ADAPTIVE MODEL-PREDICTIVE CONTROL AND 3D ACOUSTIC RADIATION FORCE IMAGING FOR THE IMPROVEMENT OF MAGNETIC RESONANCE-GUIDED FOCUSED ULTRASOUND THERAPIES

by

Joshua Thomas de Bever

A dissertation submitted to the faculty of
The University of Utah
in partial fulfillment of the requirements for the degree of

Doctor of Philosophy

in

Computing

School of Computing

The University of Utah

May 2015

THE UNIVERSITY OF UTAH GRADUATE SCHOOL

STATEMENT OF DISSERTATION APPROVAL

The dissertation of

Joshua Thomas de Bever

has been approved by the following supervisory committee members:

John M. Hollerbach Chair	12/10/2014 Date Approved
Robert B. Roemer Member	12/10/2014 Date Approved
Jake J. Abbott Member	12/10/2014 Date Approved
Dennis L. Parker Member	12/10/2014 Date Approved
Douglas A. Christensen Member	12/10/2014 Date Approved

and by Ross Whitaker, Chair of the School of Computing, and by David B. Kieda, Dean of The Graduate School.

ABSTRACT

Focused ultrasound (FUS) is a promising noninvasive and radiation-free cancer therapy that selectively delivers high-intensity acoustic energy to a small target volume. This dissertation presents original research that improves the speed, safety, and efficacy of FUS therapies under magnetic resonance imaging (MRI) guidance.

First, a new adaptive model-predictive controller is presented that leverages the ability of MRI to measure temperature inside the patient at near real-time speeds. The controller uses MR temperature feedback to dynamically derive and update a patient-specific thermal model, and optimizes the treatment based on the model's predictions. Treatment safety is a key element of the controller's design, and it can actively protect healthy tissue from unwanted damage. *In vivo* and simulation studies indicate the controller can safeguard healthy tissue and accelerate treatments by as much as 50%. Significant tradeoffs exist between treatment speed, and safety, which makes a real-time controller absolutely necessary for carrying out efficient, effective, and safe treatments while also highlighting the importance of continued research into optimal treatment planning.

Next, two new methods for performing 3D MR acoustic radiation force imaging (MR-ARFI) are presented. Both techniques measure the tissue displacement induced by short bursts of focused ultrasound, and provide a safe way to visualize the ultrasound beam's location. In some scenarios, ARFI is a necessity for proper targeting

since traditional MR thermometry cannot measure temperature in fat. The first technique for performing 3D ARFI introduces a novel unbalanced bipolar motion encoding gradient. The results demonstrate that this technique is safe, and that 3D displacement maps can be attained time-efficiently even in organs that contain fat, such as breast. The second technique measures 3D ARFI simultaneously with temperature monitoring. This method uses a multi-contrast gradient recalled echo sequence which makes multiple readings of the data without increasing scan time. This improves the signal to noise ratio and makes it possible to separate the effects of tissue heating vs displacement.

Both of the 3D MR-ARFI techniques complement the presented controller since proper positioning of the focal spot is critical to achieving fast and safe treatments.

TABLE OF CONTENTS

LIST OF TABLES

ACKNOWLEDGEMENTS

I am certainly not the first to note that many ups and downs occur in the course of completing any serious challenge. Completing my doctorate was no different. I feel very fortunate for the love and support of my family and friends; you helped immensely in weathering the storms. Mom, Dad, Ian, Lexi, Urvi, Allison, Nick, and many others: there really is no way to thank you enough. I am delighted to share with you the joy of reaching the finish line, thank you! I am also grateful to everyone from the robotics program and the School of Computing; thanks for bringing me into this fantastic program and for allowing me to put together this interdisciplinary advisory committee. To my committee members, my sincerest thanks for the advice and guidance you have provided over the course of my studies. I have learned an immeasurable amount from each of you. Finally, I am grateful to have worked with such wonderful and accomplished people at the University of Utah and the Utah Center for Advanced Imaging Research. Together, much work has been accomplished, but it is the enduring friendships we have formed that I am most thankful for.

CHAPTER 1

INTRODUCTION

1.1 Dissertation Overview

This dissertation presents work done to improve the speed, safety, and efficacy of magnetic resonance-guided focused ultrasound (MRgFUS) thermal therapies. While MRgFUS offers many potential benefits, the primary thrust of this work is to advance MRgFUS as a noninvasive and radiation-free cancer therapy.

Focused ultrasound bears similarity to diagnostic ultrasound imaging, but differs by delivering high intensity acoustic energy to a small volume and in a highly selective manner. Furthermore, the goal of FUS is to generate mechanical or thermal tissue effects instead of images. Applications of focused ultrasound are growing rapidly and currently include: mechanical fractionation of tissue (histotripsy), adjuvant hyperthermia, blood-brain barrier opening, assisted drug delivery, neuromodulation, and pain palliation.

This work focuses on thermal ablation of cancer where a variety of organs are currently being targeted including brain, breast, uterus, and liver, among others. Magnetic resonance (MR) imaging adds powerful new capabilities to ablative FUS procedures. First, MRI provides excellent soft tissue contrast for anatomical imaging, tumor identification, treatment planning, and post-treatment assessment. Second, MR thermometry makes it possible to continuously monitor the temperature inside the

patient during treatment. Third, acoustic radiation force imaging, offers the ability to interrogate the mechanical properties of tissue.

Despite these advantages, significant technical challenges impede the widespread adoption of MRgFUS in clinics. First, MRgFUS treatments take an extended period of time, both in treatment planning and patient setup stages, and in the treatment itself. This adds to the cost of MRgFUS therapy and leads to patient discomfort. Second, while MR thermometry provides vital temperature feedback, the interval between measurements is still long compared to the rate of tissue damage at higher temperatures. This leads to excessive treatment of the tumor, which wastes time and compromises the safety of normal tissues not at the focus, but in the beam path. Third, accurate positioning of the focal positions is critical to providing safe and effective treatments, but standard beam localization methods using low-power interrogation pulses risk causing unwanted tissue damage.

This dissertation presents progress toward addressing these challenges and is divided into five sections. In the remainder of Chapter 1, background theory on MRI and focused ultrasound is presented. Chapter 2 presents original results into improved control of MRgFUS using a new adaptive model-predictive controller (AMPC). The AMPC aids in accelerating MRgFUS treatments while also mitigating safety concerns through direct safeguards of healthy tissue. Chapters 3 and 4 present two methods for improved focal spot localization using 3D acoustic radiation force imaging. These techniques enable time-efficient visualization of the tissue displacement induced by a short burst of ultrasound, and are shown to be a safe alternative to standard approaches. Additionally, 3D ARFI is shown to work in tissue environments

containing fat where standard MR thermometry is ineffective. Both ARFI techniques presented encode tissue displacement into the phase of the image, however, the work in Chapter 3 presents a new motion encoding scheme used in a spin-echo sequence while Chapter 4 presents a multicontrast gradient recalled echo sequence which can simultaneous measure tissue displacement and temperature. These two 3D ARFI approaches are directly applicable to the AMPC as it requires accurate focal spot positioning to provide fast, effective, and safe MRgFUS treatments. Lastly, Chapter 5 summarizes the tasks accomplished and describes avenues for future investigation.

1.2 Principles of Magnetic Resonance Imaging

1.2.1 Benefits of MRI

Magnetic resonance imaging offers several advantages including the ability to noninvasively acquire high-resolution images with excellent soft-tissue contrast without ionizing radiation. The MR signal is dependent on many physical and system parameters, which has led to the development of numerous types of signal contrast that visualize differences among tissues in unique ways. MRI's flexibility has found wide ranging application including the identification of normal and cancerous tissue, functional mapping of the brain's internal networks, and monitoring of tissue changes over time. The lack of ionizing radiation makes it safer than modalities like X-ray computed tomography, and can produce more detailed images than ultrasound. A unique aspect of MRI is that the signal measured is derived from the sample itself, as opposed to X-ray techniques where the internal structures are inferred from the transmission (or lack thereof) of an external X-ray beam, or positron emission tomography (PET) where radioactive material is put into the body and the positrons

that escape account for the detected signal.

1.2.2 MRI Hardware Components

A typical MRI scanner consists of three principal hardware systems: (1) a primary superconducting magnet, (2) a set of resistive gradient coils, and (3) a radio frequency (RF) coil. The closely coordinated operation of these systems generates, encodes, and detects a signal, which is then reconstructed to produce images.

The primary superconducting magnet (Figure 1.1) is responsible for producing a strong and uniform magnetic field, B_0, which polarizes the sample within the bore of the MRI. Field strengths produced by clinical MRI systems currently range from approximately 1 – 3 Tesla, and the field produced by these systems are typically homogeneous to 3 ppm over a spherical volume 40-70 cm in diameter. So called "high-field" full body MRI scanners currently in development can achieve 7-11 T. Stronger main field strengths are desirable because they increase the degree of sample polarization and thus increase the amount of signal available for measurement. However, the homogeneity of the B_0 field is also critical to successful MRI imaging. Homogeneity of the main field is usually enhanced with both passive and active field

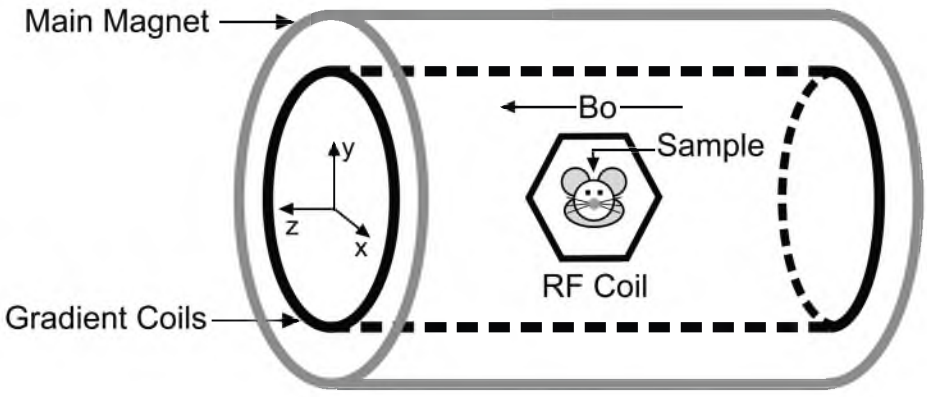

Figure 1.1: Schematic of the principal systems of an MRI.

"shimming" devices. Iron or steel blocks are inserted into the bore during installation of the main magnet to improve static field homogeneity, while special shim coils carry small currents, which can be adjusted for each subject, to generate magnetic fields that cancel out unwanted field deviations.

Radio frequency (RF) coils are responsible for both exciting the sample and detecting the resulting signal. Excitation is performed by generating a secondary time-varying magnetic field, B_1, which is perpendicular to B_0. After excitation, the RF coil is switched into "Receive Mode," and the voltage induced in the RF coil by the sample is recorded. The induced voltage recorded is the fundamental MR signal that forms all images. RF coils derive their name from the fact that the frequency of the time-varying currents they carry (typically 40 – 130 MHz for clinical systems) overlaps with the FM radio frequency spectrum. A single RF coil can be used to both excite the sample and measure the induced signal, and such coils are called transmit/receive coils. However, to maximize the signal to noise ratio (SNR), it is advantageous to place the receive coil as close as possible to the sample. Consequently, it is common to use the RF coil integrated into the bore of the magnet (sometimes called the body coil) to excite the sample while receiving with a separate coil closer to the volume of interest.

Gradient coils are resistive electromagnets that make imaging possible by spatially encoding the signal. A set of three gradient coils, one for each Cartesian axis, generate small magnetic fields that modulate B_z linearly along the x, y, and z directions. The magnetic field gradients produced are in the range of 10 – 50 mT/m for human MRI systems, but can be upward of 1000 mT/m for dedicated small animal systems.

The following sections describe in more detail how MRI generates and detects

a signal, and how that signal is used to form images. The following references are also excellent resources for additional information and derivations [1]–[4].

1.2.3 Producing a Net Magnetization

In 1922, German physicists Otto Stern and Walther Gerlach, performed an experiment that demonstrated that the angular momentum of silver came only in quantized values. Work in quantum mechanics later explained this result was due to an intrinsic quantum mechanical property of particles called spin angular momentum, or "spin." Bosons can possess only integer spin (0, 1, 2, …), while Fermions (such as electrons, protons, and neutrons) can possess only nonzero multiples of ½ integer spin $(\frac{1}{2}, \frac{3}{2}, \frac{5}{2}, \ldots)$. Consequently, the net spin of atomic nuclei (which are composed of Fermions) can take on only multiples of 0, ½-integer, or full-integer spin. When a particle with spin ≠ 0 is placed in a static magnetic field, its spin angular momentum will precess, or rotate, about the applied field at a frequency called the Larmor Frequency given by:

$$\omega_0 = \gamma B_0 \tag{1.1}$$

where γ is the gyromagnetic ratio (a nuclei specific proportionality is constant). This linear relationship between frequency of precession and field strength will prove important later when image formation is discussed.

Though imaging of other nuclei, such as ^{3}H, ^{13}C, ^{19}F, ^{31}P, and ^{23}Na (which has spin 3/2) is possible, the most commonly imaged nucleus is ^{1}H (spin ½) primarily because of its high natural abundance in the human body and large gyromagnetic ratio

(see Table 1.1).

Since MR imaging in this work was entirely based on ^{1}H, the remainder of this discussion will assume a spin ½ system. When such a system is placed in a static magnetic field, its spins can inhabit a superposition of only two energy states: aligned parallel to B_0 (low-energy state) and aligned antiparallel to B_0 (high-energy state). This is called Zeeman Splitting (or the Zeeman Effect), and the ratio of the probability of measuring a spin to be in the parallel state, $N^{\uparrow}$, vs the antiparallel state, $N_{\downarrow}$, is given by:

$$\frac{N^{\uparrow}}{N_{\downarrow}} = \exp\left(\frac{\Delta E}{kT}\right) \tag{1.2}$$

where k = 1.38x10^{-23} J/°K is the Boltzman constant, T is absolute temperature in °K, and ΔE is the energy difference between parallel and antiparallel states. To a first order approximation, $\Delta E = \gamma \hbar B_0$ where $\hbar = h/2\pi$ and h is Planck's constant 6.6 × 10^{-34} J · s. At a field strength of 3 T and body temperature of 310 °K, the population difference between $N^{\uparrow}$ and $N_{\downarrow}$ is approximately 10 parts per million. This small

Table 1.1 : Properties of selected nuclei

Nucleus	Spin	Relative Abundance in Human Body	Gyromagnetic Ratio $\gamma/2\pi$ [MHz/T]	Larmor Frequency at 3T [MHz]
^{1}H	1/2	88 M	42.576	127.7
^{13}C	1/2	0 M	10.705	32.1
^{19}F	1/2	4 μM	40.052	120.2
^{23}Na	3/2	80 mM	11.262	33.8
^{31}P	1/2	75 mM	17.235	51.7

difference is one reason higher field strengths are desirable; however, an observable signal is still generated due to the large number of spins contained in the system.

A charged particle with spin ½, such as a proton, behaves like a small electrical current, and thus produces a magnetic field much like a bar-magnet. It is useful to consider an entire population of spins so that quantum mechanical effects can be simplified to a classical picture. Without the influence of a magnetic field, the thermal energy possessed by each spin of the group serves to randomize their orientations. Thus there will be no net magnetization since each spin's magnetic moment will be canceled by another in the population. Once placed in a static field however, a net positive number of spins will align with the field (Zeeman Splitting), and the summation of the spin's moments will produce a net magnetic moment, M_0, along the direction of B_0. This is the classical picture of net magnetization that will be used in the following sections. After reaching equilibrium, the net magnetization vector points along the *z*-direction and has magnitude given by:

$$|M_0| = M_z^0 = \frac{\gamma^2 \hbar^2 B_0 N_s}{4KT} \tag{1.3}$$

where N_s is the number of spins in the sample.

1.2.4 Nuclear Magnetic Resonance and Signal Generation

At this stage, the spins subjected to B_0 are precessing, and there is a net magnetization (M_0) along *z* due to the alignment of the spins, but it is important to note that M_0 is not precessing about B_0 and thus there is no observable signal. To generate a signal, M_0 must be perturbed from equilibrium. This is done using nuclear

magnetic resonance (NMR), a discovery made by Isidor Isaac Rabi in 1938 for which he was awarded the 1944 Nobel Prize in physics. Rabi discovered that a system with spin $\neq 0$ would absorb, and then release, energy if excited by a magnetic field oscillating at a resonant frequency in a direction perpendicular to B_0. The resonant frequency turned out to be the Larmor Frequency (Eqn (1.1)), which was discovered in a different context decades earlier by Sir Joeseph Larmor in 1897. The Dutch physicist Cornelius J. Gorter proposed NMR theoretically one year before Rabi, however, Rabi was first to demonstrate the effect experimentally. To tip M_0, composed of ^1H nuclei residing in a 3 T field, away from B_0, the transmitted B_1 field must oscillate at the Larmor Frequency of 127.7 MHz (Table 1.1). This excitation pulse is commonly referred to as an RF pulse. Once M_0 has a component in the *xy* (or transverse) plane, it begins to precess about B_0. The angle that M_0 is tipped from B_0 is called the flip angle (FA), and this can be adjusted by varying the duration and/or the amplitude of the transmitted B_1 field. The achieved flip angle can be calculated from the Bloch equations, and reduces to:

$$\alpha_{FA} = \int_0^{\tau_{rf}} \gamma B_1(t) dt \tag{1.4}$$

where α_{FA} is the resulting flip angle, $B_1(t)$ is the applied, time-varying, RF pulse, and τ_{rf} is the duration that B_1 is applied (usually on the order of milliseconds). Note that the excitation is nucleus specific and that this allows the selective excitation of one nucleus without disturbing any others. Common flip angles needed for MR imaging

are 90° (shown in Figure 1.2), which results in all of M_0 being transferred into the transverse plane, and 180°, which mirrors the entire spin system about the *x* or *y* axis.

1.2.5 Signal Detection

If a receiving RF coil is placed near the precessing magnetization, a voltage will be induced in the coil due to Faraday's Law. This voltage is the fundamental signal in MRI. It is necessary to tune the receiving RF coil circuit such that it resonates at the Larmor Frequency, and consequently different RF coils must be designed for every nuclei and for each field strength.

1.2.6 Longitudinal and Transverse Relaxation

The magnetization tipped into the transverse plane represents the signal available for detection; however, the system is now out of equilibrium. After the RF

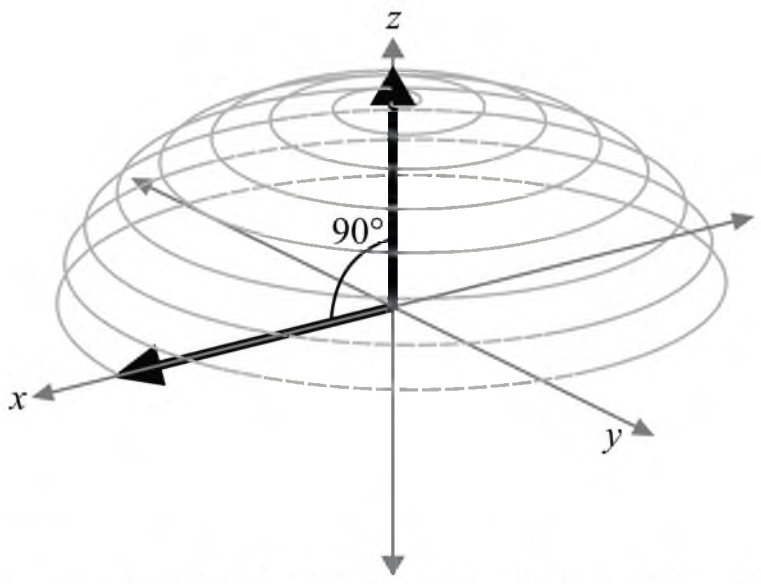

Figure 1.2: Demonstration of a 90° RF pulse caused by B_1 field applied along the *y-axis* at the Larmor Frequency. The magnetization vector (black arrow) is initially aligned with the *z*-axis (equilibrium position), and ends in the *xy* (transverse) plane.

pulse, M_z restores to M_0 exponentially with a characteristic time constant, T1. This process is called longitudinal relaxation, and the value of T1 varies for each tissue type. The restoring of M_z can be modeled by the Bloch equations, and the solution, assuming $M_z(0)$ is the remaining magnetization along the *z*-axis immediately after the RF pulse, is given by:

$$M_z(t) = M_z^0(1 - e^{-t/T1}) + \ M_z(0)\mathrm{e}^{-\mathrm{t}/\mathrm{T1}} \tag{1.5}$$

Relaxation of the magnetization also occurs in the transverse plane, independently of longitudinal relaxation, and is described by an exponential decay with time constant T2:

$$M_{xy}(t) = M_{xy}(0)e^{-t/T2} \tag{1.6}$$

where $M_{xy}(0)$ is the magnetization initially tipped into the transverse plane by the RF pulse. This relaxation process also varies by tissue type, and imposes limits on the duration available for sampling the MRI signal. Table 1.2 summarizes values of T1 and T2 for several tissues. For liquids, T2 is relatively long, while for solids it tends to be shorter. It is always the case that T1 is longer than T2.

Unfortunately, Eqn (1.6) for T2 is for a highly idealized case and many factors, such as field inhomogeneity or interactions among spins, will cause the signal to decay faster than T2 predicts. A second transverse relaxation rate, T2*, is frequently used as an effective decay rate that accounts for static field inhomogeneities. It relates to T2 by the relation:

Table 1.2 : Values of T1 and T2 at 1.5T for various tissue types

Tissue	T1 [ms]	T2 [ms]
Water/CSF	4000	2000
Gray matter	900	90
Muscle	900	50
Liver	500	40
Fat	250	70
Tendon	400	5

$$\frac{1}{T2^*} = \frac{1}{T2} + \gamma \Delta B_0 \tag{1.7}$$

Even this deviates from reality, however, it is a commonly used and useful approximating function.

1.2.7 Free Induction Decay

All 2D and 3D MR imaging is underpinned by a much simpler experiment called a free induction decay (FID). As a first example, assume a sample with a single group of spins (T1 = 500 ms, T2 = 50ms), which do not interact with one another, and who experience a uniform magnetic field. Starting from equilibrium such that Mz = M0, and Mxy = 0, a 90° RF pulse is applied and subsequently Mxy = M0, while Mz = 0. The net magnetization begins to precess around B0, and the rotating transverse magnetization induces a voltage in the receiving RF coil. This signal is given by:

$$S(t) = M_z^0 \sin(\alpha_{\mathrm{FA}}) e^{-t/T2} e^{-i\omega_0 t} \tag{1.8}$$

As the rotating M_{xy} changes its orientation with respect to the receiver RF loop, so does

the magnetic flux and induced voltage, and so the signal recorded oscillates between +/- its maximum value at the Larmor Frequency (Figure 1.3a). As time passes, the signal amplitude is bounded by an exponential decay envelope, and after one T2 interval, 63% of the initial transverse magnetization has been lost. By five T2 intervals, nearly all the signal has been lost. Conversely, M_z recovers approximately 63% of its equilibrium value after one T1 interval.

Now consider a second example where there are two spin groups with the same T1 and T2 as before, but who experience different magnetic fields due to an inhomogeneity of B_0. The result is that each group precesses at a slightly different frequency which causes the transverse magnetization to decay at a rate of T2* instead of T2 (Figure 1.3b).

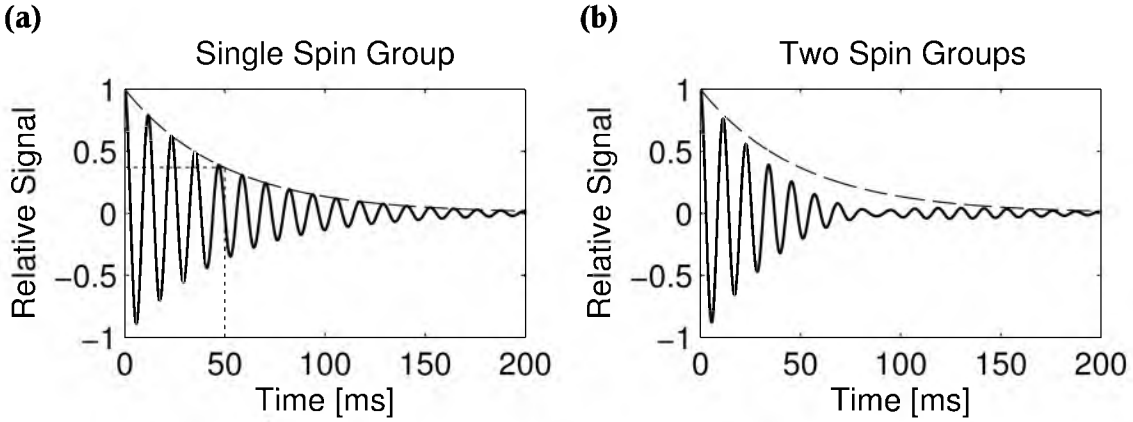

Figure 1.3: Signal from a single spin group compared to that of two spin groups. **(a)** FID from a single spin group in a uniform field. Dashed line indicates signal decay envelope at a rate of T2. **(b)** FID from a sample with two spin groups experiencing different fields due to inhomogeneity of B_0. FID decays at T2*, faster than T2 (dashed lined). Note: Larmor Frequency reduced to make oscillations more visible.

1.2.8 Image Formation in 2D and 3D

In the FID experiment, nothing can be done about the field inhomogeneities that increased the rate of signal loss, and so the optimal time to measure the signal is immediately after the RF pulse. This is problematic for MR imaging because the additional steps required before the signal can be measured (to be discussed later) result in significant signal decay. There are two commonly used techniques that recover some of the lost signal by creating a signal echo after a user defined delay called the echo time (TE). These techniques have the additional advantage of affording some flexibility in selecting when to measure the signal.

1.2.8.1 Gradient recalled echoes

The first approach to creating a signal echo is to apply an intentional field gradient along one direction, say the x direction, which adds phase to the spins and reduces the signal. Then, the gradient polarity is reversed causing the phase of the spins to decrease and eventually refocus to produce a signal echo. This is called a gradient recalled echo (GRE) and is illustrated in Figure 1.4. This technique tends to be fast, but cannot compensate for static field inhomogeneities and thus the signal decays as T2* instead of T2.

1.2.8.2 Spin-echoes

Figure 1.5 demonstrates the spin-echo (SE) approach to forming a signal echo. By adding an additional RF pulse with a 180° flip angle at a time TE/2 after the initial excitation RF pulse, the spin system will be mirrored such that the spins' accrued phase in the transverse plane is negated. As the spins continue to precess after the 180° pulse,

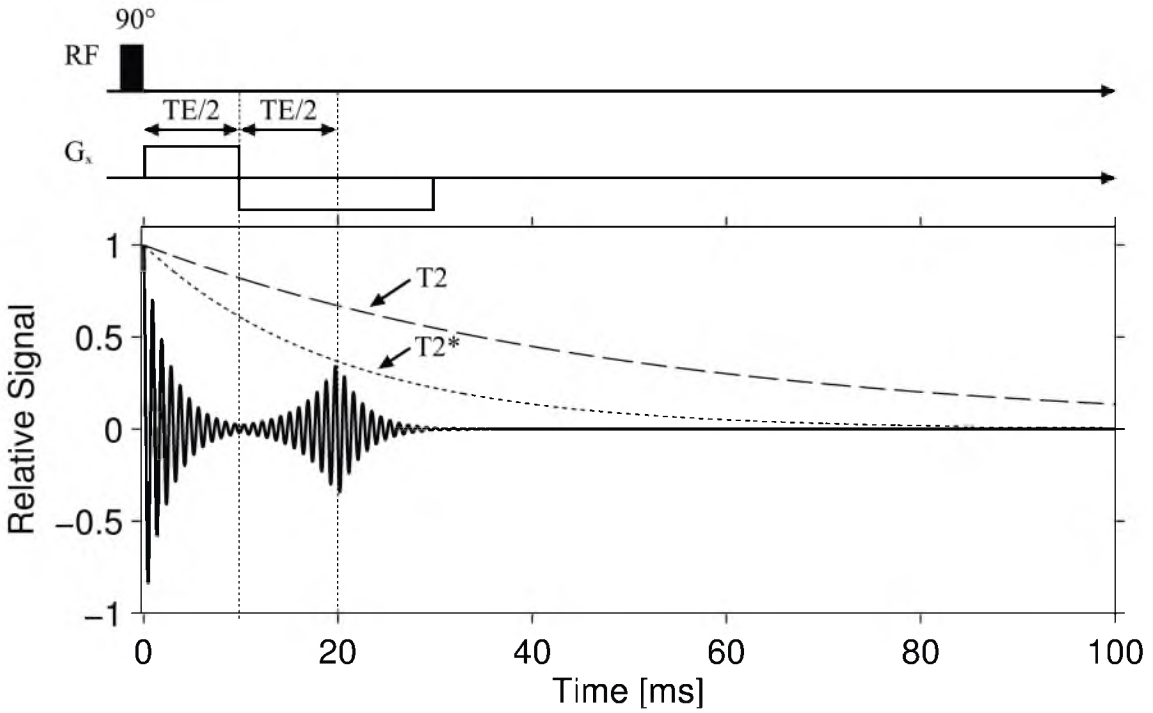

Figure 1.4: Gradient recalled echo generated at TE by applying gradients to intentionally dephase the spins, then rewinding the spins with an opposing gradient which forms an echo at TE. Signal decays with T2*, faster than T2, and static field inhomogeneities are not reversed.

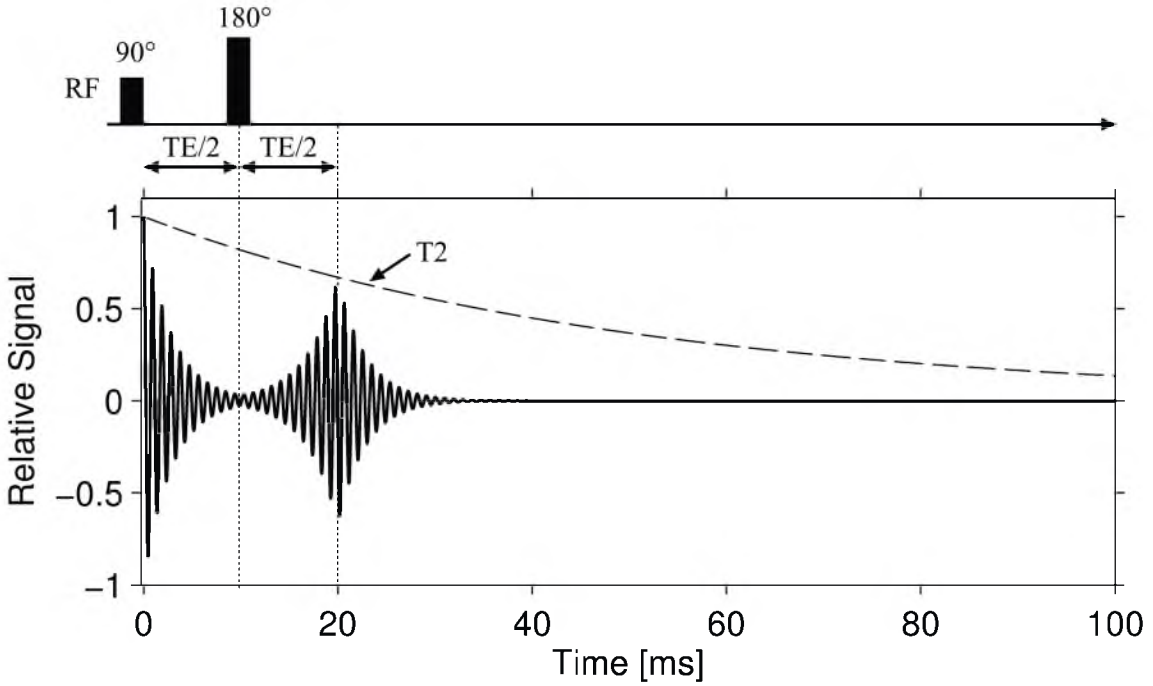

Figure 1.5: Spin-echo generated at TE by applying a 180° pulse at TE/2. Signal decays with T2, but static field inhomogeneities are reversed to recover more signal at t = TE.

they will come back into phase at t = TE creating a signal echo. One major advantage of the SE approach over the GRE approach is that the effect of static field inhomogeneities will be canceled out at the echo time because the spins encounter the same field deviations after the 180° pulse as they did before the 180° pulse. As a result, the signal decays at a rate of T2 (which is not reversible) instead of T2* as in the GRE case. The downside of the SE method is that it requires an additional RF, which takes time and deposits additional energy into the sample. The 180° pulse can also induce new, unwanted, signal that can corrupt the image.

1.2.8.3 Frequency and phase encoding

Up to this point, NMR has been used to induce a FID signal which is a measure of the bulk magnetization in the sample. However, to assemble a 2D image, a method for localizing where the signal came from must be developed. It may seem obvious now that the equation for the Larmor Frequency, $\omega = \gamma B_0$, gives us a method for accomplishing this, but the technique, first published in 1973, won Paul Laterbur a Nobel Prize. By modulating the large B_0 field by imposing an additional field that varies linearly across one dimension, for example the *x* direction, the precession frequency becomes a function of position given by:

$$\omega(x) = \gamma(B_0 + G_x x) \tag{1.9}$$

where $G_x(x)$ describes the gradient field in T/m. This is called frequency encoding. For a real object, the signal measured is now a function of the density of spins, $\rho(x)$, and the position of those spins along the *x* direction:

$$S(x,t) = \int \rho(x) e^{-i\gamma G_x x t} dx \tag{1.10}$$

where the baseline frequency ω_0 has been subtracted. It is important to note that the fact that the gradient is linear and of known magnitude is critical for accurate spin localization. A skilled pianist sitting at their piano blind folded can determine the location of keys that produce low pitch notes (to their left) vs high pitched notes (to their right) because they are familiar with the ordering of the piano. Similarly, the known gradient makes it possible to map the measured frequency to a location along the *x* axis. It is common to refer to the axis being frequency encoded as the "readout direction." There remains one problem; every *yz* plane at a given *x* position has been assigned the same frequency and cannot be separated.

To solve this, an additional form of spatial encoding, called phase encoding (PE), is performed. Similar to frequency encoding, a linearly varying magnetic field, produced by the gradient coils, is applied along a direction perpendicular to the readout direction, commonly referred to as the phase encode direction. The phase encoding gradient is only enabled for a brief amount of time, but while enabled, it causes spins along the PE-direction to accrue a phase proportional to the time the PE gradient is enabled and their position along the PE direction. Thus, if the PE direction is along the *y* axis, and the field is given by $G_y(y)$ in T/m, then the phase of the spins along *y* is now:

$$\phi(y,t) = \int_0^{\tau_{PE}} \gamma G_y(t) y \, dt \tag{1.11}$$

This can be thought of as a gradient-time area, or gradient moment, and explains that for a given phase/area, time can be exchanged for higher amplitude or vice versa. An ideal gradient system turns on and off instantaneously, and under this idealization, Eqn (1.11) reduces to:

$$\phi(y) = \tau_{PE}\gamma G_y(y) \tag{1.12}$$

And the updated signal equation is:

$$S(x,y,t) = \iint \rho(x,y)e^{-i\gamma(G_x x t + \gamma G_y y \tau_{pe})}\, dxdy \tag{1.13}$$

The last dimension (the *z* axis but generally referred to as the slice direction) is localized by selectively exciting a plane (2D imaging), or volume (3D imaging). The NMR concept says that an RF pulse only excites spins that share its resonant frequency. By applying a third gradient along the slice direction, spins will resonate at a range of frequencies, and by designing the RF pulse carefully so as to match the bandwidth of the desired spins, only a small slice of the object will be excited. Consequently, parts of the sample not in the slice will not generate a signal because their magnetization remains aligned with B_0 and not in the transverse plane. For 2D imaging, it is sufficient to perform this slice selective RF pulse and perform phase and frequency encoding. Multiple 2D slices can be acquired to increase the coverage of the sample. Alternatively, a 3D acquisition can be accomplished where the selective excitation is performed over a thick slice (a slab) that encompasses the entire volume of interest, and a second set of phase encoding is required along the *z* direction to

resolve spins within the excited volume.

1.2.8.4 Sampling k-space and the Fourier transform reconstruction

A unique aspect of MRI is that the data acquired represent samples of the spatial-frequencies of the object. This spatial-frequency domain is referred to as k-space. In order to generate an image that accurately represents the object, k-space sampling must satisfy the Nyquist sampling criteria. As shown in Figure 1.6, for a square field-of-view (FOV) and desired resolution (Δx) the required k-space sampling parameters are calculated from:

$$\Delta k_x = \frac{1}{\mathrm{FOV}} \qquad \mathrm{W}_{kx} = \frac{1}{\Delta x} \tag{1.14}$$

A useful analogy is to think of k-space as an "Etch-a-Sketch" where the knobs are the frequency encoding gradient (which moves the sampling point along k_x) and the phase encoding gradient (which moves along k_y). The gradient amplitude controls how fast k-space is traversed. The complex signal on the RF receive coil is a single point of k-space, which is sampled by an analog-to-digital converter (ADC). Once all the required k-space samples are collected, the data are transformed into image space using a Fourier transform.

The timing diagram in Figure 1.7 shows how two lines of k-space could be sampled using a 2D spin-echo acquisition. First, slice-selective excitation is performed. Immediately after excitation, the sampling point is at the center of k-space. The first line of k-space to be acquired is k_y = 0, so no phase encoding gradient is required. A

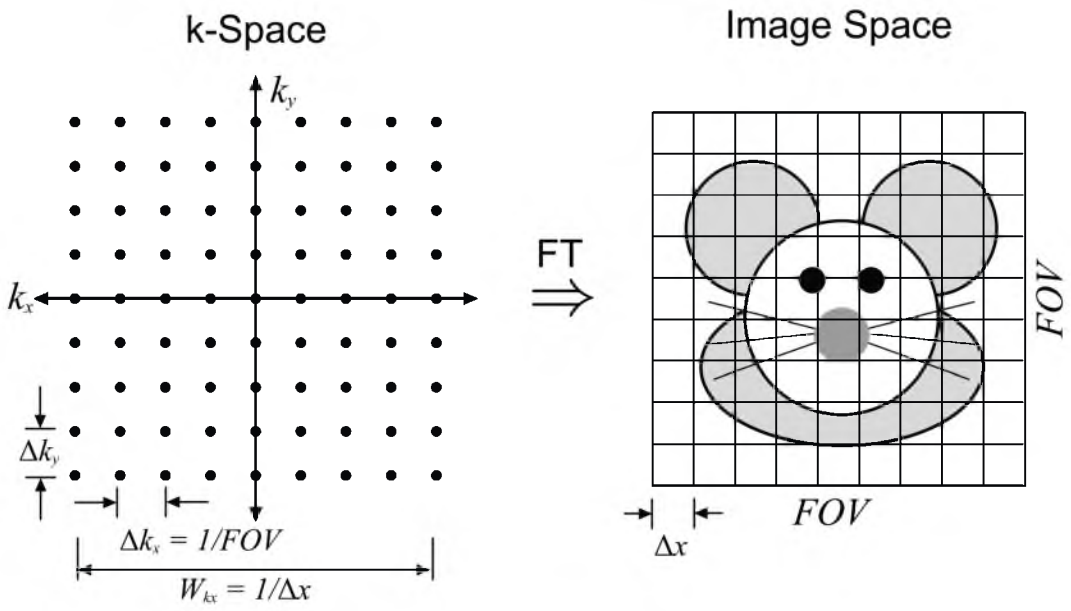

Figure 1.6: MRI samples (black dots) of the object's spatial-frequencies in k-space. After sufficient sampling of k-space, a Fourier transform is performed to generate an image. Width of the square field-of-view is *FOV* and the voxel size is Δx. From these quantities, it is possible to solve for the required k-space sampling interval and frequency extent that must be sampled.

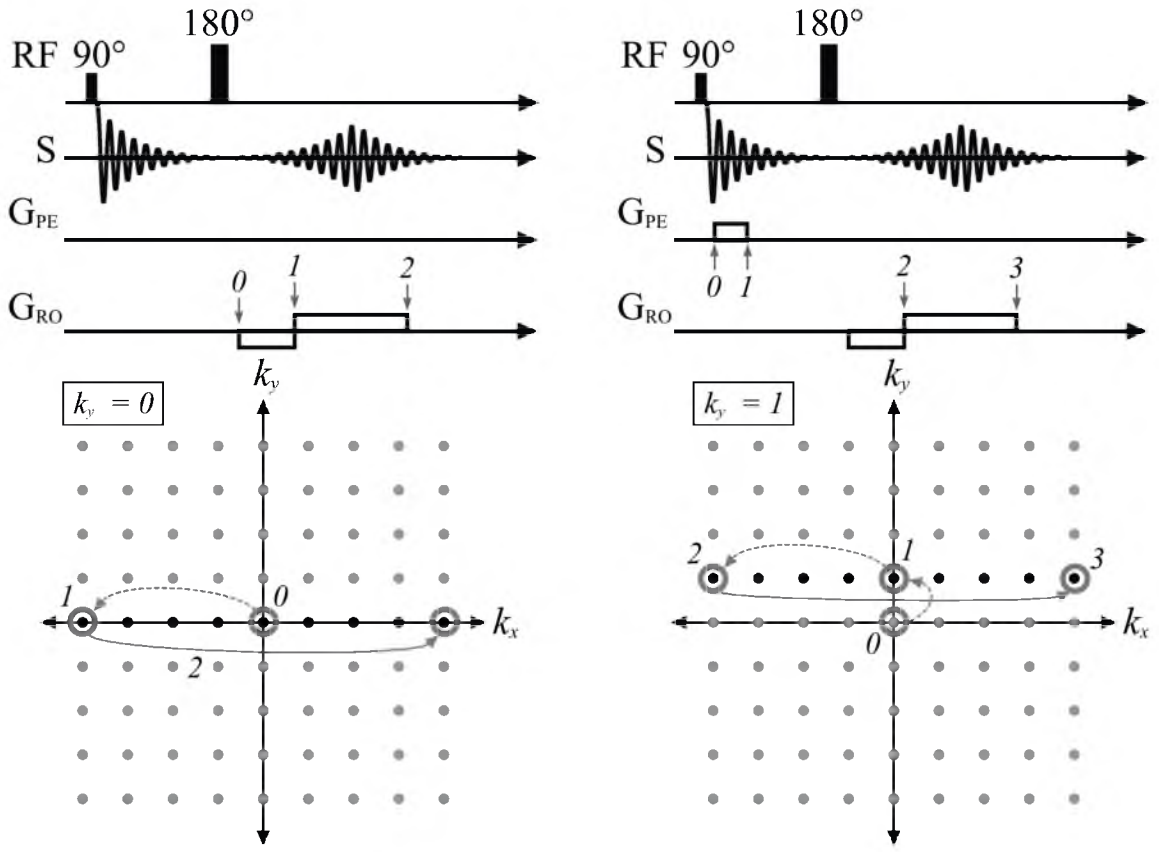

Figure 1.7: Example of Cartesian sampling of two k-space lines using a 2D spin-echo acquisition. Black dots indicate sample locations measured during the current excitation. Gray dots are samples acquired during other excitations. Dashed gray lines indicate the linear traversal between two circled locations in k-space without acquiring data. Solid gray lines indicate that data are being acquired at an interval Δt while moving linearly between two circled locations. Numbers indicate the ordering of events as they unfold due to the timing diagram.

fast way to sample data along the frequency encode (readout) direction is to start at the -k_x edge and traverse at constant speed toward +k_x while sampling at an appropriate time interval, Δt. To accomplish this, a negative readout gradient moves to –k_{max}, and then a positive, constant, gradient is applied to move toward +k_{max}. For a given readout gradient amplitude and Δk_x, the sampling interval Δt is given by:

$$\Delta t = \frac{2\pi}{\gamma G_x}\Delta k_x = \frac{2\pi}{\gamma G_x FOV} \tag{1.15}$$

This completes the acquisition of one line of k-space. The entire process is then repeated for k_y = 1 where, after the excitation, the sampling point is again at $k_x = k_y = 0$. To move to k_y = 1, the phase encode gradient must be applied. As higher k_y frequencies are sampled, the phase encoding gradient area required grows. Normally, the duration of the phase encoding gradient is kept constant, so to cover a larger k_y distance in the same time, it is necessary to increase the gradient amplitude. Assuming a phase encode duration of τ_{PE}, the PE gradient amplitude increment can be calculated by:

$$\Delta G_y = \frac{2\pi}{\gamma \tau_{PE}}\Delta k_y = \frac{2\pi}{\gamma \tau_{PE} FOV} \tag{1.16}$$

The acquisition of each k_x line requires a new excitation pulse. The time between repeated excitation pulses, TR, is an important parameter that determines the total amount of time it will take to acquire all lines of k-space, and how much

longitudinal relaxation will occur between of each acquisition along k_x. Another fundamental sequence parameter is the echo time TE. Note that the echo was formed as k_x = 0 was acquired. The center frequencies tend to be most important to the image, so it is advantageous to sample them when the signal is maximal. The process is similar for 3D acquisitions except for the additional k_z phase encoding steps which require more repetitions.

1.2.9 MR Thermometry

The first method for measuring temperature with MRI was published in 1983 and was based on the temperature dependence of the longitudinal relaxation time constant, T1 [5], [6]. It was found that T1 varied linearly over small temperature ranges and could thus be used to measure absolute temperature. This technique did not gain widespread popularity in part because T1 mapping is time consuming, and also because T1 varies across multiple parameters including tissue type and field strength.

The most popular MR thermometry method, which is used exclusively in this work, is the proton resonance frequency shift technique [7], [8]. As the name implies, when protons in water heat up, their resonant frequency changes by approximately -0.009 ppm/°C. The reduction in resonant frequency is a result of increased shielding of the hydrogen atom by the electrons on the oxygen atoms in water. The increased shielding reduces the effective local magnetic field experienced by the hydrogen atom, resulting in a frequency reduction. When tissue warms, the hydrogen protons precess about B_0 at a slower rate, and thus a phase difference will accrue over time.

The PRF method is normally used in conjunction with a GRE pulse sequence since the refocusing 180° RF pulse in SE sequences would cancel out most of the phase accrued due to temperature. The phase difference for a series of measurements over time is computed by subtracting a baseline phase image from each time frame. The change in phase can then be converted to a change in temperature, $\Delta\mathrm{T}$, via:

$$\Delta\mathrm{T} = \frac{\Delta\phi_i}{\beta\gamma B_0 TE} \tag{1.17}$$

where $\Delta\phi_i$ is the total phase change relative to the baseline for the i-th measurement, and β is the previously mentioned proportionality constant -0.009 ppm/°C. There is a tradeoff in selecting the value of TE since a longer TE results in more T2* signal loss (which reduces SNR) but provides more time for phase to accrue (which increases phase-SNR). Generally, a TE $\approx$ T2* strikes a good balance between these parameters.

It is fortunate that β is linear and relatively independent of tissue type over typical temperature ranges since it facilitates temperature monitoring in most tissue without advanced calibration. One notable exception to this is fat, which does not experience a temperature-dependent frequency change, and thus cannot be monitored with the PRF technique. This is especially problematic for MRgFUS applications in the breast.

1.3 Principles of Focused Ultrasound Thermal Therapies

1.3.1 Overview

The term "ultrasound" refers generally to any sound wave of a frequency above that of human hearing. Typical applications of ultrasound use frequencies above 20 kHz up to 10 MHz, though frequencies can extend to several hundred MHz [9]. At a simple level, sound is a mechanical vibration of particles that propagates by contact with other particles. As particles come into contact and compress, a pressure above static pressure is generated, and this pressure field is propagated through most biological tissue. A common method of producing ultrasound waves is using piezoelectric materials that compress and expand in response to an applied voltage. These devices are called ultrasound transducers because they convert electrical energy into mechanical energy (ultrasound). However, the effect works in reverse as well; deformation of the piezoelectric element by an incident pressure wave will generate a voltage. This forms the basis for ultrasound detection and medical imaging via ultrasound.

Ultrasound has proved to be an invaluable tool in medical imaging because it is safe, portable, inexpensive, and provides high frame rates. In contrast, focused ultrasound is not used for imaging, but instead aims to modify tissue through either mechanical or thermal effects. To accomplish this, higher powers are often required. The effects of high-power ultrasound were noted as long ago as 1920 when Paul Langevin placed his hand in a water tank insonified with high-intensity ultrasound and discovered that pain was induced [10]. In the 1940s Lynn and Putnam first used focused ultrasound to produce cerebral lesions [11], [12], but in doing so also

discovered how difficult it is to transmit ultrasound through bone. Soon after, in the 1950s, the Fry Brothers in collaboration with Meyers would demonstrate focused ultrasound surgery in the brain by first performing a craniotomy [13], [14]. The development of new materials, new technologies such as MR thermometry, and increased computational power have led to a resurgence of focused ultrasound research. For example, it is now possible to transmit meaningful amounts of energy through an intact skull utilizing beam refocusing algorithms that make use of CT/MRI to measure the skull's thickness. [15]. Furthermore, real-time MR thermometry makes it possible to monitor the progress and safety of cancer therapies performed by focused ultrasound.

1.3.2 Wave Propagation

The following will assume that a transducer is positioned as shown in Figure 1.8, and that this transducer produces a wave of frequency f [Hz]. The mechanical

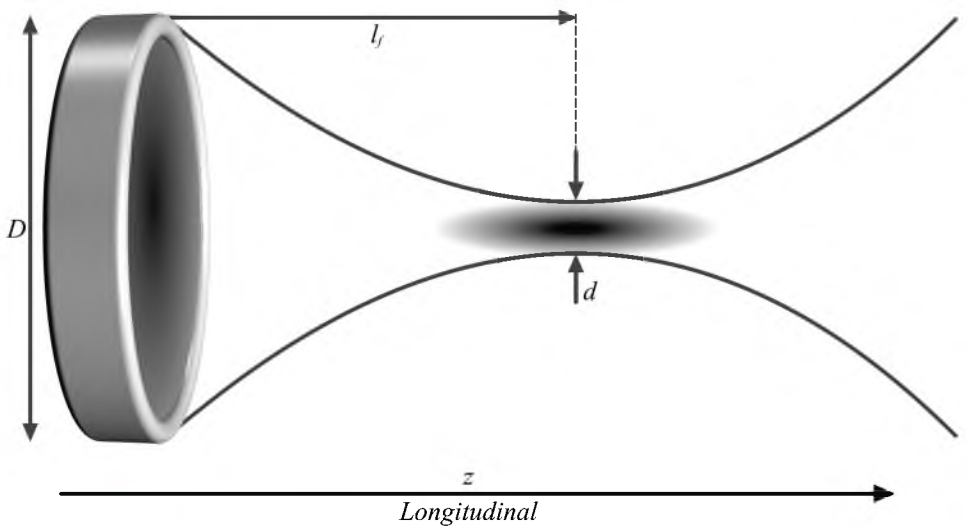

Figure 1.8: Phased array transducer. D = Diameter. l_f= Focal length, d = diameter of focus.

vibrations along the beam propagation direction (longitudinal, or *z* direction) give rise to a pressure, $p(z)$ and results in a particle velocity, $u(z)$. Note that the particles have no net motion, they simply oscillate about a central position at a velocity given by u. The speed at which the wave front propagates is given by c, the speed of sound, values for which vary by tissue type. For water, c_w= 1500 m/s, and this is a good approximate value for most soft tissues. The ratio of pressure and particle velocity defines a medium's impedance, Z, which is also related to the density of the tissue, ρ, and the speed of sound by:

$$Z = \frac{p}{u} = \rho c \tag{1.18}$$

The beam will propagate through a medium with a wavelength, λ, given by:

$$\lambda = \frac{c}{f} \tag{1.19}$$

Thus a 1 MHz wave in water would have a wavelength of λ= 0.15 cm. From these quantities, the power density of a wave is defined as:

$$I = \frac{p^2}{Z} \tag{1.20}$$

As the wave propagates through successive layers of tissue, several factors conspire to dissipate its energy, namely: (1) absorption, (2) scattering, (3) reflections off tissue interfaces. Absorption and scattering are usually combined into a single attenuation

coefficient, α, that varies by tissue type and is approximately linearly proportional with frequency. If a wave entering a block of tissue has initial pressure p_0, and corresponding power density I_0, then the remaining pressure and power after traveling a distance z through the tissue is:

$$p(z) = p_0 e^{-\alpha z} \qquad I(z) = I_0 e^{-2\alpha z} \tag{1.21}$$

In medical imaging applications it is desirable to use smaller wavelengths to improve the imaging resolution. However, Eqn (1.21) demonstrates the increased attenuation that results from higher frequencies will reduce the depth of penetration for a given power density. Using the same reasoning, when attempting to transmit focused ultrasound through the skull, lower frequencies are desirable because less loss occurs in the bone and regions deeper into the head become reachable. As will be seen later, the weakness of using larger frequencies for FUS is that it enlarges the focal spot.

Finally, reflections must be considered. Assume the situation in Figure 1.9

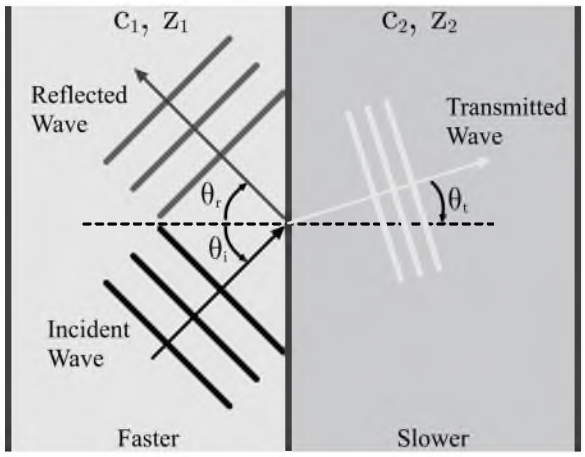

Figure 1.9: Reflection and refraction of incident wave at interface between two tissue types.

where a plane wave traveling in a medium with speed of sound c_1 and impedance Z_1 strikes a tissue boundary at an angle θ_i relative to the normal of the boundary. Also, assume the second material has speed of sound $c_2 \neq c_1$ and impedance $Z_2 \neq Z_1$. Some of the incident beam will be reflected at an angle $\theta_r = \theta_i$ and thus cannot contribute to the forward motion of the wave. The transmitted wave will be refracted as it passes through the boundary due to differences in the speed of sound of the materials. The angle of the transmitted wave is given by Snell's law, which applies for ultrasound waves just as it does for electromagnetic waves:

$$\frac{\sin\theta_i}{\sin\theta_t} = \frac{\lambda_1}{\lambda_2} = \frac{c_1}{c_2} \tag{1.22}$$

A reflection coefficient, R, is defined as the ratio of the reflected (p_r) and transmitted (p_i) pressure waves for a given angle of incidence and transmission:

$$R = \frac{p_r}{p_i} = \frac{(Z_2/\cos\theta_t) - (Z_1/\cos\theta_i)}{(Z_2/\cos\theta_t) + (Z_1/\cos\theta_i)} \tag{1.23}$$

In this work, only small incident angles will be considered ($\theta_i = \theta_t \approx 0°$), which reduces the previous equation to:

$$R = \frac{Z_2 - Z_1}{Z_2 + Z_1} \tag{1.24}$$

Most often, the reflected power is of more interest than the reflected pressure. By computing the ratio of power densities we attain for the reflected wave:

$$\frac{I_r}{I_i} = \frac{p_r^2/Z_1}{p_i^2/Z_1} = R^2 \tag{1.25}$$

For the transmitted wave:

$$\frac{I_t}{I_i} = \frac{\left(1 + (p_r/p_i)\right)^2 Z_1}{Z_2} = (1+R)^2 \frac{Z_1}{Z_2} \tag{1.26}$$

From these equations it is now possible to calculate the losses due to attenuation while traveling through a uniform tissue layer, as well as the reflected and transmitted power densities at a boundary between two tissue layers.

1.3.3 Beam Focusing and Transducer Types

To generate selective and intense tissue heating, it is necessary to concentrate a transducer's power density into a small volume, referred to in this work as the "focal spot." Several methods exist to produce this focusing effect.

First, a single-element transducer can have a sonic lens placed in front of it, which, much like glasses correct human vision, causes the incident wave to be bent and focused to the desired focal distance. This method has the advantage that different lenses can be inserted to provide multiple focal distances with a single transducer. However, it is not optimal for FUS therapies since it cannot be changed quickly during a treatment and so mechanical positioning would still be necessary.

Second, the surface of a single-element transducer can be made in a spherical shape, which results in a natural focus (or geometric focus) determined by the radius of curvature (see Figure 1.8). This eliminates the need for a lens, but also fixes the focal

position, and thus to reach multiple positions in the tumor, mechanical movement of the transducer would be needed.

Third, the surface of a spherically shaped transducer can be broken into many individually controllable elements. This is called a phased-array transducer and is the type of device used throughout this work. For a given radius of curvature, the single element transducer creates a geometric focus at the same location as the phase-array, however, the phased-array can dynamically adjust the location of peak intensity by altering the phase of the voltage that excites each element. This is referred to as electronic steering and does not require mechanical movement of the transducer. A variety of phased-array transducer designs exist with the number of elements ranging from 10s to 1000s.

The advantages of phased-array transducers has opened new possibilities for FUS that were not available to investigators in the 1940s. For starters, MR thermometry provides a remarkable noninvasive monitoring capability, but the movement of objects (such as a transducer), even if outside the imaging volume, can induce variations in the magnetic field experienced by the sample, corrupting the temperature maps. Furthermore, mechanical movement requires motors that tend to induce noise and artifacts in the MR images. Electronically steering the focal spot with a phase-array transducer avoids these issues, and complex trajectories can be achieved without motors. Transcranial transmission of ultrasound is another emerging application reinvigorated by phased-array technology. While nothing can be done to reduce the attenuation of the skull, the focal quality and amount of energy delivered to the target volume is degraded by variations in the skull's thickness. With knowledge

of the skull's geometry derived from CT or MR imaging, the element phases can be adjusted to correct for these effects [15]. Phased-array transducers do introduce significantly more complexity to the electronics required to drive the system, and makes the system more costly. Also, power is lost to secondary grating lobes which can, depending on the design of the transducer, deposit significant energy outside the desired focal spot. This can be reduced by decreasing the spacing between elements to $< \lambda/2$, but this can mean using a very large number of elements. Another strategy is to randomly position the elements such that they create fewer locations of secondary constructive interference.

The focal spot for ablative FUS transducers is usually ellipsoidal in shape, and the systems used in this work have a full width half max (FWHM) on the order of 2 x 2 x 8 mm at 1 MHz. For a spherical transducer, the pressure pattern at the focus is given by a first-order Bessel function of the first kind, and the diameter, d, of the focal spot can be computed from the first zeros of this function:

$$d = 2.44 \left(\frac{l_f}{D}\right) \lambda \tag{1.27}$$

It can be seen that the width depends on the focal length, l_f, and the transducer diameter, D, as well as the wavelength (see Figure 1.8). Thus lower frequencies (larger wavelengths) will increase the diameter of the focal spot.

1.3.4 Heating Tissue with Focused Ultrasound

The amount of tissue heating generated by application of focused ultrasound depends on many parameters including: the transducer design, focal spot size, applied power, applied frequency, and tissue properties such as specific heat, density, and attenuation. While attenuation includes the combined effects of absorption and scattering, absorption is the dominant factor in most biological tissues. Therefore, energy lost due to attenuation is approximately the energy available to generate tissue heating. If the power density from Eqn (1.21) is differentiated with respect to a volume δz, the result is the following expression for the time-rate of energy deposition per unit volume, $\dot{Q}$:

$$\dot{Q} = -2\alpha I \tag{1.28}$$

Sometimes a related quantity called the specific absorption rate (SAR) is used, and this is related to $\dot{Q}$ with:

$$SAR = \frac{\dot{Q}}{\rho} \tag{1.29}$$

Here, SAR has units of W/kg compared to $\dot{Q}$ units of W/m^3. Given the rate of energy delivery to the tissue, and the tissue's specific heat, c_h, the rate of temperature rise can be calculated from:

$$\frac{\delta T}{\delta t} = \frac{\dot{Q}}{\rho c_h} \tag{1.30}$$

In reality, this will only apply at the start of a heating pulse as conduction will transfer heat to neighboring tissue and reduce the rate of heating. A more accurate and detailed thermal model commonly used is the Pennes bioheat transfer equation [16]; it accounts for conduction and perfusion losses. This model can be implemented on a computer but requires detailed knowledge of the tissue properties and their spatial distribution. Regardless, the rate of tissue heating can be on the order of 1-4 °C /s for FUS thermal ablation, and given common MR thermometry sampling intervals of 2 – 8 s, significant temperature change can occur within one temperature sample. This poses challenges for control of thermal therapies, a topic addressed in more detail in Chapter 2.

1.3.5 Thermal Dose

MR thermometry allows for the monitoring of tissue heating caused by FUS, however, a metric that relates temperature history to tissue damage is necessary to effectively treat cancerous tumors while preventing damage to healthy tissue. The most commonly used metric, and the one used throughout this dissertation, is the cumulative equivalent minutes at 43 °C thermal dose metric [17], given by:

$$CEM_{43} = \int_0^t R^{T-43} dt \tag{1.31}$$

where T is the temperature of the tissue in °C, and $R = 2$ when $T \geq 43$ °C and $R = 4$ when $T < 43$ °C . A thermal dose of 240 CEM_{43} is a conservative threshold for histological tissue damage. This is explored in more detail in Chapter 2.

1.4 MR Acoustic Radiation Force Imaging

This section combines the MRI and ultrasound concepts discussed in Sections 1.2 and 1.3 to provide a description of how acoustic radiation force imaging (ARFI) can be measured using MRI. The benefits of performing MR-ARFI are discussed in Chapters 3 and 4. As ultrasound propagates through tissue, energy is lost due to absorption and reflections. Assuming a homogenous medium, reflections will be ignored. Given the time-average beam intensity, I, and the attenuation coefficient α, the resulting radiation force per unit volume, Γ_a is:

$$\Gamma_a = \frac{2\alpha I}{c} \tag{1.32}$$

This force causes the tissue to displace by a small amount, typically 1-30 μm depending on the applied power and tissue properties. To encode this displacement into the MR signal, a new set of gradients, called motion encoding gradients (MEG) are applied before the signal is readout. Many MEG schemes are possible, but a simple bipolar scheme is shown in Figure 1.10. If no displacement is present, as is the case when the ultrasound is off, then the first lobe of the MEG will add a phase to all spins which will be subsequently subtracted by the second lobe of the MEG. An entire set of k-space is acquired with ultrasound "OFF" and saved. Next, a measurement is acquired where a short burst of ultrasound (1 – 20 ms) is fired during only the second lobe of the MEG. In this case, the first lobe adds a phase, as before, however, spins that are displaced during the second lobe do not experience the same magnetic field they did during the first lobe, and thus a residual phase will remain in locations that

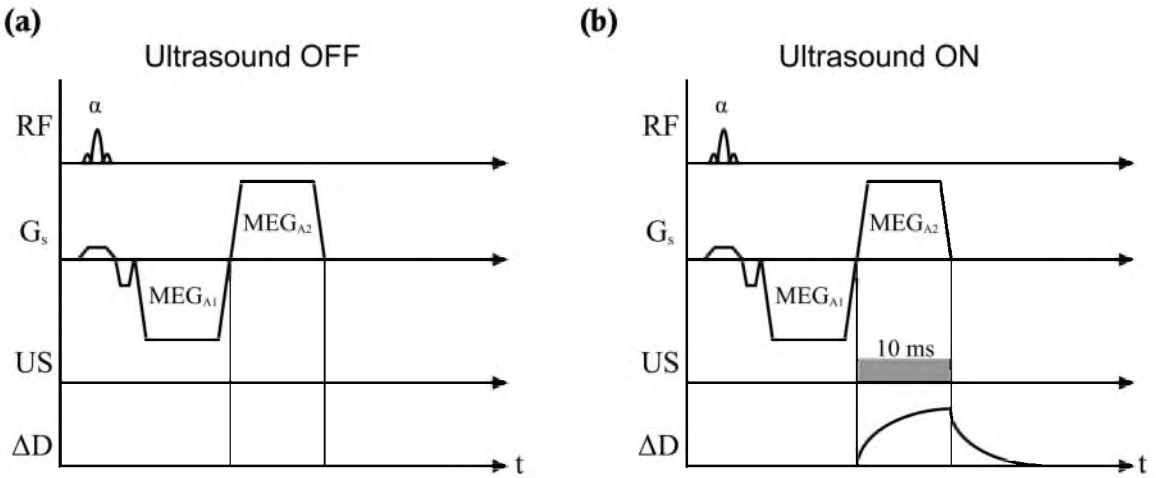

Figure 1.10: Example timing diagram with ARFI motion encoding gradients. **(a)** When no US pulse is used the phase added by MEG_{A1} gets subtracted during MEG_{A2}. **(b)** When US is fired during MEG_{A2}, the phase added by MEG_{A1} is not subtracted for tissue that was displaced by the US.

experienced displacement. When a motion encoding gradient of duration t_{enc} is applied at an amplitude of G_{MEG}, then the tissue displacement, ΔD, generates an accrued phase given by:

$$\Delta\phi_a = \gamma \int_0^{t_{enc}} G_{MEG}(t)\Delta D(t)dt \tag{1.33}$$

Similar to PRF thermometry, described in Section 1.2.9, $\Delta\phi_a$ is derived from a complex phase subtraction performed between the reference image (with no ultrasound), and the image with ultrasound on. Since G_{MEG} is known, the phase difference can then be converted to a time-average displacement using:

$$\Delta D = \frac{\Delta\phi}{\gamma MEG_{Mom}} \tag{1.34}$$

where MEG_{Mom} is the gradient area set by the user in the MR pulse sequence.

It is necessary to synchronize the start of the ultrasound burst with the MEG. At the time this work was carried out, no hardware existed for doing so. Appendix A describes the design of a device to trigger the ultrasound from an optical trigger pulse emitted by the MRI.

1.5 References

[1] Z.-P. Liang and IEEE Engineering in Medicine and Biology Society, *Principles of magnetic resonance imaging: a signal processing perspective*. Bellingham, Wash. : New York: SPIE Optical Engineering Press ; IEEE Press, 2000.

[2] D. G. Nishimura, *Principles of magnetic resonance imaging*, 1.1 ed. Stanford University Press.

[3] C. P. Slichter, *Principles of magnetic resonance*, 3rd ed. Berlin; New York: Springer, 1996.

[4] E. M. Haacke, *Magnetic resonance imaging: physical principles and sequence design*. New York: Wiley, 1999.

[5] D. L. Parker, V. Smith, P. Sheldon, L. E. Crooks, and L. Fussell, "Temperature distribution measurements in two-dimensional NMR imaging," *Med. Phys.*, vol. 10, no. 3, pp. 321–325, Jun. 1983.

[6] D. L. Parker, "Applications of NMR imaging in hyperthermia: an evaluation of the potential for localized tissue heating and noninvasive temperature monitoring," *IEEE Trans. Biomed. Eng.*, vol. 31, no. 1, pp. 161–167, Jan. 1984.

[7] Y. Ishihara, A. Calderon, H. Watanabe, K. Okamoto, Y. Suzuki, K. Kuroda, and Y. Suzuki, "A precise and fast temperature mapping using water proton chemical shift," *Magn. Reson. Med.*, vol. 34, no. 6, pp. 814–823, Dec. 1995.

[8] J. De Poorter, C. De Wagter, Y. De Deene, C. Thomsen, F. Ståhlberg, and E. Achten, "Noninvasive MRI thermometry with the proton resonance frequency (PRF) method: in vivo results in human muscle," *Magn. Reson. Med.*, vol. 33, no. 1, pp. 74–81, Jan. 1995.

[9] D. A. Christensen, *Ultrasonic bioinstrumentation*. New York: Wiley, 1988.

[10] S. L. Hagen-Ansert, "Society of diagnostic medical sonographers: a timeline of historical events in sonography and the development of the SDMS," *J. Diagn.*

Med. Sonogr., vol. 22, no. 4, pp. 272–278, Jul. 2006.

[11] J. G. Lynn, R. L. Zwemer, A. J. Chick, and A. E. Miller, "A new method for the generation and use of focused ultrasound in experimental biology," *J. Gen. Physiol.*, vol. 26, no. 2, pp. 179–193, Nov. 1942.

[12] J. G. Lynn and T. J. Putnam, "Histology of cerebral lesions produced by focused ultrasound," *Am. J. Pathol.*, vol. 20, no. 3, pp. 637–649, May 1944.

[13] W. J. Fry, J. W. Barnard, E. J. Fry, R. F. Krumins, and J. F. Brennan, "Ultrasonic lesions in the mammalian central nervous system," *Science*, vol. 122, no. 3168, pp. 517–518, Sep. 1955.

[14] W. J. Fry, W. H. Mosberg, J. W. Barnard, and F. J. Fry, "Production of focal destructive lesions in the central nervous system with ultrasound," *J. Neurosurg.*, vol. 11, no. 5, pp. 471–478, Sep. 1954.

[15] A. Kyriakou, E. Neufeld, B. Werner, M. M. Paulides, G. Szekely, and N. Kuster, "A review of numerical and experimental compensation techniques for skull-induced phase aberrations in transcranial focused ultrasound," *Int. J. Hyperthermia*, vol. 30, no. 1, pp. 36–46, Feb. 2014.

[16] H. H. Pennes, "Analysis of tissue and arterial blood temperatures in the resting human forearm," *J. Appl. Physiol.*, vol. 1, no. 2, pp. 93–122, Aug. 1948.

[17] S. A. Sapareto and W. C. Dewey, "Thermal dose determination in cancer therapy," *Int. J. Radiat. Oncol.*, vol. 10, no. 6, pp. 787–800, Apr. 1984.

CHAPTER 2

ADAPTIVE MODEL-PREDICTIVE CONTROLLER FOR MAGNETIC RESONANCE GUIDED FOCUSED ULTRASOUND THERAPY

2.1 Introduction

Magnetic resonance image-guided focused ultrasound (MRgFUS) is a promising noninvasive and radiation-free treatment modality that has been used to treat illnesses ranging from several types of cancer [2]–[9] to neurological disorders such as essential tremor [10]. In cancer therapy, MRgFUS has the advantage, compared to radiation therapy and chemotherapy, that dose delivery can be monitored during treatment and its effects on tissues can be observed relatively quickly.

While heating a tumor to sufficiently high temperatures will induce tumor necrosis, doing so accurately, with no collateral damage to normal tissue, and within practical treatment times is a major concern [3], [11]. Such time concerns are present in current FDA approved treatments of uterine fibroids [12] and will become increasingly prevalent when large malignant tumors located near critical tissues are

treated due to the enhanced need for dose delivery accuracy and normal tissue safety – both of which lead to slower treatments. Thus, it is critical to deliver thermal dose as time-efficiently as possible, and this can only be achieved using both computerized control systems designed specifically to minimize treatment times and protect critical tissues, and optimal treatment planning.

Early investigations into treating large tumors with focused ultrasound optimized a series of sequential, point-by-point, sonications [13]–[15]. Because their focal zones were much smaller than the tumor, many focal positions were required, and it was concluded that to protect healthy tissues in the transducer's near-field, a cooling period of 30-90 s must be inserted between every 5-20 s heating pulse [3], [11]. Such cooling periods allowed each successive pulse to be initiated at the same basal condition, thus providing for more uniformly applied heating pulses. However, such interpulse delay resulted in long treatments and the optimal delay that avoided normal tissue damage varied for each scenario.

Many temperature controllers have been introduced for hyperthermia to better account for the variability in heating *in vivo* tissues [16]–[19], with an emphasis on creating and maintaining a small, uniform temperature elevation over a large region. These were feedback controllers that required *a priori* knowledge for tuning, and their stability could be compromised if the control parameters were improperly tuned or if they changed during treatment. Other temperature controller work has sought to circumvent the interpulse cooling period in focused ultrasound surgery (FUS) treatments by increasing the volume heated via rapid switching of the focal zone among several locations [20]–[24]. Using multiple foci or rapid phased array steering

effectively defocuses the focused ultrasound beam; thus, trading increased heated volume for decreased heating speed. Such multipass (or volumetric) heating strategies have been combined with magnetic resonance temperature imaging (MRTI) feedback to make controllers that seek to optimize a fixed treatment trajectory, such as spiral trajectories [20]–[22], and concentric circles [23], [24]. These volumetric heating strategies have demonstrated that MRgFUS can create consistent ablation regions *in vivo*, and they have the advantage of being easier to control with currently achievable MRTI sampling intervals because they raise the temperature of tissues more slowly. However, these controllers are constrained to a single volumetric ablation strategy, and rely on high acoustic power to achieve acceptable treatment times [23], and thus may not be appropriate for all tumor geometries or locations. The ability to conform the heated region to the target tissue geometry has successfully been shown in catheter-based systems [25]–[27], and this spatial temperature control improved the specificity of the ablated region. However, all of the aforementioned controllers have focused on controlling temperature, not thermal dose, and no direct protection for healthy tissues was provided.

Therefore, unmet needs exist, especially in the area of time-optimal control of thermal dose that ensures safety for critical normal tissues and that can accurately conform thermal dose delivery to an arbitrary shape. The adaptive model-predictive controller (AMPC) presented here addresses these needs primarily by augmenting the MRTI measurements with model-based predictions of the future temperatures and thermal doses to be delivered during both heating and cooling periods. Using model-prediction, the AMPC reduces treatment times by anticipating thermal dose that will

be delivered to the tissue in the future, thereby increasing the accuracy of dose delivery and decreasing the dose delivered to healthy tissues. Unlike temperature controllers, the AMPC is concerned with controlling thermal dose, and because of the highly nonlinear accumulation of dose with temperature, model-prediction is critical to delivering the target dose as quickly and accurately as possible. The controller by Arora *et al.* [28] also controlled thermal dose using model-prediction, however that controller was restricted to 1D tumors and the model's complexity required *a priori* knowledge, which would be difficult or time consuming to acquire clinically. The present AMPC is substantially different from previous work as it identifies and dynamically adapts the heating model during treatments, making the controller practical for treatments with any number of sonication points. This also makes its predictions robust to changes in tissue properties that may occur during treatment and eliminates the need for lengthy pretreatment model identification. Furthermore, the AMPC does not require any parameter tuning or *a priori* knowledge of tissue parameters.

To ensure treatment safety, two factors are critical: 1) the controller must have a means for protecting healthy tissues, and 2) the controller must monitor a sufficiently large region surrounding the treatment volume and the transducer's beam path for undesired heating (for example, in the transducer's near field [29], [30], or because of reflections from tissue-bone interfaces [6], [31], [32]). To address the first safety factor, the controller enforces configurable temperature constraints on tissues selected by the clinician thus providing a direct mechanism to limit, or eliminate, undesired dose delivery in a flexible manner that can favor safety over speed, or vice versa, at the

clinician's discretion. Moreover, this explicit safety feature is enhanced by the model-prediction feature which implicitly reduces normal tissue dose by reducing heating times. The second safety factor motivates the use of 3D MR imaging that delivers temperature measurements to the controller with high spatial resolution and a large field-of-view (FoV) [33], [34]. However, both of these imaging requirements accentuate an existing drawback of MR temperature imaging, that of a relatively long interval between measurements (1-8 s). Without model-prediction, the highly nonlinear nature of thermal dose combined with long measurement intervals makes accurate measurement and control of thermal dose difficult; the AMPC helps alleviate this problem by supplementing model-predicted temperature and thermal dose estimates between MRTI measurements.

Finally, the controller presented here will optimize heating times along any path selected and is not limited to spirals, circles or lines, thus allowing the ablated volume to be conformed to the shape of the target. During therapy, the clinician retains full supervisory control while leveraging a computer's ability to rapidly monitor and adjust many parameters simultaneously.

The AMPC was tested *in vivo,* and simulations were used to evaluate the tradeoffs among competing controller parameters, to demonstrate the controller's path independence, and to evaluate how model-prediction affects treatment time and the accuracy of thermal dose delivery.

2.2 Materials and Methods

2.2.1 Controller Design

2.2.1.1 Overview

The adaptive model-predictive controller has the potential to facilitate treatments that are fast, reliable, and safe, and it supports clinicians by automating tasks that are difficult and time consuming for humans. The controller's central goal is to automatically deliver a target thermal dose to a defined target tissue volume as quickly as possible while simultaneously safeguarding critical tissues. The clinician provides overall treatment supervision beginning with identification of two classes of voxels on the patient's anatomical MR images: (1) treatment voxels (TVs) to be treated to a target thermal dose, and (2) protected voxels (PVs) to be safeguarded by limiting their maximal temperatures.

Figure 2.1a shows a simple example with nine treatment voxels and 14 protected voxels; voxels not assigned (NA) to either class require neither ablation nor protection (e.g., tumor margin or other noncritical tissues). A treatment is completed once all TVs have received their target thermal dose (TD) as measured in cumulative equivalent minutes at 43°C (CEM_{43}) [35], given by:

$$CEM_{43} = \int_0^t R^{T-43} dt \tag{2.1}$$

where T is the voxel's MR-measured temperature, and $R = 2$ when $T \geq 43$°C or $R = 4$ when $T \leq 43$°C. In this work, the small thermal dose that accrues below 42°C was neglected. A target dose of 240 CEM_{43} was used throughout this study, as this is a

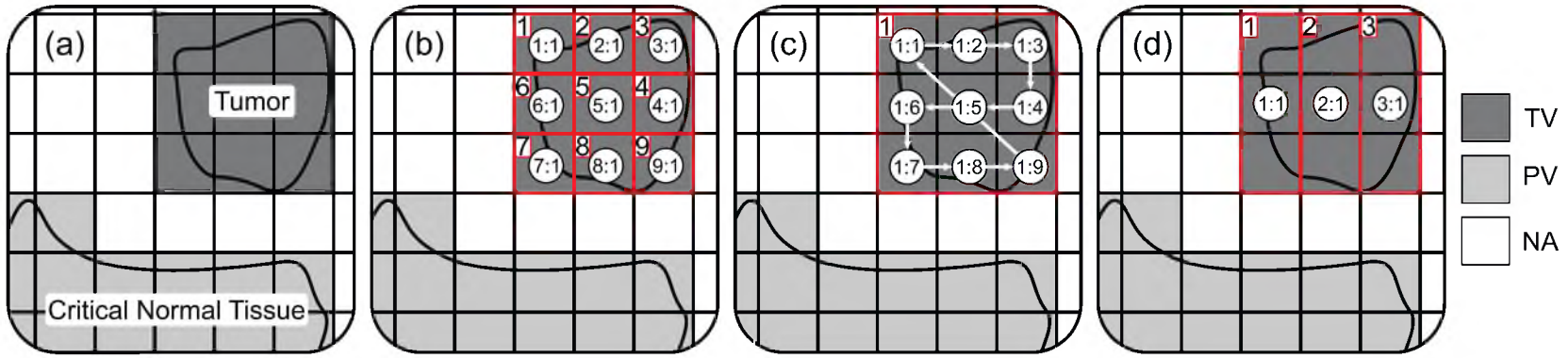

Figure 2.1: Three example controller treatment plans for a simplistic treatment. **(a)** MRI slice of patient taken perpendicular to the ultrasound beam-axis, on which the clinician identifies nine treatment voxels (TVs) and 14 protected voxels (PVs). The clinician groups TVs into cells (with each cell containing one or more TVs). During treatment, each cell is ablated sequentially as a "minitreatment" using a clinician-selected focal zone trajectory. **(b)** Plan 1 – single-pass heating: example of one extreme (one TV per cell) where the tumor is broken into nine treatment cells (number outlined in red at top left), each with only a single TV. Each cell is ablated while the focal zone is stationary at the circled location for the cell. The first number within each circle indicates the associated treatment cell of the focal position, while the second indicates the ordering of focal positions within the cell. For example, treatment of the first cell begins with the focal zone dwelling at position 1:1 until the controller's model predicts that the cell's single TV has been sufficiently heated, at which time treatment advances to the second cell (focal zone dwelling at location 2:1), and so on until finally reaching the ninth cell with the focal zone dwelling at location 9:1. **(c)** Plan 2 – multipass (volumetric) heating: the opposite extreme (all TVs in one cell) where all TVs are assigned to a single treatment cell that is ablated by repeatedly scanning the focal zone through positions 1:1, 1:2, …, 1:9, until the controller predicts the entire cell is treated. **(d)** Plan 3 – example of one possible treatment plan between the two extremes of Plans 1 and 2. The tumor is broken into three treatment cells, each of which is assigned three treatment voxels. Treatment begins with the focal zone stationary at 1:1 until all three TVs in its associated cell are predicted to receive their target dose, at which point the controller repeats the heating process for the second cell by moving the focal zone to location 2:1, and so on until all three cells are treated.

commonly used conservative threshold for histological tissue damage [36]–[39]. However, some tissues can be damaged at lower thermal doses [40] and the user is free to set the target dose that best suits their application. When calculating thermal dose, the controller assumes a linear temperature change between the discrete MR temperature measurements.

Many tumors will consist of a large number of TVs, so to provide flexibility in implementing their preferred treatment plan, clinicians divide the tumor into treatment cells (with each cell containing one or more treatment voxels) during pretreatment planning. The controller sequentially ablates each treatment cell as part of a series of individual minitreatments, and will heat each cell for the minimum time predicted for all of its treatment voxels to reach the target dose by the end of the treatment. The treatment plan parameters that must be specified are summarized in Table 2.1, while Figures 2.1b-d illustrate three example controller treatment plans for a simple treatment. Note that the applied transducer power is fixed during treatment, and that automated algorithms can greatly simplify treatment plan setup once a high-level treatment strategy (i.e., single-pass, multipass, etc.) is selected by the clinician. Regardless of the treatment plan, the controller's model anticipates the future dose to be delivered to each cell after the focal zone moves to subsequent locations. This feature allows the controller to advance to the next treatment cell before all of the TVs in the current cell reach their target thermal dose, thus saving time.

MRTI allows the controller to monitor the TVs' and PVs' temperatures at discrete times during treatment and determine: (1) if the temperature of any PV has exceeded its specified safety limit, at which time the controller turns off the ultrasound

Table 2.1: Summary of treatment plan parameters

Treatment Plan Parameter	Normally Specified By Clinician†	Automatically‡
Classifying regions as TVs or PVs	✓	
High-Level Treatment Strategy (single vs multiple pass, path type, starting location, focal point spacing)	✓	
Number of Treatment Cells		✓
Sequential Ordering of TC's		✓
Assignment of TVs to Treatment Cells		✓
Safety temperature thresholds: T_{ON} & T_{OFF}	✓	
Cooling Model Parameters	✓	
Heating Model Parameters		✓
US Power Level (constant)	✓	

†Parameters that can only be assigned by a clinician. ‡Parameters that could be assigned automatically by an algorithm. TV = Treatment voxel, PV = Protected voxel, TC = Treatment Cell.

power; and (2) if all TVs in the cell have reached their desired switching dose (see below), at which time the controller begins heating the next cell.

2.2.1.2 Treatment voxel model prediction

A real-time 3-D controller requires computationally efficient models so that predictions can be completed in a fraction of the temperature sampling interval. Thus, the AMPC uses a simple, flexible, exponential heating and cooling model for each treatment voxel, as follows:

$$T_{heat_i}(t) = A_i + B_i(1 - \exp\left(-\frac{t}{\tau_{H_i}}\right)$$
$$T_{cool_i}(t) = C_i - \mathrm{D_i}\exp\left(-\frac{t}{\tau_{C_i}}\right) \quad (2.2)$$

here i indicates the i-th treatment voxel, A_i is the initial temperature before heating, C_i is the final temperature after cooling, B_i and D_i are the overall temperature changes associated with heating and cooling, respectively, and τ_{H_i} and τ_{C_i} are the exponential time constants for heating and cooling, respectively. A_i is obtained dynamically from the temperature measurements, while C_i is set to 37 °C for all voxels as a conservative estimate. The heating terms B_i and τ_{H_i} can be estimated before beginning the treatment and are subsequently derived and adapted during treatment as each new set of temperature measurements arrive. The cooling parameter D_i is updated dynamically by subtraction of C_i from the peak temperature measured during heating, while C_i and τ_{C_i} are set in advance by the clinician and fixed during treatment.

To minimize treatment time, the controller uses the model to anticipate three aspects of the future temperatures of the TVs in the active treatment cell: (1) heating time prediction – the heating time remaining for the TVs to reach their switching dose; (2) cooling dose prediction – the TVs' temperatures, and concomitant thermal doses, predicted to occur during the period when the controller has advanced the focal zone to subsequent treatment cells, and; (3) peak temperature prediction – the peak temperature that each TV will reach at the time when heating of the current cell ends. These three model-based anticipation features allow the heating power to be moved to the next cell earlier than it would be otherwise, thus minimizing heating time and,

most importantly, the amount of concurrent heating of protected tissues.

2.2.1.2.1 Heating time prediction. This feature iteratively calculates the shortest heating time remaining such that all TVs in a treatment cell will reach their target dose by the time the tissue has cooled to $\leq$ 42°C. Note that a TV's switching dose, the thermal dose delivered at the time the heating of a cell ends, is less than the TV's target dose because the cooling prediction (described below) is performed at each iteration. Heating time prediction also saves time by allowing the controller to switch from one cell to the next between MRTI measurements since for a given MRTI sampling interval (e.g., 5 s), it frequently occurs that a cell's TVs will all have reached the switching dose just after one temperature measurement has been made (e.g., 1 s after). Thus, if prediction were not being used, and so the controller waited until the next measurement arrived before advancing to the subsequent cell, 4 s of unnecessary heating would have been applied, thereby over-treating the tumor (not detrimental) but, more seriously, unnecessarily heating the protected voxels. While not necessarily a concern for a single heating pulse, the effect in the normal tissue is cumulative due to overlap of the SAR pattern in the near-field. This feature can reduce the penalties incurred when increasing the MRTI sampling time, which can in turn improve temperature measurement precision, increase field-of-view, or improve spatial resolution.

2.2.1.2.2 Cooling dose prediction. The cell's TV temperatures and thermal doses are predicted for the future time period after the controller has advanced the focal zone to the next treatment cell. Again, this allows the controller to move to the next treatment cell earlier rather than waiting for the entire target dose to be delivered

during the heating period.

2.2.1.2.3 Peak temperature prediction. This feature is activated once the heating time prediction mode schedules the transition to the next cell. When a cell is heated for only part of an MR acquisition interval, the peak temperature of the TVs may not be measured by MRTI, which could result in an underestimate of the true thermal dose delivered. This is important due to the strong nonlinearity of thermal dose that results in large doses being delivered in very short times at high temperatures. The controller corrects for this by supplementing the discrete MRTI measurements with continuous, model-predicted TV temperatures up to the switching time. This improves knowledge of the actual dose delivered and mitigates the effects of longer MRTI sampling durations.

The computational simplicity of this model allows the controller to rapidly adapt the heating model of each TV in the active cell after receiving a new set of MRTI measurements. Consequently, any changes to the tissue environment that impact the rate of heating (e.g., increased or decreased blood flow or changes in ultrasound attenuation) will automatically be taken into account. Furthermore, because the heating model is continuously updated during treatments, its predictions need only be accurate until the next measurement is received, not for the entire heating duration. Adaptation (updating of parameters in Eqn. 2.2) is performed by a constrained least-squares error fit, using Matlab's *fmincon* function, to at least, the last N_{min} measurements and at most, the last N_{max} measurements since heating began in the current cell. Both N_{min} and N_{max} are user specified parameters, but for this study setting N_{min} = 2 and $N_{max} = 3$ was found to identify accurate models. If the MRTI

sampling rate is slow relative to the heating rate, so that the heated cell gets fully treated before N_{min} MRTI samples are acquired ($N < N_{min}$), then a model cannot be dynamically identified. In this case, the controller will make predictions based on an initial-guess model, if provided, until a model can be identified dynamically ($N \geq N_{min}$), or in the last resort, it will disable heating-prediction. From the perspective of minimizing heating time, this is a drawback. However, this is not a problem from the point of view of delivering the target dose because the controller is monitoring the thermal dose accrued in all TVs, and thus at the next MRTI measurement it will detect that the target dose has been achieved and advance to the next cell. The simplicity of the exponential model is also advantageous because it minimizes the need for *a priori* knowledge of tissue properties or for pretreatment parameter identification, thus reducing the patient's and clinician's time spent in the MR facility.

2.2.1.3 Protected voxel safety

The controller safeguards protected voxels by enforcing a pair of user-configurable temperature constraints: T_{OFF} and T_{ON}. The controller disables the ultrasound beam (triggering a cooling period) when the temperature of any PV exceeds T_{OFF}, and resumes heating once all PVs are below T_{ON}. Each PV can be assigned unique constraint temperatures; for example, to more rigorously protect a particular area. Using temperature constraints is a conservative and flexible approach for limiting patient pain and protecting against tissue damage due to thermal dose. The effect of increased treatment safety on treatment time was examined in simulations.

2.2.1.4 Additional controller features

The AMPC has several additional noteworthy features. First, measurement is given priority over prediction; i.e., if the heating model has under-predicted the actual thermal dose delivered during a measurement interval, and the next measurement confirms that all of the cell's treatment voxels have actually received their target dose, the controller disregards the prediction and begins treatment of the next cell. Second, the controller continuously monitors and updates the thermal dose of all voxels in the imaging volume so if the heating of a given cell is interrupted by a safety violation, but the cell reaches its target dose during the subsequent safety-triggered cooling period, the controller will automatically advance to the next cell once the PVs reach T_{ON}. Finally, as a "fail-safe" measure, if any TVs have not reached their target dose by the end of the treatment, then the controller will perform a "clean up" pass to deliver any missing dose.

2.2.2 Simulations

All simulations treated a cylindrical tumor of radius 7 mm and height 10 mm (1539 TVs) positioned in the center of a homogenous 10 x 10 x 10 cm tissue volume (Figure 2.2a) with a finite-difference grid resolution of 1 x 1 x 1 mm. A 4 x 4 x 3 cm volume of protected voxels (50,430 PVs in total) was identified starting at the ultrasound beam's plane of entry into the simulated volume and extending 3 cm into the volume, leaving 1.5 cm of unassigned "tumor margin" voxels between the PVs and the bottom edge of the tumor (Figure 2.2b). The simulated transducer was a 256-element phased-array operating at 1 MHz (focal distance of 13 cm, aperture diameter of 14.5 cm, f-number = 0.90). The transducer was positioned in water 8 cm from the

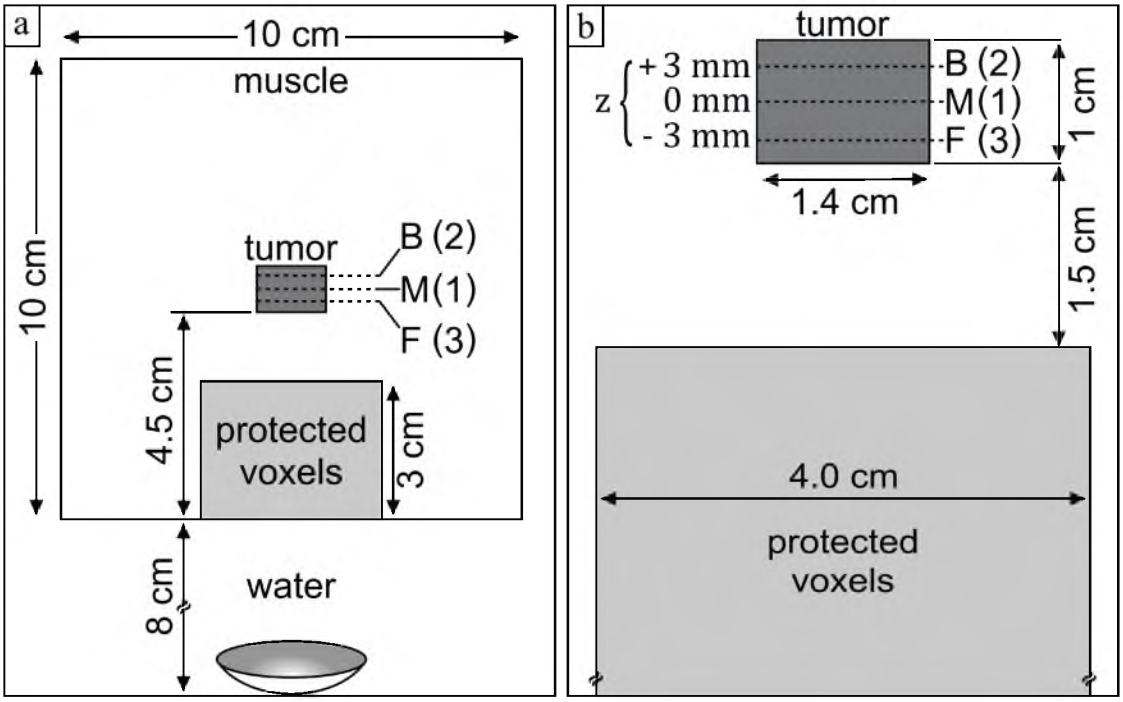

Figure 2.2: Configuration of simulation volume. **(a)** The ultrasound beam propagates through 8 cm of water before entering the 10 x 10 x 10 cm tissue volume of muscle with a cylindrical tumor centered within it. **(b)** Zoomed-in view of the tumor and protected voxels shown in (a). The tumor, (radius = 0.7 cm, height = 1 cm) is subdivided into three planes, which are visited in the order (M) middle (z = 0 mm, geometric focus), (B) back (z = +3 mm), (F) front (z = -3 mm).

simulated volume.

Two single-pass treatment plans (Figure 2.3) were simulated: (1) single pass–hottest neighbor (SP-HN) and (2) single pass–square spiral (SP-SS). For both treatment plans, the trajectories shown in Figure 2.3 were replicated in each of three planes shown in Figure 2.2b. Treatment progressed in axial "stacks," each of which consisted of a single treatment cell from each plane, with the three cells in each stack ablated in the order: middle ($z = 0$ mm), back ($z = +3$ mm), front ($z = -3$ mm). There were 149 treatment cells per plane (447 cells total), yielding an average of ~3.4 TVs/cell.

While the two treatment plans have the same number of cells, focal positions, and average number of TVs per cell, they differ in the sequence in which the cells are treated. The hottest-neighbor treatment plan takes advantage of the adjacency of successive axial stacks and the thermal buildup resulting from the superposition of SAR patterns from the most recently heated cells. The square-spiral initially shares some of that adjacency, and also takes advantage of thermal buildup in the tumor by proceeding sequentially from the center of the tumor to its periphery; however, as treatment progresses its treatment cells become increasingly farther apart and more independent from its recently heated predecessor cells.

The hybrid angular spectrum ultrasound simulation method [41] was used to efficiently precompute the 447 SAR patterns for each focal zone position required for each plan. The simulated SAR patterns were used in conjunction with Pennes' bio-heat transfer equation [42], in which the metabolic power generated by the tissue was neglected, the specific heat of the tissue and arterial blood were assumed to be approximately equivalent, and conduction and perfusion were assumed to be scalars,

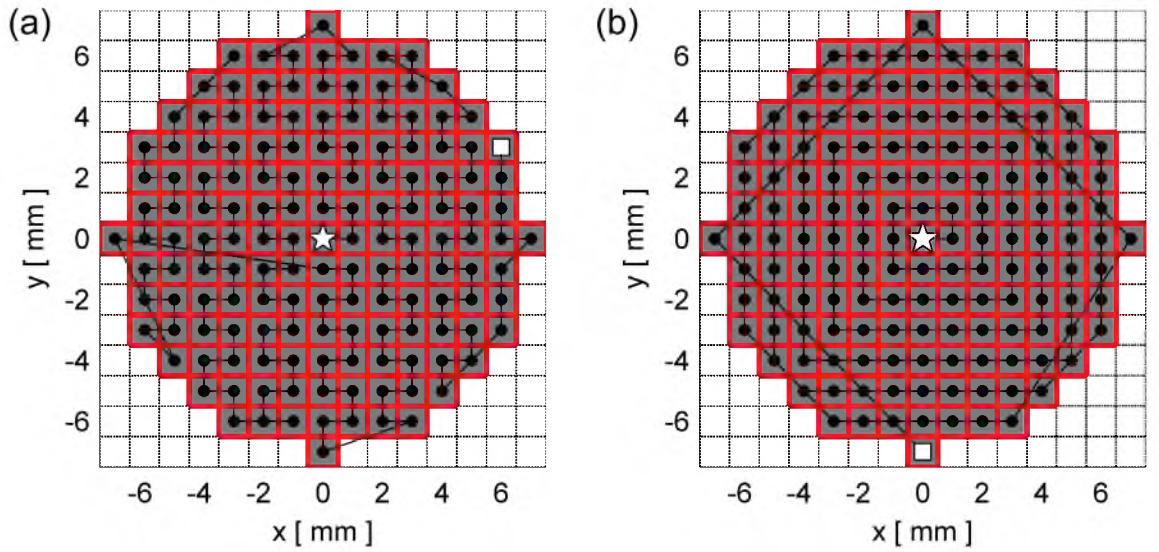

Figure 2.3: Middle plane (M) for the two simulated treatment plans: **(a)** single pass–hottest neighbor **(b)** single pass–square spiral; Gray = treatment voxels; Red outline = treatment cell; Black dot = focal zone position for a cell. The starting focal zone location is marked with a white star, while the ending location is marked by a white square. The focal zone dwells at each location until the associated cell's treatment is completed. Note: although not visible in this drawing, each treatment cell includes multiple TVs (~3.4 on average) that extend in the direction perpendicular to the slice shown.

leading to the simplified equation:

$$\rho_t c_t \frac{dT(x,y,z,t)}{dt} = Q_a(x,y,z,t) + \ k\nabla^2 T - w_b c_t (T - T_b) \qquad (2.3)$$

where T is the tissue temperature in °C; x, y, z are the spatial coordinates in m; t is time in s; ρ_t is the tissue density in kg/m^3; c_t is the tissue's specific heat in J/kg/°C; Q_a is the absorbed ultrasound power per unit volume in W/m^3; k is the tissue's thermal conductivity in W/m/°C; w_b is the blood perfusion rate in kg/m^3/s, and T_b is the temperature of the blood in °C. T_b and all boundaries were set to the volume's initial temperate, $T_0 = 37$ °C. An explicit finite-difference solution (Euler's method) was used to update temperatures between two time periods, T_{i+1} and T_i, separated by Δt. For each time step, the simulation used one precomputed Q_a^i pattern scaled to the desired power magnitude. Arbitrary focal zone trajectories can be simulated by successively changing the Q_a^i pattern for each corresponding time step. The simulation time step was $\Delta t = 0.1\ s$ except when the controller's predicted heating time was not evenly divisible by Δt (e.g., 0.25 s), in which case a single shorter time step equal to the remainder (e.g., 0.05 s) was used for the last time step.

The MR sampling interval Δt_{MR} is the duration required to acquire each MR temperature measurement. While the finite difference thermal model operates at Δt to ensure numerical stability, the controller is only given temperature information every Δt_{MR}. Furthermore, at the $i\text{-}th$ MR measurement, the center of k-space is usually sampled at the midpoint of the sampling interval, i.e., at $t_{m_i} = \Delta t_{MR}(i - 0.5)$,

thus the temperature reported at the end of an interval, $t_{e_i} = i \cdot \Delta t_{MR}$, is most indicative of the tissue temperature at t_{m_i}. Effectively, the controller is making decisions at t_{e_i} based on measurements at t_{m_i}, a delay of $\frac{\Delta t_{MR}}{2}$, and this real-world effect is included in the simulations.

The following tissue properties were assigned to all voxels; these values fall within published ranges for biological tissues [43], [44]: US attenuation = 0.05 Np·cm^{-1}·MHz^{-1}, speed of sound = 1517 m·s^{-1}, ρ_t = 993 kg·m^{-3} , k = 0.58 W·m^{-1}·°C^{-1}, c_t = 4187 J·kg^{-1}·°C^{-1}, w_b = 0.5 kg·m^{-3}·s^{-1} . Unless otherwise noted, simulations used: Δt_{MR} = 3.0 s, T_{OFF} = 43.0 °C, T_{ON} = 41.5 °C, and an applied power of 15 W. At this power, the resulting max/min peak absorbed power densities in the treatment cells were 1.97 x 10^7 / 1.46 x 10^7 W·m^{-3}, which correspond to linear heating rates of 4.7 / 3.5 °C·s^{-1}.

To quantify the time savings derived from each of the major controller optimization features, simulations were performed at successively increasing levels of optimization, with each level keeping the features of the previous level and adding one more optimization feature. As a reference case, the independent heating pulses (IP) scenario was run first without any AMPC features. For this case, each cell begins at a baseline temperature of 37 °C and the cell's entire 240 CEM_{43} target dose is delivered during the heating period. Next, the different AMPC optimization levels were enabled as follows: (1) +temperature buildup: this first level of optimization illustrates the simplest benefit of using MRTI to monitor the TVs' temperatures. Rather than beginning at the baseline temperature of 37 °C (as in the IP reference case), the cell's TVs begin at the final temperatures reached after treating the previous cell. As in the

IP case, each cell receives 240 CEM_{43} and only the dose delivered while heating that cell is considered (i.e., no prior dose was accounted for, and the future dose to be delivered after the focal zone advanced to the next cell is ignored). (2) +Prior dose: adding this feature to the temperature buildup feature demonstrates the benefit of using a computer that can use MRTI to calculate the thermal dose delivered to the volume in real-time. When treatment of a new cell begins, the dose already delivered to that cell's TVs is known, and thus the controller need only deliver the remaining dose. (3) +Adaptive model-predictive control: this level adds the three predictive modes of the AMPC (described previously) to the use of temperature buildup and prior dose accounting.

In the IP reference case, only the three cells with focal zone positions along the transducer centerline at $x = y = 0$, $z = \{0$ mm, -3 mm, +3 mm$\}$ were simulated. The time to treat each of these three cells was multiplied by the number of cells in each z-plane (149) and summed to arrive at the total treatment time. This represents the minimum treatment time achievable by the independent heating pulses approach (for a given transducer power) since it ignores the inherent power losses when using phased-array steering to treat the edges of the tumor. These losses would reduce the SAR and thereby lengthen the needed heating times. All simulations were run first with safety constraints disabled, and again with safety constraints enabled (T_{ON} = 41.5 °C and T_{OFF} = 43.0 °C).

2.2.3 In Vivo Experiments

After completing development tests in phantoms, the AMPC was tested *in vivo* in rabbit thigh muscle (two rabbits, three thighs) with a target dose of 240 CEM_{43} in all

treatment voxels. Experiments were designed to test specific features of the controller. In all tests, the rabbit was positioned on its side (Figure 2.4a) approximately 11.5 cm above the transducer, which was driven by electronics from Image Guided Therapy (Pessace, France). The transducer (described in the previous section) was coupled to the rabbit with deionized water that was degassed using a custom built degassing system. Measurements from a Hanna Instruments HI-9146 (Woonsocket, Rhode Island, USA) meter confirmed that this system degassed the water to a dissolved oxygen level of $\leq$ 1.0 mg/L of water.

In order to demonstrate the controller feature that allows it to assign different numbers of TVs to each treatment cell and then automatically treat them in sequence,

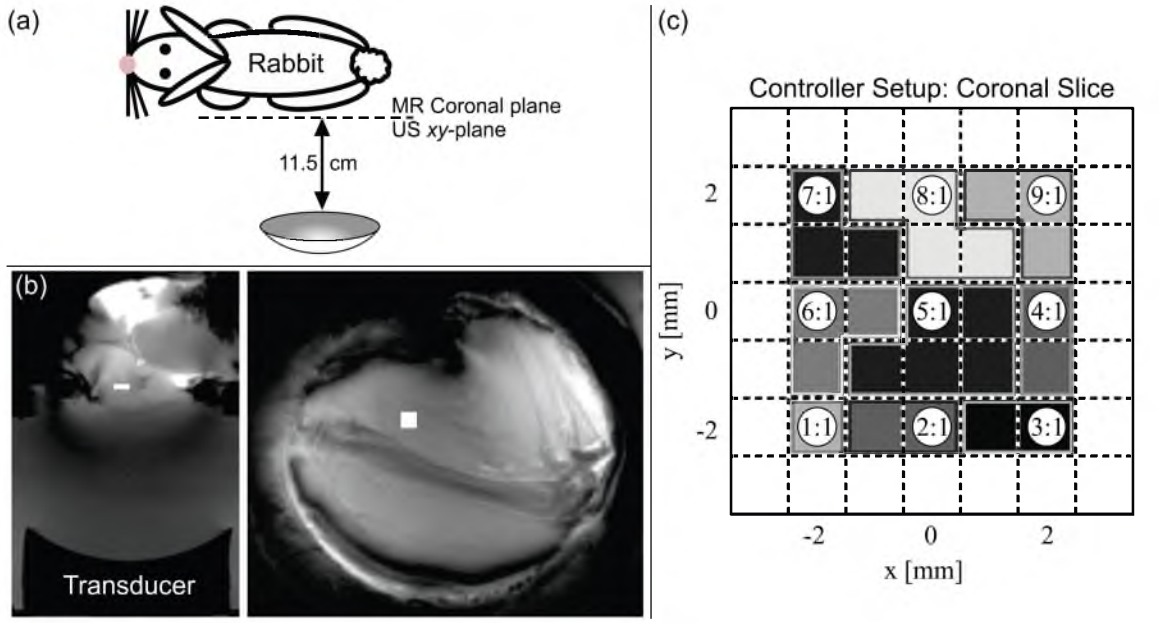

Figure 2.4: Configuration of *in vivo* experiments. **(a)** Rabbit's position during all controller tests. **(b)** Anatomical MR image of *in vivo* rabbit experiment in the transverse (left) and coronal (right) planes, respectively. White box indicates approximate treatment location for Run 1. **(c)** Controller configuration: single-pass–raster scan treatment plan with nine treatment cells covering a 5 x 5 x 3 mm volume. Each cell was heated by a single focal zone position (circles). Shading and outlines indicate to which cell each treatment voxel was assigned.

the controller was configured to treat a 5 x 5 x 3 mm treatment volume using a single-pass raster-scan treatment plan in a single plane, as shown in Figure 2.4b. The 25 treatment voxels were assigned to nine treatment cells, and each cell was sequentially ablated by dwelling at a single focal zone position. Controller Runs 1-4 used a transducer power of 20 W and had no normal tissue constraints, while Run 5 used a transducer power of 33 W and had a 16 x 16 x 3 mm region of protected voxels specified in a plane 2 cm below the treatment volume with T_{OFF} and T_{ON} thresholds of 45 °C and 41 °C, respectively. Each run was performed in a unique region of rabbit thigh that had not been ablated by previous tests, and a single short test shot was performed in advance of each run to adjust the targeting of the center cell.

Temperature measurements for controller feedback were acquired using a Siemens 3T Tim Trio MRI scanner and a segmented gradient recalled echo (GRE) echo planar imaging (EPI) proton resonance frequency shift (PRF) thermometry sequence with fat saturation. For Runs 1-4, 3D temperatures were acquired every 4.2 s in a 256 x 168 x 27 mm volume at 2 x 2 x 3 mm voxel resolution, and each measurement was zero-fill-interpolated to a voxel spacing of 1 x 1 x 1.5 mm to reduce partial volume effects [45]. Other relevant MR parameters were: TR/TE = 35 / 11 ms; flip angle = 15°; EPI factor = 9; 18 slices with 33.3% slice over-sampling; and bandwidth = 738 Hz/pixel. For Run 5, the PRF sequence was run with three 2D slices (two in the tumor, one in the protected tissue) in order to cover a sufficiently large field-of-view to monitor the protected voxels; relevant MR parameters for this sequence were: FoV = 256 x 176 mm; resolution = 2 x 2 x 3 mm (zero-fill-interpolated to 1 x 1 x 3 mm); TR/TE = 39/8 ms; flip angle = 25°; EPI factor = 1; bandwidth = 751

Hz/pixel; acquisition time = 3.7 s.

2.3 Results

2.3.1 Simulations

2.3.1.1 Treatment plan independence

To illustrate the controller's treatment plan independence, both treatment plans shown in Figure 2.3 were simulated at 15 W with and without safety constraints, and the resulting treatment time and maximum thermal dose delivered to the protected tissue are shown in Figure 2.5. With safety constraints disabled, the single pass–hottest neighbor plan was 17% faster than the single pass–square spiral plan (15 vs 18 minutes), and also reduced the maximum dose delivered to the protected voxels by 44% (282 CEM_{43} vs 500 CEM_{43}). For the practical case when safety constraints were enabled, the single pass–hottest neighbor plan was again faster than the single pass–square spiral plan (1 hour 45 minutes vs 2 hours 5 minutes), however, both plans were approximately 6-7 times slower than their unsafe cases. Importantly, however, the

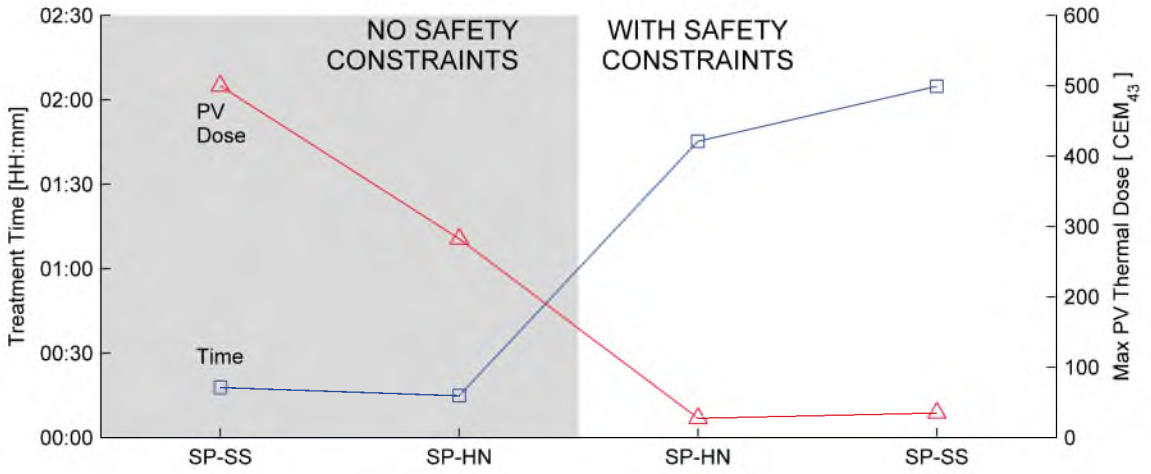

Figure 2.5: Treatment time and maximum protected voxel thermal dose as a function of treatment plan at 15 W. AMPC was used for all runs. SP-SS = single-pass–square-spiral, SP-HN = single-pass–hottest neighbor.

protected voxel dose was limited to < 27 CEM_{43} for the single pass–hottest neighbor plan and < 35 CEM_{43} for the single pass–square spiral plan.

Unless otherwise noted, the remaining simulations only consider the single pass–hottest neighbor treatment plan because it was 24% faster than the single pass–square spiral plan and delivered 23% less dose to the protected tissues.

2.3.1.2 Time savings derived from controller optimization levels

The treatment times and maximum protected voxel thermal dose resulting as each of the major controller optimization features are enabled are shown in Figure 2.6. The no-constraint half of this graph shows the time gains attainable by successively adding controller optimizations; however, all of those results yielded thermal doses in the protected voxels that exceeded the target dose for tumor ablation. For example, the +thermal buildup (+TB) case without safety constraints delivered >3000 CEM_{43} to

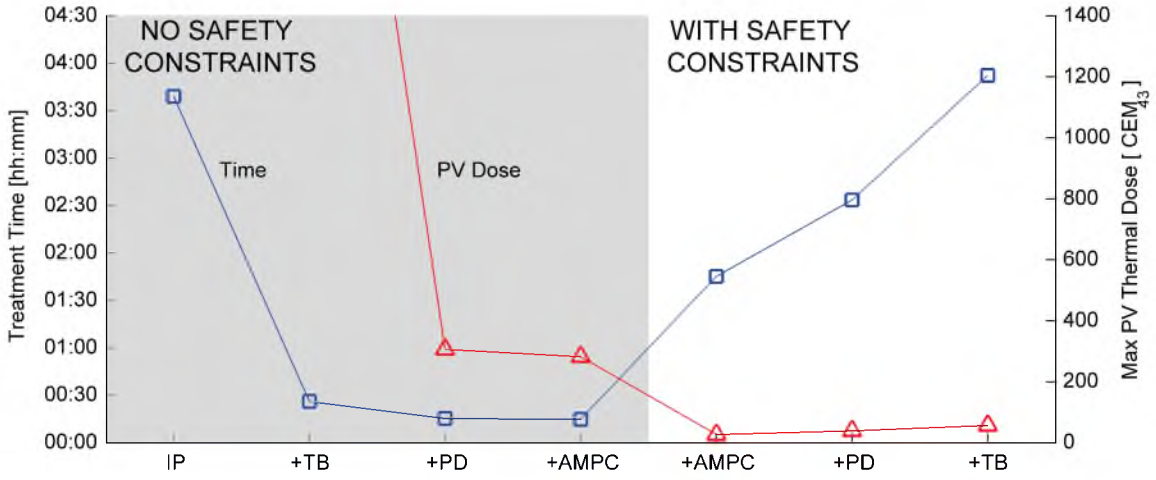

Figure 2.6: Treatment time and maximum dose delivered to protected voxels for the single pass–hottest neighbor treatment plan at 15 W as a function of optimization feature when PV safety constraints are disabled (shaded region) and enabled (white region). IP = independent heating pulses (no optimization); +TB = thermal buildup added; +PD = prior dose added; +AMPC = adaptive model-predictive control added. The maximum PV dose for +TB with no safety constraint is 3277 CEM_{43}.

the protected tissues. Thus, the no-constraint cases are of interest only to illustrate the importance of considering safety.

In the practical case when safety constraints are enabled, treatment time sequentially decreases as each optimization level is added. Enabling temperature buildup gives a treatment time of 3 hours 52 minutes, almost as fast as the independent pulses case without safety constraints (note that the IP case is artificially fast since it does not include the interpulse cooling period, often 90 s, that would be necessary to make the pulses truly independent). Adding prior dose reduces treatment time to 2 hours 33 minutes, and full AMPC is the fastest, taking only 1 hour 45 minutes; a 54% reduction compared to +TB only. The full AMPC case was also the safest case, yielding a maximum protected voxel dose of 27 CEM_{43} compared to 40 and 57 CEM_{43} for the +prior dose and +thermal buildup cases, respectively.

2.3.1.3 Safety constraint thresholds

The previous results have shown that activation of the AMPC's safety constraints reduces the thermal dose delivered to the protected voxels. Thus, to investigate the tradeoffs of different safety thresholds, multiple T_{OFF} /T_{ON} combinations were simulated.

Starting with the safety constraint thresholds used previously, T_{OFF} = 43.0 °C and T_{ON} = 41.5 °C, Figure 2.7 shows the change in treatment time and maximum protected voxel dose when T_{OFF} is decreased in 0.5 °C intervals to 42.0 °C (the temperature below which thermal dose is assumed to no longer accumulate). Then, T_{OFF} is held constant at 42.0 °C (limiting the protected voxel dose to zero) while T_{ON}

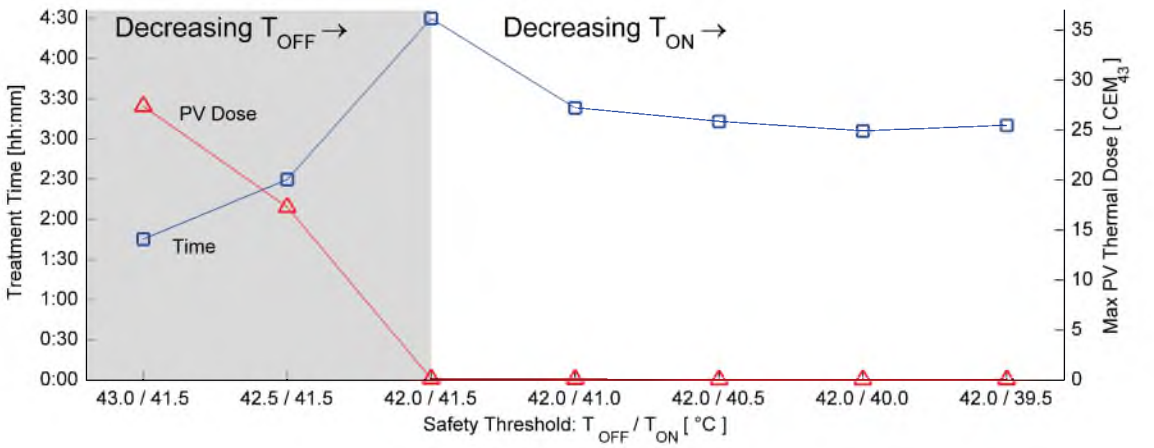

Figure 2.7: Effect of safety threshold on treatment time and maximum PV thermal dose for the single pass–hottest neighbor treatment plan at 15 W with AMPC. Shaded region: T_{OFF} reduced in 0.5 °C increments, fixed T_{ON} = 41.5°C. Unshaded region: T_{ON} reduced in 0.5 °C increments, fixed T_{OFF} = 42 °C. Placing more stringent constraints on T_{OFF} reduces dose delivered to protected voxels at the expense of increased treatment time. Reducing T_{ON} increases cooling time before the US is re-enabled, but also increases the available heating time before the next constraint violation occurs.

is decreased in 0.5 °C intervals, effectively varying the cooling duration per constraint violation. The results show that, if desired, the controller can be configured with a strict T_{OFF} value that disallows any significant thermal dose being delivered to the protected tissue; for example, when T_{OFF} / T_{ON} = 42.0/41.5 °C, protected voxel thermal dose was constrained to 0 CEM_{43}, whereas a maximum of 27 CEM_{43} was delivered to the protected voxels when T_{OFF} / T_{ON} = 43.0/ 41.5 °C. Such increased safety comes at the expense of considerably increased treatment time; e.g., the fastest treatment when zero protected tissue dose was allowed (T_{OFF} / T_{ON} = 42.0/40.5 °C) is 1.8 times as long as when 27 CEM_{43} was allowed (with T_{OFF} / T_{ON} = 43.0/ 41.5 °C).

Interestingly, when fixing T_{OFF} = 42.0 °C (to minimize protected voxel dose), Figure 2.7 shows that decreasing T_{ON}, to force longer cooling intervals, yields a net time savings until T_{ON} = 39.5 °C. After this point, the additional heating time afforded

is countered by the additional cooling time required, and total treatment time begins increasing again.

2.3.1.4 Accuracy and uniformity of thermal dose delivered

To investigate how accurately and uniformly the controller delivered the target dose to all treatment voxels, the final thermal dose distributions achieved for each controller optimization level were analyzed for the practical AMPC case of Figure 2.6: the single pass–hottest neighbor treatment plan with safety constraints enabled. The top row of Figure 2.8 shows a frequency distribution of dose for all treatment voxels in the tumor, while the bottom row shows the distribution of the doses for only the lowest dosed treatment voxel in each cell. Treatment time is dominated by the voxel that receives the lowest SAR in the cell, and thus overdosing in the other treatment voxels of the cell is expected. The target dose for all voxels was 240 CEM_{43}, and the median doses delivered to the least dosed voxel of each cell were 1676, 886, and 450 CEM_{43} for the +temperature buildup, +prior dose, and +AMPC optimizations, respectively. The safety constraint threshold was exceeded 70, 44 and 30 times for the +temperature buildup, +prior dose, and +AMPC cases, respectively. Enabling each additional controller optimization level thus makes a significant improvement in treatment quality (more accurate dose delivery and fewer safety triggered cool-down periods). The full featured AMPC delivers the target thermal dose to the treatment voxels more accurately, the fastest, and with the lowest doses delivered to the protected voxels.

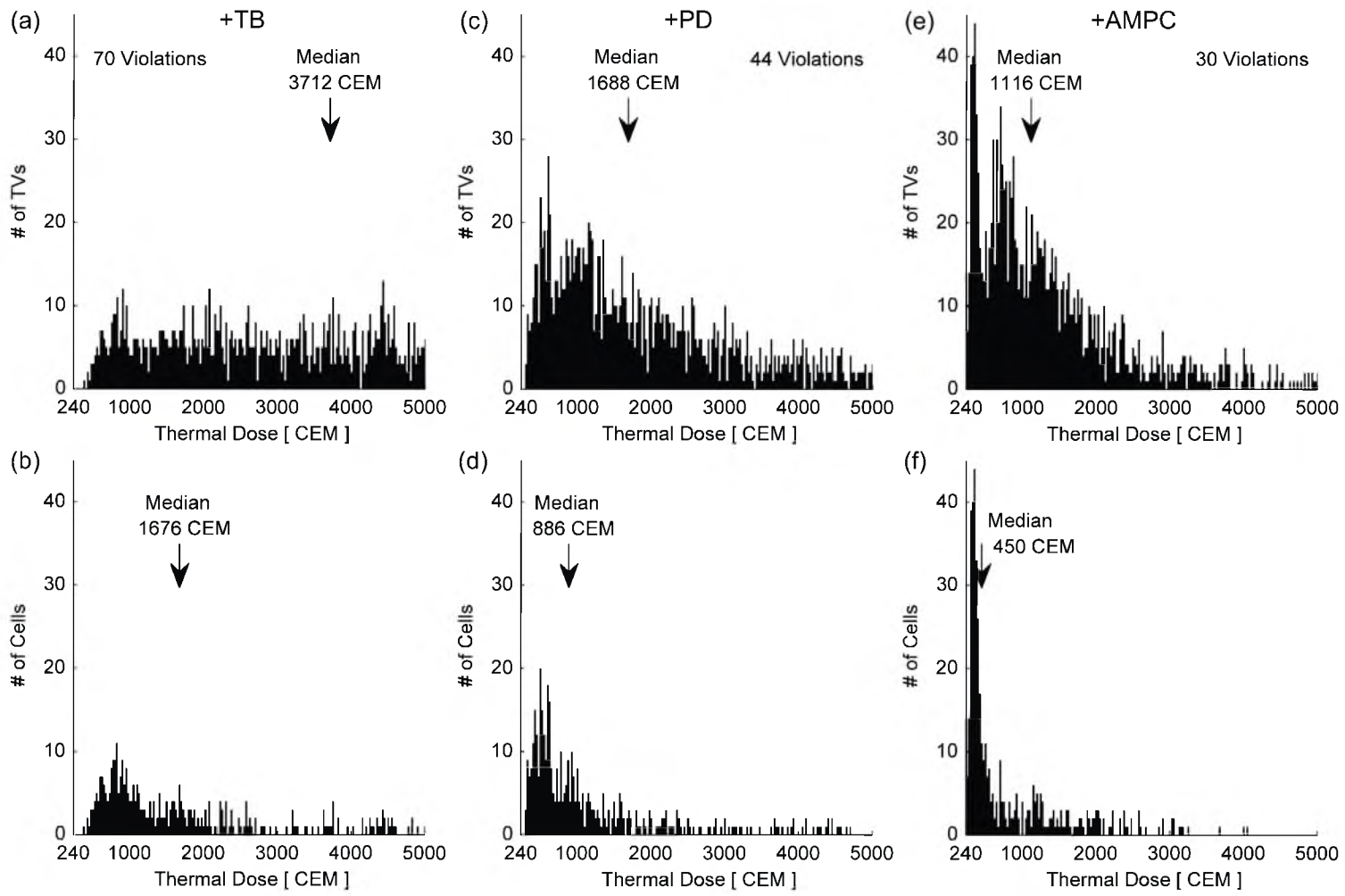

Figure 2.8: Histogram of final dose delivered as controller features are enabled. +Temperature buildup (+TB): **(a)** all treatment voxels, **(b)** minimum dose delivered to cells. +Prior dose (+PD): **(c)** all treatment voxels, **(d)** minimum dose delivered to cells. +AMPC: **(e)** all treatment voxels, **(f)** minimum dose delivered to cells.

2.3.1.5 Applied power and treatment time

When increasing the applied power magnitude there is a tradeoff between the increased rate of heating of the tumor vs that of the protected voxels. Figure 2.9 demonstrates this tradeoff for the single pass–hottest neighbor treatment plan with full AMPC optimization and safety constraints enabled. Treatment time and dose to the protected voxels monotonically decreases with higher powers, but there is a "knee" in the curve beyond which the benefits of higher power rapidly decreases.

2.3.1.6 Effect of MR sampling time

MR acquisition time is valuable currency which can be spent, for example, to increase the imaging field-of-view, improve spatial resolution, and decrease noise, but

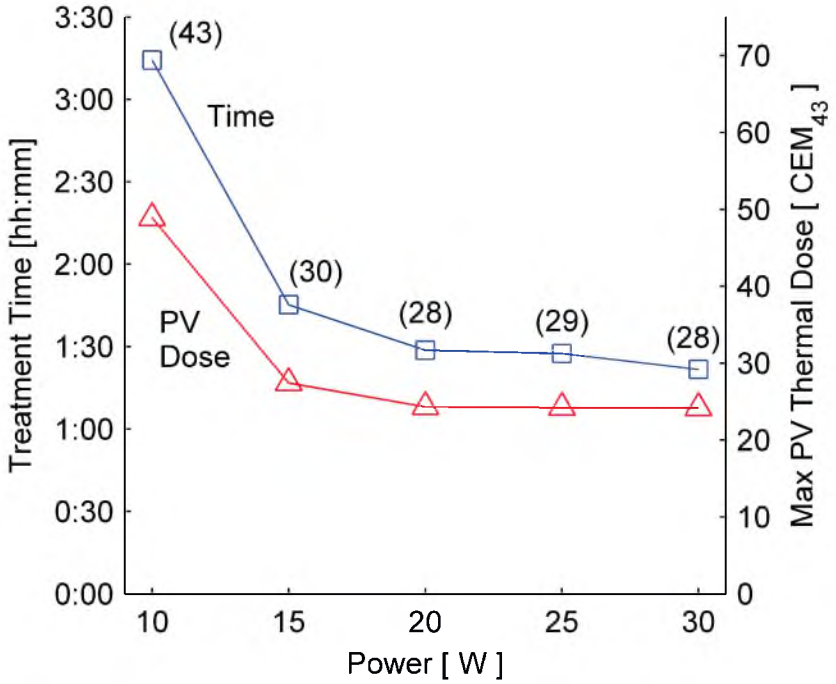

Figure 2.9: Treatment time and maximum protected voxel (PV) thermal dose as a function of applied ultrasound power for single pass–hottest neighbor treatment plan run with AMPC and safety constraints enabled. Values in parenthesis indicate the number of safety violations for each case.

these gains would be accrued at the expense of a longer interval between measurements. It would be beneficial if model prediction could help mitigate the costs of increasing the MR sampling interval and allow the clinician more freedom in selecting the imaging parameters. Simulations using the +AMPC and +prior dose optimization levels were run at a fixed power of 15 W for 1, 3, 5, and 7 s MR sampling intervals to explore the effect of MR sampling time on treatment time and dose delivered to the protected voxels. As shown in Figure 2.10, the AMPC treatment time increased by 42% when the sampling interval increased from 1 s to 7 s, while the protected tissues' maximum dose increased by 28% over the same range; however, the AMPC outperforms the +Prior Dose optimization level by 19-31% over all sampling intervals, thus illustrating how AMPC can reduce treatment times even with long MR sampling times. For the AMPC, as the sampling interval increases, the temperature overshoot above the T_{OFF} safety threshold also increases, but was < 0.2 °C for all cases.

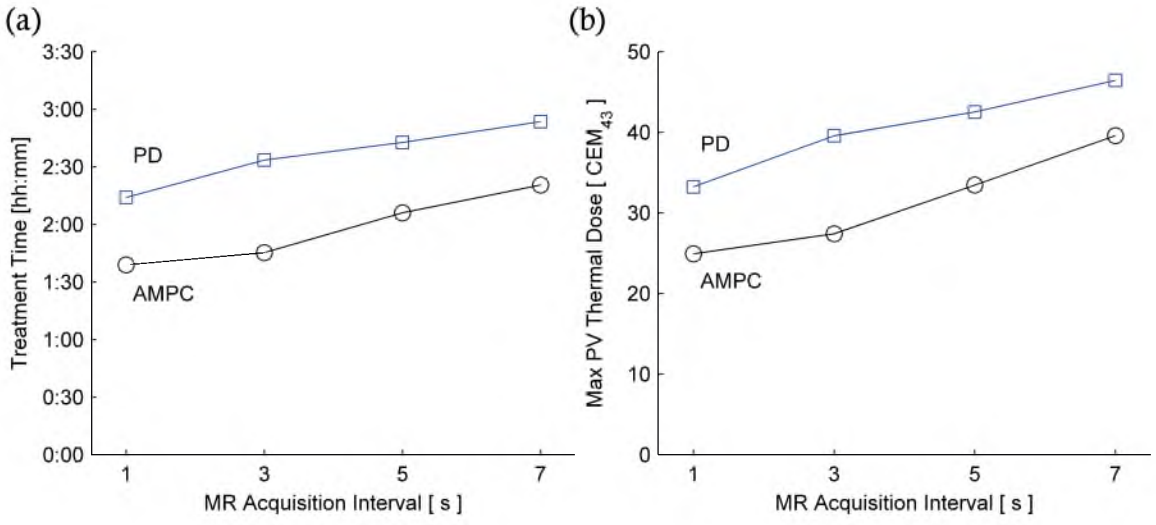

Figure 2.10: Treatment time (a) and maximum protected voxel thermal dose (b), as a function of MRTI acquisition interval; simulations run at 15 W with +AMPC or +Prior Dose optimization with safety constraints enabled using the single pass–hottest neighbor treatment plan. Implementing AMPC decreases both the treatment time and maximum thermal dose in the protected voxels for any given MR acquisition interval.

Similarly, the number of violations changed from 29 to 37 for the 1 s and 7 s MR sampling intervals, respectively.

2.3.2 In Vivo Results

2.3.2.1 AMPC repeatability

Figure 2.11 illustrates the final thermal dose deposited after each *in vivo* controller test for the treatment plan shown in Figure 2.4c. All four runs successfully delivered the target dose to all of the TVs, and the controller was able to create sharp boundaries between the target volume and surrounding tissues, with doses falling below 10 CEM_{43} after a distance of ≤ 4 mm outside of the prescribed treatment volume. The first trial (Figure 2.11a) shows signs of secondary dose delivered due to proximity of the rabbit's thigh bone to the treatment volume (see Figure 2.4b).

Of the 36 treatment cells treated in the four trials (nine cells per trial), the controller's ability to monitor the temperature and thermal dose history of the entire volume allowed for one cell to be skipped entirely because the AMPC detected that it had already received the target dose during treatment of the previous cells. In two cells the controller deferred to the MRTI measurements and advanced the treatment to the next cell because the target dose had been delivered before a heating model could be identified dynamically. Most interestingly, the controller's prediction that the switching dose for the active cell would be delivered between MRTI measurements and that the cell's target dose would be reached during cooling were borne out in 91% of cells treated.

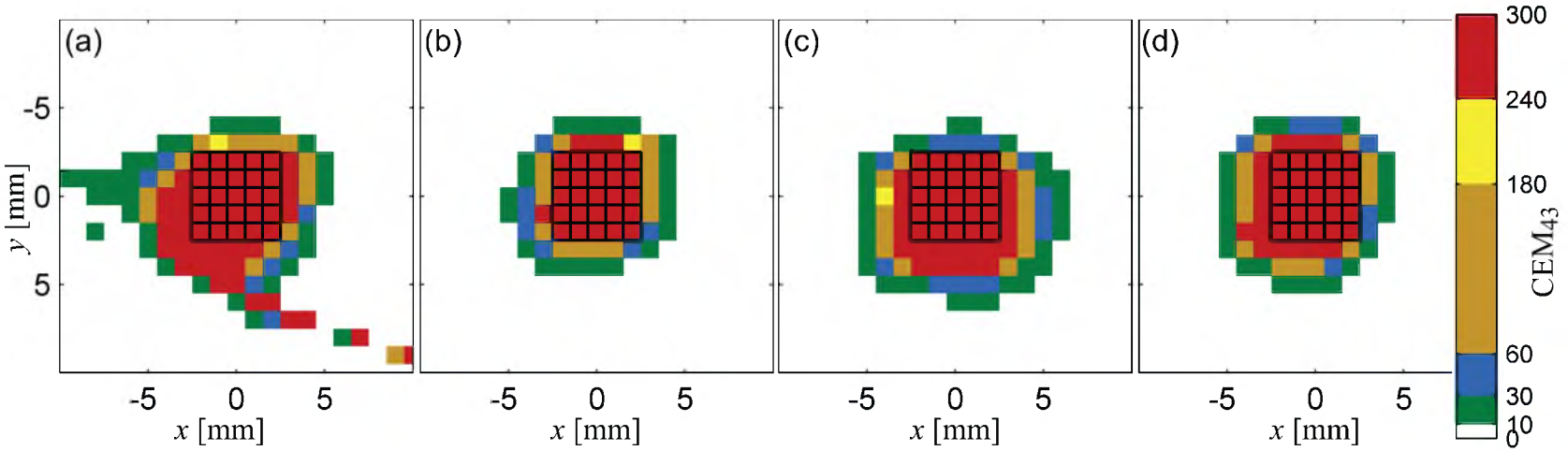

Figure 2.11: Final thermal dose maps in coronal slice of the treatment plane (perpendicular to ultrasound beam). Black squares indicate 1 x 1 x 1.5 mm treatment voxels. All treatment voxels were successfully treated, and minimal dose was deposited outside the prescribed treatment volume.

2.3.2.2 Temperature prediction accuracy during heating

The simplicity of the exponential heating model used by the AMPC for prediction is a benefit for ease of use because it can be identified and adapted during treatment. However, to evaluate the accuracy of the predictions, the temperatures predicted by the model at t_i for the following measurement at t_{i+1} were compared to the temperatures actually measured at t_{i+1} for one *in vivo* rabbit trial. Each dot of Figure 2.12 represents a measured temperature and the corresponding error in the predicted temperature. The MRTI measurements were assumed to have zero-mean Gaussian noise and calculated to have a standard deviation of $\sigma = 1.2$ °C by sampling an unheated 10 x 10 mm region of the rabbit thigh during the initial baseline temperature measurements. The results indicate that the heating model predicted the measured temperature within the measurement error, and the average prediction error was -0.2 ± 0.7 °C.

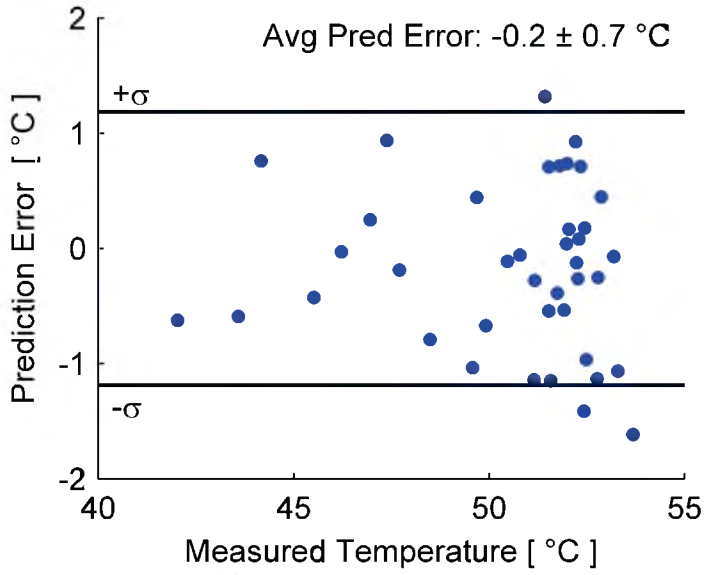

Figure 2.12: Prediction error as a function of measured temperature for all predictions made during a single treatment. MR measurements have σ = ± 1.2 °C, calculated from an unheated tissue region.

2.3.2.3 Safety constraints

An *in vivo* evaluation of the safety constraints consisted of configuring the AMPC to monitor a plane of PVs 2 cm below the treatment volume with safety thresholds that allowed high normal tissue temperatures for short intervals (T_{OFF} = 45°C and T_{ON} = 41°C). All treatment cells successfully received their 240 CEM_{43} target dose, and as shown in Figure 2.13, the controller constrained the temperature of the protected voxels by entering the cooling mode when T_{OFF} was violated and then resuming treatment after all protected voxel temperatures were $\leq T_{ON}$. This example included an additional, optional, controller feature that can be enabled to increase safety; this feature forces the PVs to cool to T_{ON} between the heating of each cell even if T_{OFF} has not been breached. While this feature slowed the *in vivo* test treatment (as did the choice of path—which was made to demonstrate the controllers features, not to deliver the fastest treatment), the AMPC constrained the maximum dose delivered to the protected voxels to 8.4 CEM_{43}.

2.4 Discussion

Our simulation and *in vivo* results show that a real-time model-predictive controller can be practically implemented for MRgFUS therapy, and can reduce treatment times, optimize any treatment path, and actively protect normal tissues. Each controller optimization feature (+thermal buildup, +prior dose, and +adaptive model-prediction) makes significant contributions to those improvements (Figure 2.6), and model-prediction reduces treatment time by approximately 55% compared to only accounting for thermal buildup. Furthermore, the reduced heating times made possible with model-prediction also result in reduced dose delivered to protected tissues.

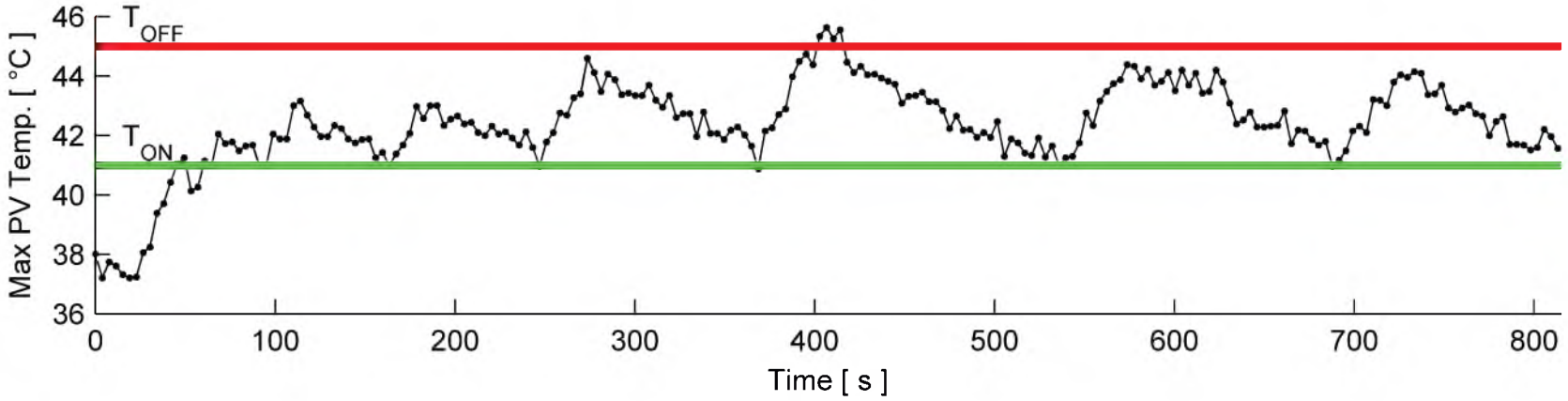

Figure 2.13: Protected voxels' maximum temperature vs time during *in vivo* treatment with T_{OFF} = 45 °C and T_{ON} = 41 °C. For this demonstration only, an additional safety feature forced the treatment of each cell to begin with protected voxel temperatures $\leq T_{ON}$. Maximum dose delivered to PVs was 8.4 CEM_{43}.

The nonlinearity of the thermal dose equation (Eqn. 2.1) makes accurate delivery of thermal dose difficult without model-predictive control (Figure 2.8). Modeling improves the accuracy of the delivered target dose by anticipating the nonlinear thermal dose effects, and has the additional advantage of reducing heating times by anticipating dose delivered during cool-down periods. The simple heating model used for prediction is sufficiently accurate (Figure 2.12), has the advantage of not needing *a priori* knowledge of tissue properties, and is amenable to on-line adaptation making the controller robust to tissue property changes during treatment. During *in vivo* evaluations, the AMPC always delivered the prescribed 240 CEM_{43} target dose to the treatment voxels (Figure 2.11) and the boundary between treated and untreated regions was sharply demarcated with <10 CEM_{43} delivered to regions ≥ 4mm away from the target volume.

While the AMPC will automatically benefit from the work of others who accelerate MR temperature measurements [34], model-prediction will always be useful in decreasing treatment time because it anticipates the future dose to be delivered after the focal zone leaves a given treatment cell. Furthermore, model-prediction provides the flexibility to trade MR sampling time for increased coverage or higher resolution measurements. For example, Figure 2.10 demonstrates that performing the single pass–hottest neighbor treatment plan with model-prediction and an MR sampling time of 5 s would achieve the same degree of safety and complete the treatment faster than if treatment were performed with a 1 s MR sampling time but without model-prediction.

Our results reinforce the previously shown [29], [30] importance of considering

the safety of healthy tissue when discussing treatment time, as unconstrained treatments can deliver >>240 CEM_{43} to normal tissues (Figures 2.5 and 2.6). *In vivo* evaluations of the configurable safety constraint showed that the AMPC reliably and automatically triggered cooling periods and limited protected voxel dose to < 9 CEM_{43} without affecting treatment efficacy. While enabling the AMPC's safety feature comes at the expense of longer treatment times, and relies upon capturing a large field-of-view (preferably with a fully 3D acquisition scheme), it is necessary for the safe treatment of clinically relevant tumors. Simulations showed the AMPC is capable of constraining dose to zero in tissues near the tumor (Figure 2.7), but the resulting treatment time may be difficult for the patient to endure. As Figure 2.7 illustrates, a more balanced selection of temperature constraints (T_{OFF}/T_{ON} = 43.0/41.5 °C) reduced thermal dose in the intervening tissues to manageable levels (< 30 CEM_{43}) while achieving a more reasonable treatment time.

We have also demonstrated that the AMPC can be used with arbitrary treatment paths defined by the user (Figure 2.5 and 2.11), which allows the treatment to be conformed to the tumor geometry and patient anatomy. Those results demonstrate that a single-pass treatment plan with small cells, each heated by a single focal zone location, is clinically practical and that path selection is important for minimizing both treatment time and dose delivered to protected tissues. Our results indicate that a treatment plan that achieves a high degree of adjacency (proceeding from the completed cell to a nearby cell) takes maximum advantage of the temperature buildup in the tumor. This explains why the single pass–hottest neighbor treatment plan is 24% faster and delivers 23% less thermal dose to the protected voxels than the

single pass–square spiral plan. Path selection becomes critically important once safety constraints are enabled since every safety-triggered cool-down period causes thermal buildup in the tumor to dissipate. Therefore, a path with a high degree of adjacency will more fully leverage the benefit of thermal buildup and maximize the volume treated per constraint violation. While several treatment paths have been demonstrated, further studies into optimal path selection are needed.

Our results with a real-time controller agree with previous optimization findings [46], [47] that: (1) the use of higher powers monotonically decreases treatment times, although a point of diminishing returns is reached after which minimal time gains are attained even with large increases in applied power (Figure 2.9); and (2) that an optimal interpulse cooling time exists (Figure 2.7), though it likely depends on many treatment parameters and this controller does not solve for the optimal cooling period.

Given our experience with this initial version of the controller, several improvements are planned to allow the adaptive model-predictive controller to further reduce treatment times and improve safety and efficacy. First, given the influential role of safety constraints in prolonging treatment time, a model of the heating and cooling of the protected voxels will be added to complement that of the treatment voxels (Eqn. 2.2). While moving the focal zone along the scan path, the controller could then predict if the next heating pulse would involve a safety violation. Using both the PV and TV models, the violation could be avoided by replacing the fixed T_{ON} safety threshold with a real-time optimization that solved for the optimal starting temperature (T_{ON_OPT}) [46]. Once the PVs cooled to T_{ON_OPT}, the next heating pulse could begin and

would complete without interruption. It may also be possible to speed up treatments by implementing a "fuzzy logic" constraint that would allow a few short-lived violations of T_{OFF}. This would eliminate the lengthy process of reheating a cell, after it had cooled, to deliver only a small amount of dose. Such a change would essentially be a combined temperature and dose safety system, with model-prediction expanded to include PV dose prediction.

Second, improved controller features, such as better treatment voxel models, could further reduce treatment times. In particular, (1) the current model assumes that a single exponential cooling period follows each heating pulse, a conservative approach that does not account for the complex temperature profiles that occur due to SAR overlap while treating future cells. Extension of the current TV cooling model to include more specific future events, something that is imminently feasible when the scan path is known, could reduce heating times. (2) If the heating rate is high enough so that a heating model cannot be identified before a cell is fully treated (see the Materials and Methods section), the AMPC cannot take full advantage of its predictive abilities and will likely over-heat the treatment cell. A better heating model approach is needed for these faster heating rates. For example, data-mining of large collections of treatment data combined with machine learning algorithms could yield better initial guesses for model parameters and improve model adaptation by applying information from similar tumor locations from other treatments, or more simply, from previous cells of the current treatment. (3) As a conservative approach, the current implementation places a high emphasis on MRTI measurements over model-predicted temperatures. In particular, the controller is allowed to switch treatment cells only

once within an MRTI interval to ensure at least one temperature measurement is acquired while treating each cell. In some cases this can introduce unnecessarily long heating times. Implementing the above changes would have the additional advantage of reducing the AMPC's treatment time dependence on the MRTI sampling interval (Figure 2.10), allowing for improved MRTI imaging.

Other investigators have reported ablation rates of ~3-4 cm^3/minute using multipass (volumetric) treatment strategies [12], [23], [24], values much larger than those attained in this study. The aforementioned studies obtained higher ablation rates because they performed treatments under different conditions. First, they did not predefine a target volume for ablation (as was done in this study), but instead executed a multipass treatment plan of fixed radius and evaluated the volume ablated post-treatment. Second, the multipass treatment plan implemented in those studies was executed with much higher applied power (~130 W vs 15 W in most of the current study). Third, they treated large tumors. Lastly, and perhaps most notably, those studies did not implement safety constraints of any kind.

When the AMPC'S treatment conditions are made more equal to those used in prior studies, simulations show the AMPC can reach comparable ablation rates. For example, when the AMPC system is used with the treatment plan shown in Figure 2.3a, a power of 130 W, a fast MRTI sampling interval, no safety constraints, and considering all ablated tissue, the AMPC'S resulting ablation rate was 4.9 cm^3/minute (65 s treatment time). Once the safety constraints are re-enabled (keeping the power at 130 W), treatment time increases to 44 minutes and the ablation rate decreases to 0.04 cm^3/minute. This illustrates again how protecting a critical area in close proximity to

the treatment volume can substantially prolong treatments.

In the future, an automatic mechanism for dynamically adjusting the transducer phases to ensure that the active cell receives the maximum SAR would further simplify treatments for the clinician. Finally, the AMPC presented here has been tailored to ablative FUS applications, but the concept of adaptive model-predictive control could benefit mild hyperthermia treatments. Instead of using model-prediction to anticipate nonlinear thermal dose effects, it could make it possible to approach the target temperature more quickly or with less overshoot. Additionally, real-time model adaptation could help compensate for tissue environment changes, such as blood flow, as well as make treatments more automatic by reducing the need for pretreatment controller tuning. Moreover, the slower rates of temperature change and longer heating durations encountered in hyperthermia treatments make it easier to dynamically derive and adapt a model (reduced need for fast MRTI). Lastly, model-prediction may also benefit hyperthermia treatments by allowing for increased MRTI field-of-view or improved resolution

2.5 Conclusion

The simulations and *in vivo* results show that adaptive model-predictive control can automatically deliver safe, effective MRgFUS treatments, and that activation of each of its multiple features successively reduces treatment time; path planning; 3D temperature measurements; accounting for prior dose; and model prediction. Such model-predictive control is practical for single-pass heating approaches despite their associated short heating intervals and need for rapid controller actions. The safety features of the AMPC provide clinicians with a flexible tool to safeguard healthy tissue

to any degree desired while automatically performing reliable and effective treatments in significantly reduced times. Finally, the controller's features provide extensive flexibility to the clinician: it is independent of the specified focal zone path; the safety vs speed tradeoff is customizable; and the model's parameters are identified and adapted during treatment.

2.6 Acknowledgments

The authors would like to thank Dr. Dennis Parker for his mentorship and the many fruitful conversations that helped this work.

2.7 References

[1] J. de Bever, N. Todd, A. Payne, D. A. Christensen, and R. B. Roemer, "Adaptive model-predictive controller for magnetic resonance guided focused ultrasound therapy," *Int. J. Hyperthermia*, vol. 30, no. 7, pp. 456–470, Nov. 2014.

[2] E. A. Stewart, W. M. W. Gedroyc, C. M. C. Tempany, B. J. Quade, Y. Inbar, T. Ehrenstein, A. Shushan, J. T. Hindley, R. D. Goldin, M. David, M. Sklair, and J. Rabinovici, "Focused ultrasound treatment of uterine fibroid tumors: safety and feasibility of a noninvasive thermoablative technique," *Am. J Obstet. Gynecol.*, vol. 189, no. 1, pp. 48–54, Jul. 2003.

[3] K. Hynynen, O. Pomeroy, D. N. Smith, P. E. Huber, N. J. McDannold, J. Kettenbach, J. Baum, S. Singer, and F. A. Jolesz, "MR imaging-guided focused ultrasound surgery of fibroadenomas in the breast: a feasibility study," *Radiology*, vol. 219, no. 1, pp. 176–185, Apr. 2001.

[4] L. G. Merckel, L. W. Bartels, M. O. Köhler, H. J. G. D. van den Bongard, R. Deckers, W. P. T. M. Mali, C. A. Binkert, C. T. Moonen, K. G. A. Gilhuijs, and M. A. A. J. van den Bosch, "MR-guided high-intensity focused ultrasound ablation of breast cancer with a dedicated breast platform," *Cardiovasc. Intervent. Radiol.*, vol. 36, no. 2, pp. 292–301, Apr. 2013.

[5] H. Furusawa, K. Namba, S. Thomsen, F. Akiyama, A. Bendet, C. Tanaka, Y. Yasuda, and H. Nakahara, "Magnetic resonance-guided focused ultrasound surgery of breast cancer: reliability and effectiveness," *J. Am. Coll. Surg.*, vol. 203, no. 1, pp. 54–63, Jul. 2006.

[6] N. McDannold, G. T. Clement, P. Black, F. Jolesz, and K. Hynynen, "Transcranial magnetic resonance imaging- guided focused ultrasound surgery of brain tumors: initial findings in 3 patients," *Neurosurgery*, vol. 66, no. 2, pp. 323–332; discussion 332, Feb. 2010.

[7] A. Okada, T. Murakami, K. Mikami, H. Onishi, N. Tanigawa, T. Marukawa, and H. Nakamura, "A case of hepatocellular carcinoma treated by MR-guided focused ultrasound ablation with respiratory gating," *Magn. Reson. Med. Sci.*, vol. 5, no. 3, pp. 167–171, Oct. 2006.

[8] W. M. Gedroyc, "New clinical applications of magnetic resonance-guided focused ultrasound," *Top. Magn. Reson. Imaging*, vol. 17, no. 3, pp. 189–194, Jun. 2006.

[9] S. Thüroff, C. Chaussy, G. Vallancien, W. Wieland, H. J. Kiel, A. Le Duc, F. Desgrandchamps, J. J. M. C. H. De La Rosette, and A. Gelet, "High-intensity focused ultrasound and localized prostate cancer: efficacy results from the European multicentric study," *J. Endourol.*, vol. 17, no. 8, pp. 673–677, Oct. 2003.

[10] W. J. Elias, D. Huss, T. Voss, J. Loomba, M. Khaled, E. Zadicario, R. C. Frysinger, S. A. Sperling, S. Wylie, S. J. Monteith, J. Druzgal, B. B. Shah, M. Harrison, and M. Wintermark, "A pilot study of focused ultrasound thalamotomy for essential tremor," *N. Engl. J. Med.*, vol. 369, no. 7, pp. 640–648, Aug. 2013.

[11] J. Hindley, W. M. Gedroyc, L. Regan, E. Stewart, C. Tempany, K. Hynyen, N. Mcdannold, Y. Inbar, Y. Itzchak, J. Rabinovici, H. S. Kim, J.-F. Geschwind, G. Hesley, B. Gostout, T. Ehrenstein, S. Hengst, M. Sklair-Levy, A. Shushan, and F. Jolesz, "MRI guidance of focused ultrasound therapy of uterine fibroids: early results," *Am. J. Roentgenol.*, vol. 183, no. 6, pp. 1713–1719, Dec. 2004.

[12] Y. Kim, D.-S. Bae, B.-G. Kim, J.-W. Lee, and T.-J. Kim, "A faster nonsurgical solution very large fibroid tumors yielded to a new ablation strategy," *Am. J. Obstet. Gynecol.*, vol. 205, no. 3, pp. 292.e1–5, Sep. 2011.

[13] N. J. McDannold, F. A. Jolesz, and K. H. Hynynen, "Determination of the optimal delay between sonications during focused ultrasound surgery in rabbits by using MR imaging to monitor thermal buildup in vivo," *Radiology*, vol. 211, no. 2, pp. 419–426, May 1999.

[14] X. Fan and K. Hynynen, "Ultrasound surgery using multiple sonications--treatment time considerations," *Ultrasound Med. Biol.*, vol. 22, no. 4, pp. 471–482, 1996.

[15] C. Damianou and K. Hynynen, "Focal spacing and near-field heating during pulsed high temperature ultrasound therapy," *Ultrasound Med. Biol.*, vol. 19, no.

9, pp. 777–787, 1993.

[16] P. VanBaren and E. S. Ebbini, "Multipoint temperature control during hyperthermia treatments: theory and simulation," *IEEE Trans. Biomed. Eng.*, vol. 42, no. 8, pp. 818–827, Aug. 1995.

[17] E. Hutchinson, M. Dahleh, and K. Hynynen, "The feasibility of MRI feedback control for intracavitary phased array hyperthermia treatments," *Int. J. Hyperthermia*, vol. 14, no. 1, pp. 39–56, Feb. 1998.

[18] M. Mattingly, R. B. Roemer, and S. Devasia, "Exact temperature tracking for hyperthermia: a model-based approach," *IEEE Trans. Control Syst. Technol.*, vol. 8, no. 6, pp. 979–992, Nov. 2000.

[19] N. B. Smith, N. K. Merrilees, M. Dahleh, and K. Hynynen, "Control system for an MRI compatible intracavitary ultrasound array for thermal treatment of prostate disease," *Int. J. Hyperthermia*, vol. 17, no. 3, pp. 271–282, Jun. 2001.

[20] R. Salomir, J. Palussière, F. C. Vimeux, J. A. de Zwart, B. Quesson, M. Gauchet, P. Lelong, J. Pergrale, N. Grenier, and C. T. Moonen, "Local hyperthermia with MR-guided focused ultrasound: spiral trajectory of the focal point optimized for temperature uniformity in the target region," *J. Magn. Reson. Imaging*, vol. 12, no. 4, pp. 571–583, Oct. 2000.

[21] J. Palussière, R. Salomir, B. Le Bail, R. Fawaz, B. Quesson, N. Grenier, and C. T. W. Moonen, "Feasibility of MR-guided focused ultrasound with real-time temperature mapping and continuous sonication for ablation of VX2 carcinoma in rabbit thigh," *Magn. Reson. Med.*, vol. 49, no. 1, pp. 89–98, Jan. 2003.

[22] C. Mougenot, R. Salomir, J. Palussière, N. Grenier, and C. T. W. Moonen, "Automatic spatial and temporal temperature control for MR-guided focused ultrasound using fast 3D MR thermometry and multispiral trajectory of the focal point," *Magn. Reson. Med.*, vol. 52, no. 5, pp. 1005–1015, 2004.

[23] M. O. Köhler, C. Mougenot, B. Quesson, J. Enholm, B. Le Bail, C. Laurent, C. T. W. Moonen, and G. J. Ehnholm, "Volumetric HIFU ablation under 3D guidance of rapid MRI thermometry," *Med. Phys.*, vol. 36, no. 8, pp. 3521–3535, Aug. 2009.

[24] J. K. Enholm, M. O. Köhler, B. Quesson, C. Mougenot, C. T. W. Moonen, and S. D. Sokka, "Improved volumetric MR-HIFU ablation by robust binary feedback control," *Biomed. Eng. IEEE Trans. On*, vol. 57, no. 1, pp. 103–113, 2010.

[25] D. L. Deardorff and C. J. Diederich, "Axial control of thermal coagulation using a multi-element interstitial ultrasound applicator with internal cooling," *IEEE Trans. Ultrason. Ferroelectr. Freq. Control*, vol. 47, no. 1, pp. 170–178, 2000.

[26] C. J. Diederich, W. H. Nau, A. Kinsey, T. Ross, J. Wootton, T. Juang, K. Butts-Pauly, V. Rieke, J. Chen, D. M. Bouley, and G. Sommer, "Catheter-based ultrasound devices and MR thermal monitoring for conformal prostate thermal therapy," *Conf. Proc. IEEE Eng. Med. Biol. Soc.*, vol. 2008, pp. 3664–3668, 2008.

[27] A. M. Kinsey, C. J. Diederich, V. Rieke, W. H. Nau, K. B. Pauly, D. Bouley, and G. Sommer, "Transurethral ultrasound applicators with dynamic multi-sector control for prostate thermal therapy: in vivo evaluation under MR guidance," *Med. Phys.*, vol. 35, no. 5, pp. 2081–2093, May 2008.

[28] D. Arora, M. A. Minor, M. Skliar, and R. B. Roemer, "Control of thermal therapies with moving power deposition field," *Phys. Med. Biol.*, vol. 51, no. 5, pp. 1201–1219, Mar. 2006.

[29] A. Payne, U. Vyas, N. Todd, J. de Bever, D. A. Christensen, and D. L. Parker, "The effect of electronically steering a phased array ultrasound transducer on near-field tissue heating," *Med. Phys.*, vol. 38, no. 9, pp. 4971–4981, Sep. 2011.

[30] N. Ellens, A. Pulkkinen, J. Song, and K. Hynynen, "The utility of sparse 2D fully electronically steerable focused ultrasound phased arrays for thermal surgery: a simulation study," *Phys. Med. Biol.*, vol. 56, no. 15, pp. 4913–4932, Aug. 2011.

[31] K. Hynynen and D. DeYoung, "Temperature elevation at muscle-bone interface during scanned, focused ultrasound hyperthermia," *Int. J. Hyperthermia*, vol. 4, no. 3, pp. 267–279, Jun. 1988.

[32] F. J. Fry, "Transkull transmission of an intense focused ultrasonic beam," *Ultrasound Med. Biol.*, vol. 3, no. 2–3, pp. 179–184, 1977.

[33] N. Todd, U. Vyas, J. de Bever, A. Payne, and D. L. Parker, "Reconstruction of fully three-dimensional high spatial and temporal resolution MR temperature maps for retrospective applications," *Magn. Reson. Med.*, vol. 67, no. 3, pp. 724–730, Mar. 2012.

[34] N. Todd, J. Prakash, H. Odéen, J. de Bever, A. Payne, P. Yalavarthy, and D. L. Parker, "Toward real-time availability of 3D temperature maps created with temporally constrained reconstruction," *Magn. Reson. Med.*, vol. 71, no. 4, pp. 1394–1404, Apr. 2014.

[35] S. A. Sapareto and W. C. Dewey, "Thermal dose determination in cancer therapy," *Int. J. Radiat. Oncol.*, vol. 10, no. 6, pp. 787–800, Apr. 1984.

[36] N. J. McDannold, R. L. King, F. A. Jolesz, and K. H. Hynynen, "Usefulness of MR imaging-derived thermometry and dosimetry in determining the threshold for tissue damage induced by thermal surgery in rabbits," *Radiology*, vol. 216,

no. 2, pp. 517–523, Aug. 2000.

[37] N. McDannold, K. Hynynen, D. Wolf, G. Wolf, and F. Jolesz, "MRI evaluation of thermal ablation of tumors with focused ultrasound," *J Magn. Reson. Imaging JMRI*, vol. 8, no. 1, pp. 91–100, Feb. 1998.

[38] C. Damianou and K. Hynynen, "The effect of various physical parameters on the size and shape of necrosed tissue volume during ultrasound surgery," *J. Acoust. Soc. Am.*, vol. 95, no. 3, pp. 1641–1649, Mar. 1994.

[39] A. H. Chung, F. A. Jolesz, and K. Hynynen, "Thermal dosimetry of a focused ultrasound beam in vivo by magnetic resonance imaging," *Med. Phys.*, vol. 26, no. 9, pp. 2017–2026, Sep. 1999.

[40] M. W. Dewhirst, B. L. Viglianti, M. Lora-Michiels, M. Hanson, and P. J. Hoopes, "Basic principles of thermal dosimetry and thermal thresholds for tissue damage from hyperthermia.," *Int. J. Hyperthermia*, vol. 19, no. 3, p. 267, Jun. 2003.

[41] U. Vyas and D. Christensen, "Ultrasound beam simulations in inhomogeneous tissue geometries using the hybrid angular spectrum method," *IEEE Trans. Ultrason. Ferroelectr. Freq. Control*, vol. 59, no. 6, pp. 1093–1100, Jun. 2012.

[42] H. H. Pennes, "Analysis of tissue and arterial blood temperatures in the resting human forearm," *J. Appl. Physiol.*, vol. 1, no. 2, pp. 93–122, Aug. 1948.

[43] F. A. Duck, *Physical Properties of Tissue: A Comprehensive Reference Book*. London; San Diego: Academic Press, 1990.

[44] D. A. Christensen, *Ultrasonic Bioinstrumentation*. New York: Wiley, 1988.

[45] N. Todd, U. Vyas, J. de Bever, A. Payne, and D. L. Parker, "The effects of spatial sampling choices on MR temperature measurements," *Magn. Reson. Med.*, vol. 65, no. 2, pp. 515–521, Feb. 2011.

[46] A. Payne, U. Vyas, A. Blankespoor, D. Christensen, and R. Roemer, "Minimisation of HIFU pulse heating and interpulse cooling times," *Int. J Hyperthermia*, vol. 26, no. 2, pp. 198–208, Jan. 2010.

[47] J. Coon, N. Todd, and R. Roemer, "HIFU treatment time reduction through heating approach optimisation," *Int. J Hyperthermia*, vol. 28, no. 8, pp. 799–820, Nov. 2012.

CHAPTER 3

THREE-DIMENSIONAL MR ACOUSTIC RADIATION FORCE IMAGING

3.1 Introduction

Magnetic resonance-guided focused ultrasound (MRgFUS) is a promising noninvasive technology with wide ranging applications for the treatment of cancer [1]–[3], localized drug-delivery [4]–[6], neuromodulation applications [7], [8], and blood-brain barrier opening [9]–[11]. One critical aspect of successfully using MRgFUS for any application is accurate positioning of the ultrasound focal spot as well as ensuring high quality focusing when the beam propagates through an aberrating tissue environment. Aberrations caused, for example, by tissue inhomogeneity in the breast [12], [13] or by tissue-bone [14] interfaces could cause inadvertent damage to nontargeted tissues.

One clinically implemented approach to minimizing the risk of inadvertent damage to nontargeted tissue is to perform low-power interrogation pulses while measuring the resulting temperature distribution via MR proton resonance frequency (PRF) shift thermometry. Since the location and magnitude of the temperature rise is not known in advance, and many interrogation pulses may be required during a single treatment, unintended tissue damage may occur. Furthermore, the standard PRF

thermometry method is ineffective in fat, which would be especially problematic for therapies in organs such as the breast. Previous work has shown that the tissue displacement caused by focused ultrasound can be measured using MR acoustic radiation force imaging (ARFI), and that this technique can be used to localize the focal spot in 2D [15]–[17]. Since these MR-ARFI techniques use short ultrasound bursts on the order of 1-20 ms with low duty cycles (1-10%), minimal tissue heating is induced, making 2D MR-ARFI a safe alternative to low power interrogation pulses. Additionally, MR-ARFI generates displacement maps via motion encoding gradients (MEG) that produce a phase difference proportional to the tissue's displacement; as a result, MR-ARFI is not susceptible to the same issues as PRF thermometry and can measure displacement in any tissue type, including fat.

Several methods for performing MR-ARFI have been presented using both spin-echo and gradient echo sequences, and several MEG schemes have been used including: (1) repeated unipolar [16], [18]; (2) bipolar gradients [17], [19], [20] (often repeated on both sides of the refocusing RF pulse in spin-echo sequences); (3) alternating bipolar gradients [21]; and (4) tripolar gradients [22]. In addition to beam localization, variations of these encoding schemes have been used to apply MR-ARFI for phase aberration correction [22]–[25], and tissue property determination [16], [19], but has been done with 2D imaging only. While 2D imaging has proved to be fast, the low displacements being measured (on the order of micrometers) sometimes required many averages to improve SNR. When used for beam localization, there is the risk that the peak energy deposition does not occur in the imaging plane because the user must place the measurement plane before the location of the focus is known.

Furthermore, significant energy may be deposited outside the 2D field-of-view (FoV), which will not be captured but may impact beam quality. Measuring the displacement field over a large FoV in 3D would simplify and improve the accuracy of beam localization as well as improve knowledge of how intervening tissues affect beam quality. For the purpose of phase aberration correction, it is also possible that the increased information content provided by a 3D displacement field would improve the resulting focus or reduce the number of scans required to perform the optimization process. Also, 3D acquisition schemes have inherent signal averaging which improves SNR compared to a single 2D acquisition.

This chapter presents a method for performing 3D MR-ARFI with special attention paid to reducing imaging time and maintaining safe levels of tissue heating (< 6 °C). Several unique features are presented including: (1) an unbalanced bipolar motion encoding gradient waveform that allows for lower echo-times and higher echo train lengths (ETL); (2) a configurable k_z reduction factor (KZRF) that reduces the number of US pulses required by firing only during the acquisition of a central subset of the k_z partitions; and (3) pulse repetition time (TR)-level interleaving of the US-ON and US-OFF images which can either reduce the effective duty cycle by half (reducing tissue heating) or reduce the total imaging time by half (keeping duty cycle constant). This work also presents a parametric study of the tradeoffs among sequence parameters that influence imaging time and tissue heating including duty cycle (DC), TR, ETL, and KZRF.

3.2 Methods

3.2.1 Sequence Overview

A 3D spin-echo segmented EPI pulse sequence was modified to include an unbalanced bipolar MEG and optional flyback readout (Figure 3.1a). The area of MEG lobe A1 and crusher gradient lobe A2 is specified by the user, and the area of the second MEG lobe is set to A1 + A2 to ensure that the 0^{th} order gradient moment sums to zero. The second MEG lobe effectively combines the crusher gradient of a standard spin-echo sequence (required to suppress stimulated echoes between successive TRs due to imperfect refocusing pulses) and the required gradient moment for motion encoding. An optical trigger output from the MRI pulse sequence synchronizes the firing of an ultrasound burst with the second lobe of the MEG. This optical trigger is converted to an electrical pulse compatible with the ultrasound device with custom made electronics designed and manufactured by the first author. The 3D spin-echo unbalanced bipolar ARFI sequence presented here has two additional features that enhance safety. First, the KZRF reduces the number of ultrasound pulses delivered by firing only while acquiring a central subset of all k_z partitions. Second, instead of sequentially acquiring all k-space lines for a volume with ultrasound ON followed by the acquisition of all k-space lines with ultrasound OFF, acquisition of an US-ON image can be interleaved with an US-OFF image at the TR level. Thus, the same line of k-space will be read twice in consecutive TRs: once with an ultrasound burst and once with no ultrasound. This reduces the ultrasound duty cycle by a factor of two while keeping total scan time constant, or conversely the imaging time can be halved while holding the duty cycle constant.

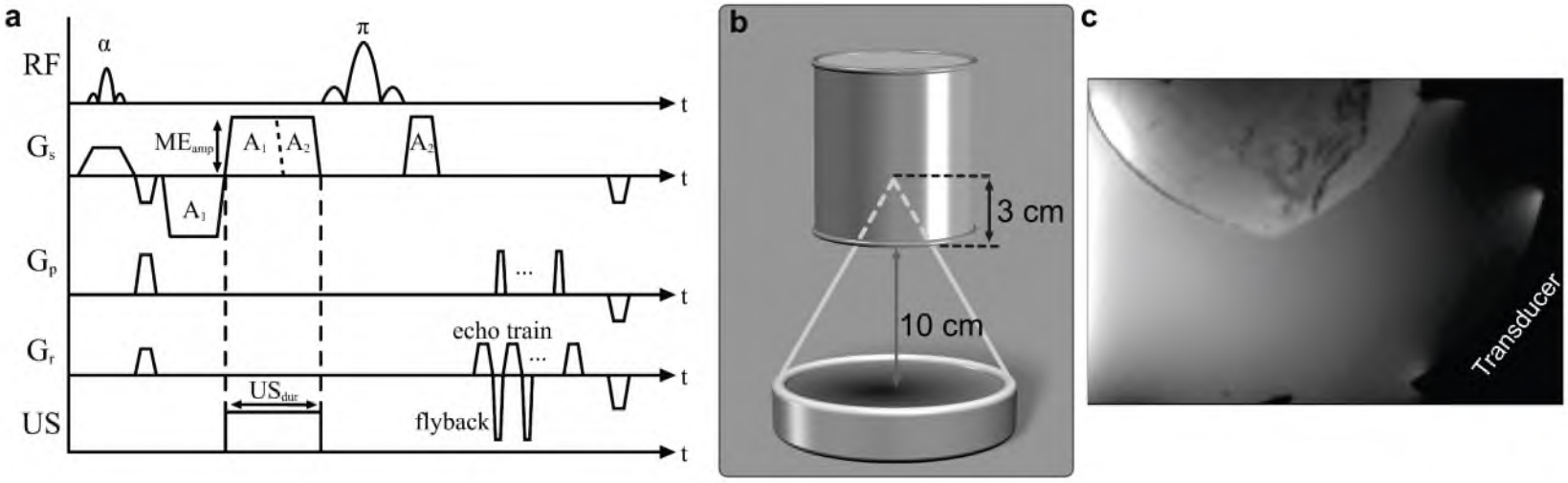

Figure 3.1: Overview of the experiment configurations. **(a)** Pulse sequence diagram for unbalanced-bipolar spin-echo ARFI sequence. **(b)** Phantom experiment setup. Phased array transducer approximately 10 cm below gelatin phantom. Geometric focus penetrates approximately 3 cm into the phantom. **(c)** Ex vivo cadaver breast used with breast specific MRgHIFU system consisting of phased array transducer and integrated 11-chanel RF coil.

3.2.2 Comparison of 3D ARFI and 3D PRF Thermometry

A study in a tissue-mimicking phantom was performed to evaluate the ability of 3D ARFI to predict the position of peak temperature rise, and also to compare the characteristics of the 3D displacement pattern measured by MR-ARFI to the 3D temperature pattern measured by standard PRF thermometry. A gelatin phantom was constructed in-house from powder (Vyse Gelatin Co., Schiller Park, IL, USA) and positioned approximately 10 cm (Figure 3.1b) above a 256-element phased-array transducer (Imasonic, Besançon, France) operating at 1 MHz (focal distance of 13 cm, aperture diameter of 14.5 cm, full-width-at-half-maximum 2 x 2 x 8 mm, f-number = 0.90). The transducer was driven by electronics and software by Image Guided Therapy (Pessac, France). A deionized and degassed water bath coupled the phantom to the transducer. The water bath was degassed using a custom built degassing system, and a Hanna Instruments HI-9146 (Woonsocket, Rhode Island, USA) dissolved oxygen meter confirmed that the dissolved oxygen content was reduced to $\leq$ 1.0 ppm. A single loop radio-frequency (RF) receive-only coil was positioned around the phantom approximately 3 cm from the bottom of the phantom. The 3D ARFI maps were acquired with a Siemens 3T Tim Trio MRI scanner (Erlangen, Germany) over a 192 x 108 x 48 mm volume at 1.2 x 1.2 x 2.0 mm resolution. The raw k-space data were Tukey filtered along k_z (using Matlab's (Mathworks Inc, Natick, MA) *tukeywin* function with R = 0.85) to suppress Gibbs ringing artifact, and then zero-fill-interpolated to 0.2 x 0.2 x 0.5 mm voxel spacing to mitigate partial volume effects. Complex phase subtraction between the US-ON and US-OFF images was performed to produce phase difference maps, which were converted to displacement using the

following equation that assumes constant tissue displacement over the encoding interval:

$$\Delta D = \frac{\Delta\phi}{2\pi\gamma \int_0^{t_{enc}} G_{MEG}(\mathrm{t})\delta t} \tag{3.1}$$

where γ is the gyromagnetic ratio of hydrogen in MHz/T, G_{MEG} is the trapezoidal motion encoding gradient amplitude in mT/m, and $\Delta\phi$ is the phase difference measured.

Unless otherwise noted, the following scan parameters were used: TR = 200 ms, echo time (TE) = 45 ms, ETL = 9, bandwidth = 744 Hz/px, flyback readout, flip angle = 90°, ME_{amp} = 30 mT/m, MEG_{A1} = 259 mT·m^{-1}·ms, MEG_{A2} = 25 mT·m^{-1}·ms, acquisition time = 56 s, US power = 55 W, US_{dur} = 10 ms. Holding the ultrasound power constant, 3D ARFI maps were acquired while electronically steering the focal spot to four locations (US_x, US_y, US_z): (0, 0, 0) mm, (6, 0, 0) mm, (12, 0, 0) mm, and (0, 0, 8) mm. These displacement maps were acquired with KZRF = 0.64 (US on during 18 of 28 k_z partitions). ARFI displacement maps were also acquired at geometric focus with the TR-interleaving feature enabled such that the effective duty cycle was reduced to 2.5% with KZRF remaining 0.64. For comparison, a fully sampled ARFI dataset was acquired with US on during all k_z partitions (KZRF = 1.0) and with no filtering along k_z.

A second set of experiments were performed to investigate whether 3D ARFI could predict the location of peak heating as measured by PRF thermometry. Temperature maps of continuous-wave heating (8.8 W applied for 27.72 s) were

acquired using a 3D segmented EPI PRF thermometry sequence with flyback readout. Temperature was measured over the same volume, at the same resolution, with equivalent k_z filtering, and at the same four electronically steered focal spot locations as the 3D ARFI maps. All scan parameters were equal to the 3D ARFI scan parameters except: TR = 33 ms, TE = 15 ms, FA = 20°, and acquisition time = 9.24 s. The 3D ARFI and 3D temperature datasets were compared and the error between the position of peak ARFI displacement and location of peak temperature change was quantified.

3.2.3 Ex Vivo Cadaver Breast

After tests in phantoms, an experiment in a cadaver breast was performed to evaluate the sequence's effectiveness at measuring 3D displacement fields in a realistic inhomogeneous tissue environment. The breast was secured to a plastic plate and positioned on top a breast specific MRgFUS system [26] with integrated 11-channel RF coil and 940 kHz 256-channel phased array transducer (Imasonic, Besançon, France). 3D ARFI maps were acquired in ME2 mode over a 256 x 196 x 36 mm volume at 2 x 2 x 3 mm resolution. Other sequence parameters include: TR = 250 ms, TE = 53 ms, ETL = 7, bandwidth = 751 Hz/px, flyback readout, flip angle = 90°, ME_{amp} = 28 mT/m, MEG_{A1} = 305 $mT \cdot m^{-1} \cdot ms$, MEG_{A2} = 25 $mT \cdot m^{-1} \cdot ms$, acquisition time = 49 s, US power = 44 W, US_{dur} = 10 ms.

3.2.4 Parametric Safety Study of 3D MR-ARFI

Three-dimensional imaging requires more phase encoding steps than 2D imaging, and while the primary penalty of this is increased imaging time, for 3D MR-

ARFI this also increases tissue heating due to the increased number of US pulses delivered. To safely perform MR-ARFI, the induced temperature rise should be limited to 6 °C, both to avoid the accumulation of thermal dose [27] and to satisfy FDA limits on Thermal Index [28]. To this end, an evaluation of the tradeoffs among sequence parameters affecting tissue heating was performed. This study considered the field-of-view and resolution used to acquire the experimental 3D ARFI maps in the previous section. Parameters studied that affect tissue heating included: ETL, KZRF, TR / DC, and TR-Interleaving (see Sequence Overview). Echo-planar imaging helps achieve practical imaging times and reduces the number of US pulses required to attain a 3D MR-ARFI map. However, ETLs can increase ghosting artifacts and increase TE, both of which diminish image quality and SNR. Using this sequence's k_z reduction factor feature, the number of US pulses can be reduced without changing the ETL by setting KZRF < 1. This reduces the spatial resolution of the displacement maps along the k_z direction (while maintaining full resolution of the anatomical images), however these high frequency components may not be necessary to resolve the ARFI peak since the broadest dimension of the beam is also along k_z. The number of US pulses, N_{US}, required for a given ETL and KZRF is given by:

$$N_{US} = \frac{N_y N_z}{ETL} \times KZRF \tag{3.2}$$

where N_y and N_z are the number of 3D phase encoding steps required for a given field-of-view and resolution. For the fixed FoV and resolution studied, $N_y = 90$ and $N_z = 28$. The number of US pulses required for a single US-ON 3D MR-ARFI map was

computed using Eqn. (3.2) with ETL ranging from 1 to 15 and for three KZRFs: [1.00, 0.64, 0.50].

To rule out impractically long sequence configurations (>60 s per measurement), the imaging time to acquire a single measurement of a 3D MR-ARFI sequence was computed using:

$$tAcq = \frac{N_y N_z}{ETL} \times TR \tag{3.3}$$

A set of heating experiments were performed in the gelatin phantom to quantify the temperature increase induced by the ultrasound pulses of varying duty cycles. During acquisition of the US-ON image, Eqn. (3.4) relates the TR interval, the US-pulse duration (US_{dur}) and duty cycle (DC) when the TR-interleaving feature is disabled.

$$DC = \frac{US_{dur}}{TR} \times 100 \tag{3.4}$$

For these experiments, the ultrasound power and pulse duration were held constant (55 W and 10 ms, respectively) while TR was varied to adjust the duty cycle. The following TRs (duty cycles) were tested: 100 ms (10% DC), 200 ms (5% DC), 400 ms (2.5% DC). Temperature rise was measured with a standard 3D PRF thermometry sequence with similar parameters to those described previously, but with a reduced FoV to improve the temporal resolution (4.16 s instead of 9.24 s). For each DC tested, the maximum temperature of each time frame was computed, and a double

exponential curve was fit to these temperature data via least-squared error minimization. These curves were used to evaluate how much heating occurred for a given number of US pulses at each duty cycle.

3.3 Results

3.3.1 Comparison of 3D MR-ARFI with 3D PRF Thermometry

A representative 3D displacement pattern measured by the SE unbalanced-bipolar MR-ARFI sequence while firing at the geometric focus is shown in Figure 3.2. Slices through the displacement maps measured when electronically steering the US beam from (0, 0, 0) to (6, 0, 0), (12, 0, 0) and (0, 0, 8) mm are shown in Figure 3.3a-d, with slices longitudinal to the beam through the point of maximum displacement. For comparison, the 3D PRF thermometry maps are shown in Figure 3.3e-h. The drop in maximum displacement and temperature rise as well as a measurement of the actual beam deflection as the US beam was steered electronically from geometric focus is illustrated in Figure 3.4. Maximum displacement fell from 32 μm at geometric focus

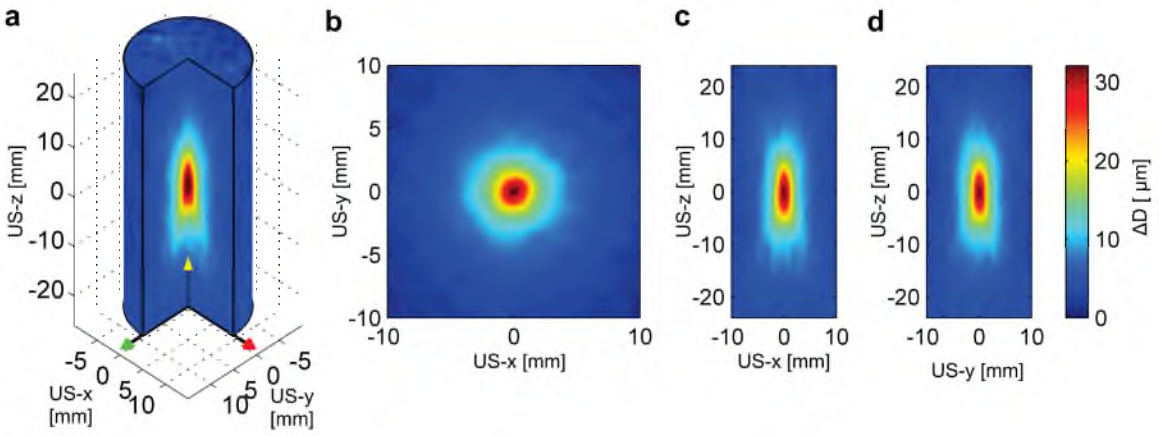

Figure 3.2: 3D ARFI volume measured at geometric focus. **(a)** Cut away view of 3D displacement map, **(b)** slice transverse to US beam through maximum displacement, **(c-d)** slices longitudinal to US beam through maximum displacement.

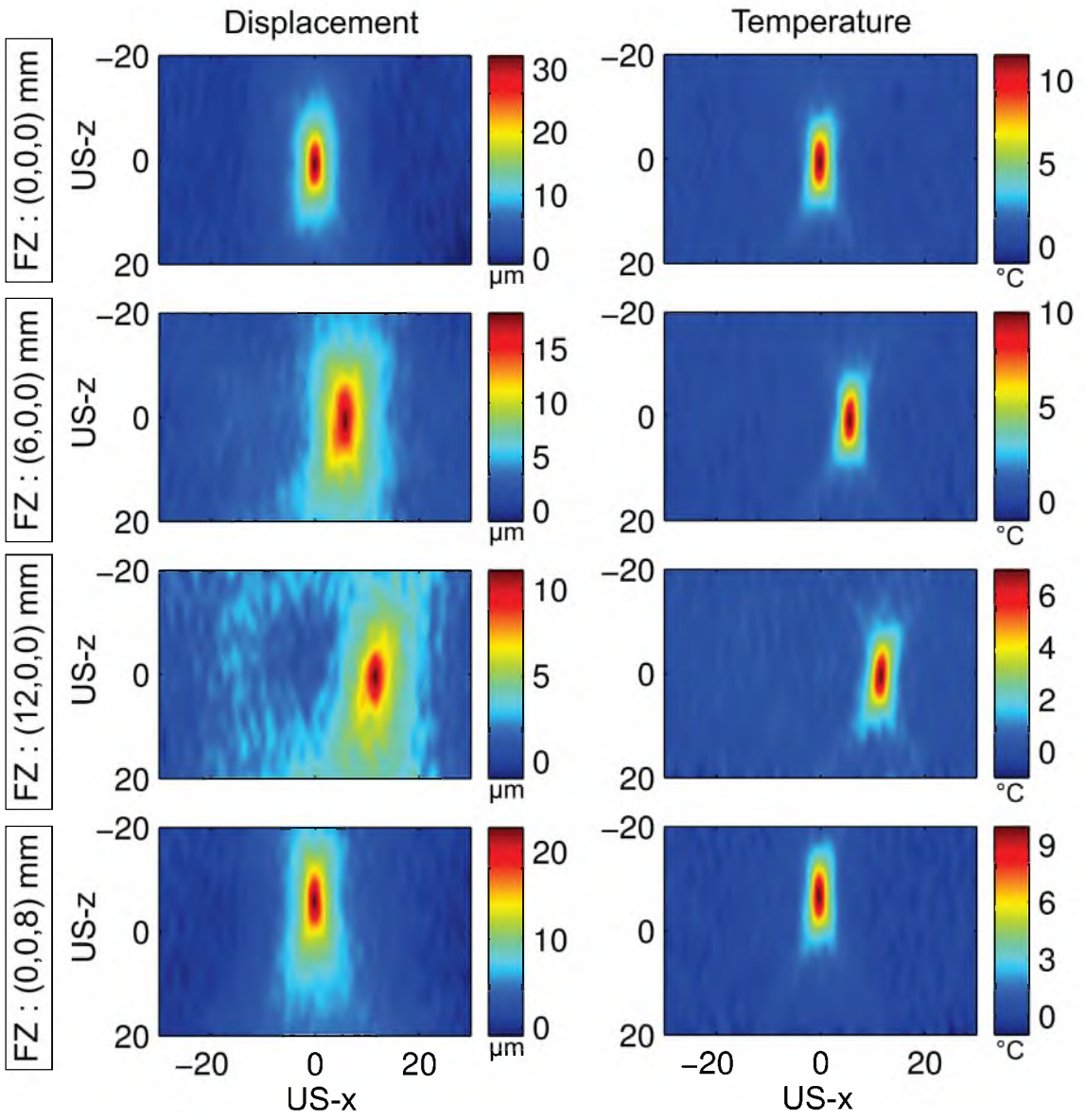

Figure 3.3: Comparison of 3D ARFI and 3D temperature patterns while electronically steering to multiple positions. Slices are longitudinal to US beam propagation and cut through maximum displacement/temperature. While the 3D ARFI patterns are generally broader than the 3D temperature patterns, a clear peak exists and matches the location of the temperature peak within 0.4 mm in the transverse direction and 1.0 mm in the longitudinal direction. The 3D ARFI maps captured the expected beam tilting and decreased displacement associated with electronic steering in addition to the near-field effects.

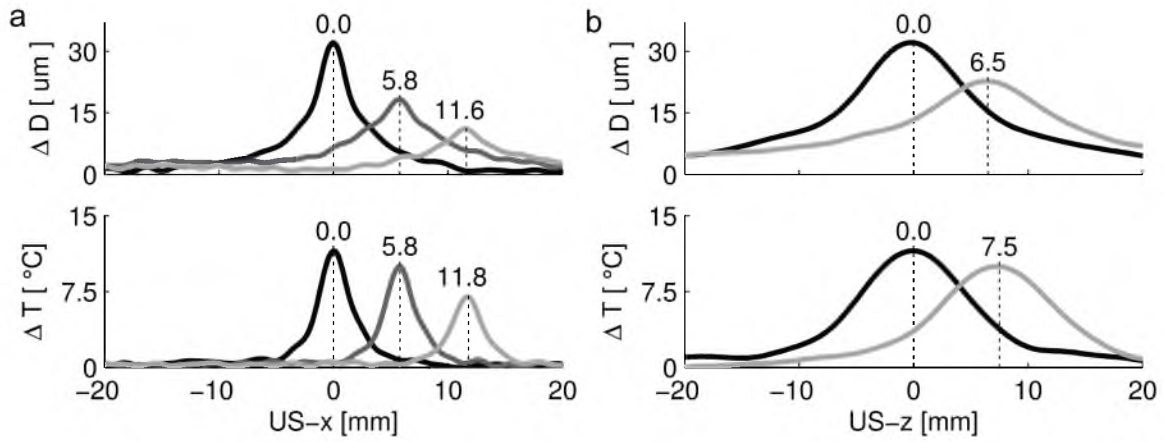

Figure 3.4: Comparison of temperature and ARFI profiles when electronically steering the US beam. **(a)** Profiles along transverse line through maximum displacement (top) and maximum temperature (bottom) as beam is electronically steered to from (0, 0, 0) mm (black) to (6, 0, 0) mm, (medium gray) and (12, 0, 0) mm (light gray). Numbers above lines indicate measured beam deflection. **(b)** Profiles along longitudinal line through maximum displacement (top) and temperature (bottom) as beam is steered from (0,0,0) mm (black) to (0, 0, 8) mm (light gray).

to 18 μm when the beam was steered to (6, 0, 0) mm (a 44% reduction), and to 11 μm at (12, 0, 0) mm (a 65% reduction), despite the output power being held constant. The movement of the peak displacement tracked the prescribed beam deflection within 0.4 mm when steering in the US-x direction (perpendicular to the US beam), and was within 1.5 mm when steering in the US-z direction (along the US beam). Evaluating the same quantities using the 3D temperature maps, at geometric focus the maximum temperature measured was 11.5 °C which was reduced to 10.0 °C when steering the beam to (6,0,0) mm (a 13% reduction), and to 7 °C at (12,0,0) mm (a 39 % reduction). The error between the location of peak temperature rise and the desired beam deflection distance was within 0.2 mm when steering in the US-x direction and within 0.5 mm when steering in the US-z direction.

3.3.2 Ex vivo Cadaver Breast

Slices through the 3D displacement volume measured in ex vivo cadaver breast are shown in Figure 3.5. Because of the high fat content of the breast, it was not possible to measure temperature using the PRF thermometry method, however, the fat content did not impact the ability to measure ARFI displacement.

3.3.3 Parametric Study of Heating due to 3D MR-ARFI

Figure 3.6 summarizes the critical sequence parameters and their effects on tissue heating. Figure 3.6a illustrates the imaging time required for several TR and ETL combinations. For a given combination of ETL and TR, it is possible to look up the corresponding number of US pulses required in Figure 3.6b for various k_z reduction factors. For example, with ETL = 9, TR = 200 ms, and KZRF = 1.0, Figure 3.6a shows that tAcq = 56 s while Figure 3.6b indicates 280 US pulses would be required. According to Figure 3.6c, which shows the tissue heating as a function of the number of US pulses for each duty cycle, acquiring a 3D ARFI map with this configuration would result in a 6.2 °C temperature rise which violates the 6 °C safety limit. However, by reducing KZRF to 0.64 (such that only 18 of the 28 k_z partitions are acquired with US on), the number of US pulses decreases to 180 and induced tissue heating is reduced to 5.6 °C. The TR2-interleaving mode can either reduce the effective duty cycle by half (to 2.5%), which in this case would limit the induced temperature rise to 3.1 °C, or double imaging speed by reducing TR by 50% (duty cycle remains 5.0%). In this mode (TR = 100 ms, KZRF = 0.64, and ETL = 9), imaging time would be only 28 s vs 56 s without TR-interleaving, while maintaining a safe tissue temperature.

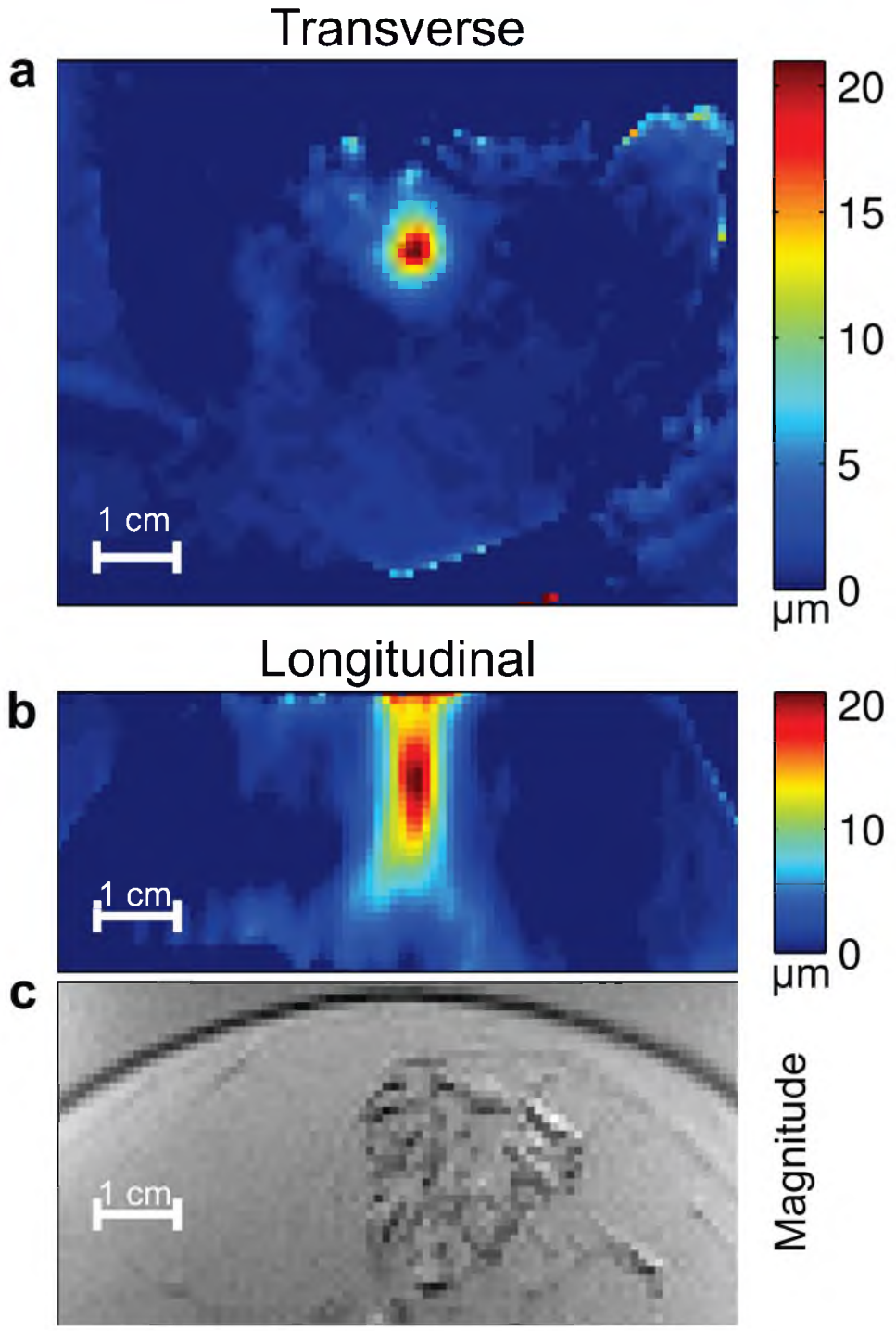

Figure 3.5: 3D displacement maps in cadaver breast. **(a)** Slice transverse to US beam. **(b)** Slice longitudinal to US beam. **(c)** Magnitude image at approximate location shown in (b).

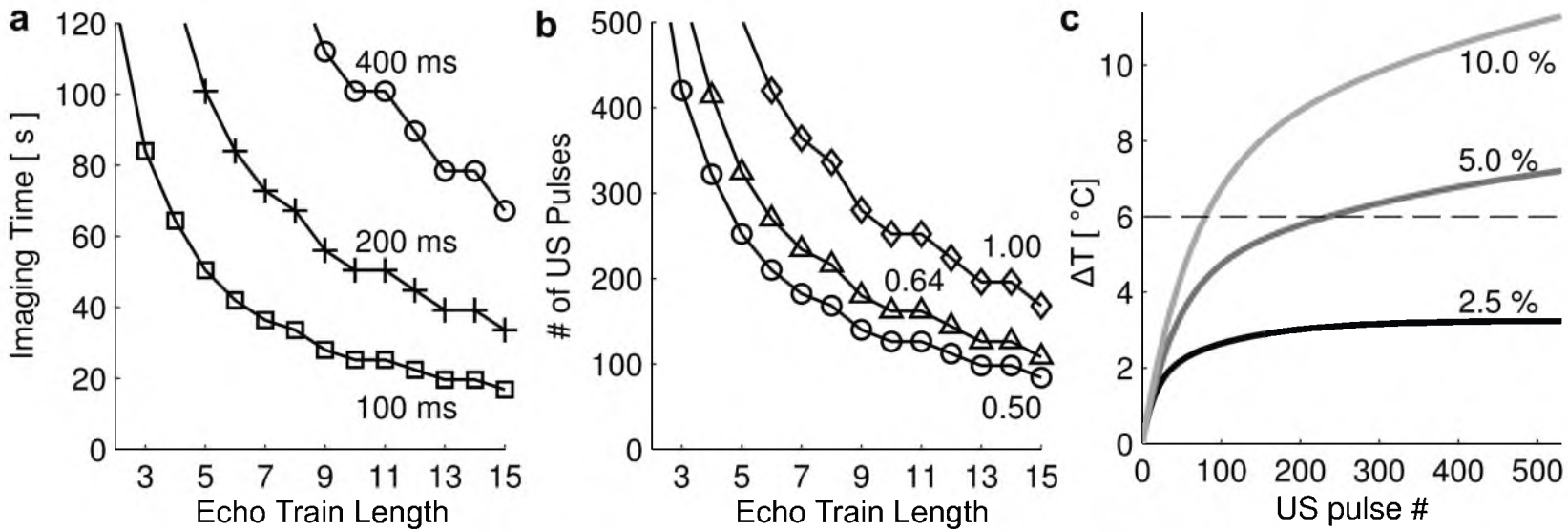

Figure 3.6: Effect of ARFI imaging parameters on resulting tissue heating. **(a)** Imaging time, calculated from Eqn. (3.3), as a function of ETL for TR = 400, 200, and 100 ms. **(b)** Number of ultrasound pulses delivered (Eqn. (3.2)) as a function of ETL and KZRF = 1.0 (Full sampling), 0.64, and 0.5. **(c)** Tissue heating as a function of number of US pulses for duty cycle = 10.0%, 5.0%, and 2.5%. Curves are the result of double-exponential fits to experimentally measured tissue heating data with the ultrasound pulse duration kept constant at 10 ms. The dashed line indicates the 6 °C safety limit on induced tissue heating.

The displacement profiles for the fully sampled mode (KZRF = 1.0, no filtering in k_z), partial sampled mode (KZRF = 0.64, tukey filter in k_z) and TR2 interleaved mode (KZRF = 0.64, tukey filter in k_z) are shown in Figure 3.7. The location of peak displacement agree in US-x/y for all three modes, while the TR2 interleaved mode differs along the US-z direction by 0.5 mm. The magnitude of maximum displacement measured by the full and partial modes agree within approximately 10%, while the TR2 interleaved mode shows significantly less displacement, albeit a clear peak exists that is suitable for focal spot localization. Neither the reduction of KZRF from 1.0 to 0.64, nor the filtering performed along k_z diminished the displacement profile's quality appreciably.

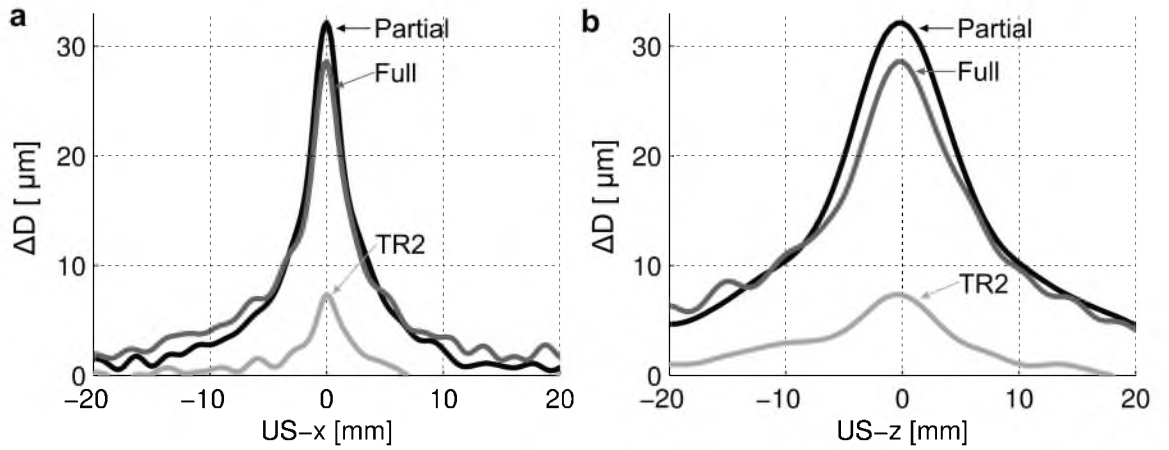

Figure 3.7: Comparison of displacement profiles measured by different acquisition schemes. **(a)** Displacement profiles along the US-x direction, **(b)** displacement profiles along the US-z direction. [Full] has US on during all k_z partitions (KZRF = 1.0) and no k-space filtering, [partial] has US on during 18/28 k_z partitions (KZRF = 0.64) and filtering along k_z, and [TR2] has TR interleave mode enabled with KZRF = 0.64 and k_z filtering. In all schemes the locations of the peaks agree within 0.5 mm, but partial and TR2 reduce the induced temperature rise to 5.6 °C and 3.0 °C, respectively, from 6.2 C in the full case.

3.4 Discussion

The choice of motion encoding gradient (MEG) proved to be beneficial in reducing imaging time and tissue heating. Other common motion encoding strategies employ two bipolar gradients pulses on either side of the 180° pulse (for SE sequences), single bipolar pulses with alternating polarity (for GRE sequences), or tripolar pulses. The double bipolar approach increases the TE or limits the ETL that can be used, which increases imaging time in a 3D acquisition and increases tissue heating due to repeated application of US bursts. A single bipolar approach helps reduce TE, but if alternating polarity gradient encoding is used, such that there is no US-OFF image, then the number of US pulses is doubled which would increase tissue heating. Tripolar gradients have the benefit of producing more self-canceling eddy currents, but increase the risk that the tissue is still displaced during the 3rd gradient moment thus incorrectly subtracting motion encoding phase. The unbalanced bipolar MEG gains time efficiency by combining the motion encoding and crusher gradient moments allowing the US to be on for a maximum amount of time. Since there is only one MEG (before the 180° pulse), motion encoding does not compete for time with the EPI readout after the 180° pulse, allowing for shorter TEs and larger ETLs.

The results in Figure 3.3 and Figure 3.4 demonstrate that 3D ARFI maps can localize the focal spot in all three dimensions in a single scan and that peak displacement is a good predictor of the location of peak temperature rise. This could be important in applications such as FUS treatments of breast where PRF temperature imaging may not be able to measure the temperature due to fat content of the tissue, or in brain treatments where performing a test heating to localize the focal spot may

cause unwanted tissue heating. The errors between the location of peak temperature and displacement were within one measure voxel (before zero-filling). After zero-filling, the maximum difference in location of peak displacement vs temperature was 0.4 mm transverse to the US beam and 1.0 mm along the US beam. While it does not improve the fundamental resolution of the image, zero-filling helps reduce errors introduced by partial volume effects and thus can improve the localization of the focal spot, especially in the case of ARFI where the profile has a sharp peak along the beam's transverse direction. Since the PRF thermometry sequence is based on a GRE pulse sequence while the unbalanced-bipolar ARFI sequence is based on a SE sequence, the temperature imaging is susceptible to additional distortion (caused by, for example, static field inhomogeneities), which may not affect the SE ARFI sequences. The ARFI sequence also benefits from a longer TR and higher flip angle which may increase the available signal. However, these benefits are offset by the ARFI sequence's relatively long TE (45 ms vs 15 ms) and the additional vibration and eddy currents caused by the strong motion encoding gradients.

The cadaver breast sample was highly inhomogeneous and contained a significant amount of fat which made it impossible to measure temperature with the PRF method. However, 3D displacement fields were successfully measured (Figure 3.5), and the 21.3 μm peak displacement measured is similar in magnitude to the tissue mimicking phantom tests. This demonstrates the usefulness of 3D ARFI to fully localize the focal position regardless of tissue type, and in a scenario where standard test heating approaches would be unsuccessful.

At the power tested, the induced temperature rise for a 2.5% duty cycle reached

steady state of 3.5 °C, and thus imaging for long durations could be performed safely without violating the 6.0 °C safety threshold (Figure 3.6). However, at the 5.0% and 10% duty cycles it becomes important to consider the number of US shots delivered, as the 6 °C threshold is violated after 236 and 80 shots, respectively. Using Figure 3.6 to guide the selection of imaging parameters for the imaging volume tested, ETLs of ≤ 5 are impractical either because the imaging time is too long (> 60 s) or because the number of US shots required results in significant tissue heating. On the other hand, as the ETL is increased there are diminishing returns in regard to imaging time and tissue heating. Higher ETLs can also increase ghosting artifacts as well as TE, which degrades SNR, and so ETLs in the range of 7-11 strike a balance between image quality, imaging time, and safety.

Adjusting the KZRF from 1.0 to 0.64 mitigated tissue heating concerns by reducing the induced temperature rise from 6.2 °C to 5.6 °C. While this also reduces the effective resolution of the 3D ARFI maps along the US-z direction, generally focused ultrasound transducers have an ellipsoid shaped focal zone with one dimension being elongated and this reduces the spatial resolution requirements along that dimension. The datasets shown in Figure 3.2–Figure 3.5 were acquired with KZRF = 0.64, but in Figure 3.7 it can be seen that the displacement profile shape and location of peak displacement did not differ appreciably when full sampling was used (KZRF = 1.0) and filtering was disabled. This indicates that the high frequency components did not contribute significantly to the localization of the focal spot and thus acquiring them with US on superfluously heats the tissue. Furthermore, the higher k_z spatial frequencies were acquired (albeit without US), so the magnitude

images needed for correlation of the MR-ARFI maps with patient anatomy would retain their full prescribed resolution.

Further reductions in tissue heating were achieved by enabling the TR-interleaving feature, which was used to halve the effective duty cycle. For comparison, sequential acquisition of the US-ON and US-OFF images using an US-pulse duration of 10ms, a TR of 200ms (5% DC), and KZRF = 1.0 resulted in a 6.2 °C temperature rise. By activating TR-interleaving and setting KZRF = 0.64, the TR remained 200 ms but the effective DC was reduced to 2.5% because the US fires every other TR. Consequently, the maximum tissue heating was lowered by 50% to only 3.1 °C. Alternatively, the TR-interleaving mode could have maintained the 5.0% DC and halved total imaging time by reducing the TR to 100 ms without causing unsafe tissue heating. Without TR interleaving, a TR of 100 ms (10% DC) would cause unsafe heating for any choice of ETL or KZRF studied since the safety threshold is violated after 80 US shots and even an ETL of 15 with KZRF = 0.5 requires 84 shots. However, by interleaving the acquisition of the US-ON and US-OFF images every TR, the imaging speed of TR = 100 ms is available with the tissue safety of the TR = 200 ms case.

The location of peak displacement measured by each imaging mode (full sampling, partial sampling, and TR-interleaved) agreed except for the US-z location in the TR2 mode which differed by 0.5 mm. More significantly, however, was that the TR2 mode measured a lower peak displacement of 7.4 μm vs 28.6 um for the fully sampled case. To investigate this result, an additional test was performed where three measurements were acquired in [OFF]-[ON]-[OFF] order, but where only the first two

were interleaved and the third was acquired without interleaving. The phase of each measurement before subtraction, shown in Figure 3.8a, reveals that the first measurement has a phase profile akin to that of the second, US-ON, measurement despite it lacking US pulses. This is not seen in the third measurement, which also lacked US pulses but whose acquisition was not interleaved with an US-ON measurement. This indicates that signal pathways exist which allow stimulated echoes to contaminate the phase of the first US-OFF measurement, and thus reduce the measured displacement. When the third, US-OFF and un-interleaved, measurement is used as the reference phase, the measured displacement increases to 19.1 μm which

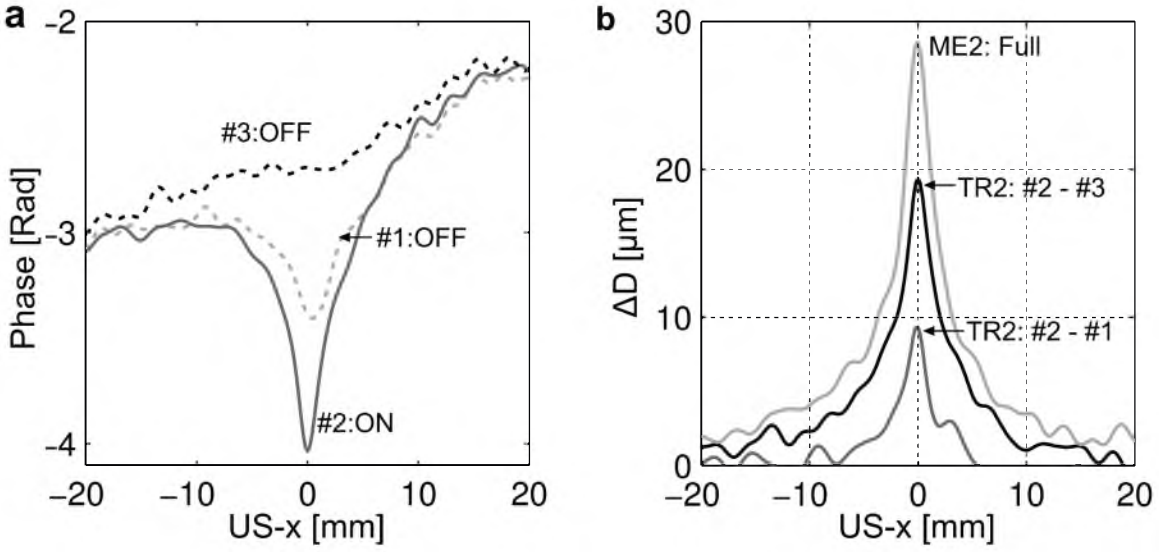

Figure 3.8: Fully sampled mode compared to TR-interleaved mode. **(a)** Phase for three TR2 measurements before subtraction. The first (OFF) and second (ON) measurements were interleaved while all k-space lines for the third (OFF) measurement were acquired sequentially without interleaving. Though #1 and #3 both lack US pulses, a phase bump exists in #1 that mimics that of #2 (which had US pulses). This indicates that stimulated echoes are distorting the phase measurement of #1, which artificially reduces the displacement measured by TR2 mode (Figure 3.7). **(b)** Displacement measured by ME2 mode computed to TR2 mode when #1 vs #3 is used as the reference phase. Eliminating the phase offset seen in #1 by using #3 as the reference phase increases the measured displacement.

agrees more closely to the displacement measured by ME2 mode (Figure 3.8b). Stimulated echoes may play a role in exaggerating the phase induced during ME2 mode which could account for the remaining difference between ME2 and TR2. Future investigations and sequence improvements could disrupt the offending signal pathways and improve signal fidelity in both modes.

As a final note on safety, these measurements represent a worst-case scenario as the phantom is not perfused, and the US power used in both the phantom and breast studies generated tissue displacements that were larger than required for focal spot localization. Safety concerns under *in vivo* conditions should be allayed both by tissue perfusion, which accelerates tissue cooling, and reduced power. Using the study of sequence parameters and features to guide the selection of imaging parameters, 3D MR-ARFI maps can be safely acquired in a time efficient manner over a large field-of-view.

As with all 3D acquisition schemes, this sequence is sensitive to motion, both of the imaging subject, and peripheral objects (such as the coupling water bath) that may generate susceptibility changes in the imaging volume. It may be possible to reduce these side effects by adding a phase navigator to perform correction during image reconstruction. Nevertheless, this 3D ARFI technique could be beneficial for applications such as breast imaging and brain imaging where there is little organ motion, or the motion can be constrained.

In the future, it may be possible to further reduce the tissue heating and acquisition by integrating existing k-space undersampling techniques [29], [30] into this 3D ARFI sequence. Additional investigation into the use of 3D MR-ARFI for the

purpose of phase aberration correction would also be beneficial, as the 3D displacement field provides significantly more information with which to perform correction.

3.5 Conclusion

A 3D spin-echo pulse sequence employing a novel unbalanced bipolar motion encoding gradient was presented and successfully tested in phantoms and ex vivo breast tissue. This sequence can safely measure displacement due to acoustic radiation force over a large FoV and at high resolution in reasonable scan times (< 60 s per scan). Comparisons to 3D PRF temperature imaging showed that the 3D ARFI sequence accurately localized the ultrasound focal spot using a single scan. The ability to cover a large FoV increases the likelihood that the peak displacement is captured, and that any near-field effects, such as reflections of bone interfaces, are observed before potentially harmful heating is attempted. The ability of 3D ARFI to localize the focal spot, even in a cadaver breast containing fat, proved that 3D ARFI is a useful alternative to standard low-power heating methods, which failed in this scenario. The tradeoffs among imaging parameters and tissue heating were explored in a parametric study of TR, ETL, and duty cycle. It was found that ETLs in the range of 7-11 strike a good balance between improving imaging time, reducing tissue heating, and managing image artifacts. Advanced sequence features such as k_z reduction factor, where the US is enabled only during a subset of all k_z partitions, and TR-interleaving, where the acquisition of US-ON and US-OFF images alternate every TR, were tested and shown to reduce tissue heating by up to 50% without affecting the accuracy of beam localization.

3.6 Acknowledgments

The authors gratefully acknowledge the input and guidance of Dr. Allison Payne.

3.7 References

[1] H. Furusawa, K. Namba, S. Thomsen, F. Akiyama, A. Bendet, C. Tanaka, Y. Yasuda, and H. Nakahara, "Magnetic resonance-guided focused ultrasound surgery of breast cancer: reliability and effectiveness," *J. Am. Coll. Surg.*, vol. 203, no. 1, pp. 54–63, Jul. 2006.

[2] G. Sommer, D. Bouley, H. Gill, B. Daniel, K. B. Pauly, and C. Diederich, "Focal ablation of prostate cancer: four roles for magnetic resonance imaging guidance," *Can. J. Urol.*, vol. 20, no. 2, pp. 6672–6681, Apr. 2013.

[3] Y. Kim, D.-S. Bae, B.-G. Kim, J.-W. Lee, and T.-J. Kim, "A faster nonsurgical solution very large fibroid tumors yielded to a new ablation strategy," *Am. J. Obstet. Gynecol.*, vol. 205, no. 3, pp. 292.e1–5, Sep. 2011.

[4] B. Kneidl, M. Peller, G. Winter, L. H. Lindner, and M. Hossann, "Thermosensitive liposomal drug delivery systems: state of the art review," *Int. J. Nanomedicine*, vol. 9, pp. 4387–4398, 2014.

[5] N. Rapoport, K.-H. Nam, R. Gupta, Z. Gao, P. Mohan, A. Payne, N. Todd, X. Liu, T. Kim, J. Shea, C. Scaife, D. L. Parker, E.-K. Jeong, and A. M. Kennedy, "Ultrasound-mediated tumor imaging and nanotherapy using drug loaded, block copolymer stabilized perfluorocarbon nanoemulsions," *J. Controlled Release*, vol. 153, no. 1, pp. 4–15, Jul. 2011.

[6] V. Frenkel, A. Etherington, M. Greene, J. Quijano, J. Xie, F. Hunter, S. Dromi, and K. C. P. Li, "Delivery of liposomal doxorubicin (Doxil) in a breast cancer tumor model: investigation of potential enhancement by pulsed-high intensity focused ultrasound exposure," *Acad. Radiol.*, vol. 13, no. 4, pp. 469–479, Apr. 2006.

[7] W. J. Elias, D. Huss, T. Voss, J. Loomba, M. Khaled, E. Zadicario, R. C. Frysinger, S. A. Sperling, S. Wylie, S. J. Monteith, J. Druzgal, B. B. Shah, M. Harrison, and M. Wintermark, "A pilot study of focused ultrasound thalamotomy for essential tremor," *N. Engl. J. Med.*, vol. 369, no. 7, pp. 640–648, Aug. 2013.

[8] G. Suffredini and L. M. Levy, "MR-guided focused ultrasound: applications to essential tremor and other neurologic conditions," *Am. J. Neuroradiol.*, Nov.

2013.

[9] N. McDannold, C. D. Arvanitis, N. Vykhodtseva, and M. S. Livingstone, "Temporary disruption of the blood-brain barrier by use of ultrasound and microbubbles: safety and efficacy evaluation in rhesus macaques," *Cancer Res.*, vol. 72, no. 14, pp. 3652–3663, Jul. 2012.

[10] M. A. O'Reilly and K. Hynynen, "Ultrasound enhanced drug delivery to the brain and central nervous system," *Int. J. Hyperth. Off. J. Eur. Soc. Hyperthermic Oncol. North Am. Hyperth. Group*, vol. 28, no. 4, pp. 386–396, 2012.

[11] K. Hynynen, N. McDannold, N. Vykhodtseva, S. Raymond, R. Weissleder, F. A. Jolesz, and N. Sheikov, "Focal disruption of the blood-brain barrier due to 260-kHz ultrasound bursts: a method for molecular imaging and targeted drug delivery," *J. Neurosurg.*, vol. 105, no. 3, pp. 445–454, Sep. 2006.

[12] C. Mougenot, M. Tillander, J. Koskela, M. O. Köhler, C. Moonen, and M. Ries, "High intensity focused ultrasound with large aperture transducers: a MRI based focal point correction for tissue heterogeneity," *Med. Phys.*, vol. 39, no. 4, pp. 1936–1945, Apr. 2012.

[13] P. D. Freiburger, D. C. Sullivan, B. H. LeBlanc, S. W. Smith, and G. E. Trahey, "Two dimensional ultrasonic beam distortion in the breast: in vivo measurements and effects," *Ultrason. Imaging*, vol. 14, no. 4, pp. 398–414, Oct. 1992.

[14] K. Hynynen and D. DeYoung, "Temperature elevation at muscle-bone interface during scanned, focused ultrasound hyperthermia," *Int. J. Hyperthermia*, vol. 4, no. 3, pp. 267–279, Jun. 1988.

[15] E. A. Kaye, J. Chen, and K. B. Pauly, "Rapid MR-ARFI method for focal spot localization during focused ultrasound therapy," *Magn. Reson. Med.*, vol. 65, pp. 738–743, Mar. 2011.

[16] N. McDannold and S. E. Maier, "Magnetic resonance acoustic radiation force imaging," *Med. Phys.*, vol. 35, no. 8, pp. 3748–3758, Aug. 2008.

[17] A. Holbrook, "In vivo MR acoustic radiation force imaging in the porcine liver," *Med. Phys.*, vol. 38, no. 9, pp. 5081–9, 2011.

[18] E. A. Kaye and K. B. Pauly, "Adapting MRI acoustic radiation force imaging for in vivo human brain focused ultrasound applications," *Magn. Reson. Med.*, vol. 69, no. 3, pp. 724–733, Mar. 2013.

[19] R. Souchon, R. Salomir, O. Beuf, L. Milot, D. Grenier, D. Lyonnet, J.-Y. Chapelon, and O. Rouvière, "Transient MR elastography (t-MRE) using ultrasound radiation force: theory, safety, and initial experiments in vitro," *Magn. Reson. Med.*, vol. 60, no. 4, pp. 871–881, Oct. 2008.

[20] J. Chen, R. Watkins, and K. B. Pauly, "Optimization of encoding gradients for MR-ARFI," *Magn. Reson. Med.*, vol. 63, pp. 1050–1058, Apr. 2010.

[21] V. Auboiroux, M. Viallon, J. Roland, J.-N. Hyacinthe, L. Petrusca, D. R. Morel, T. Goget, S. Terraz, P. Gross, C. D. Becker, and R. Salomir, "ARFI-prepared MRgHIFU in liver: simultaneous mapping of ARFI-displacement and temperature elevation, using a fast GRE-EPI sequence," *Magn. Reson. Med.*, vol. 68, no. 3, pp. 932–946, Sep. 2012.

[22] Y. Hertzberg, A. Volovick, Y. Zur, Y. Medan, S. Vitek, and G. Navon, "Ultrasound focusing using magnetic resonance acoustic radiation force imaging: application to ultrasound transcranial therapy," *Med. Phys.*, vol. 37, no. 6, pp. 2934–2942, Jun. 2010.

[23] A. Kyriakou, E. Neufeld, B. Werner, M. M. Paulides, G. Szekely, and N. Kuster, "A review of numerical and experimental compensation techniques for skull-induced phase aberrations in transcranial focused ultrasound," *Int. J. Hyperthermia*, vol. 30, no. 1, pp. 36–46, Feb. 2014.

[24] L. Marsac, D. Chauvet, B. Larrat, M. Pernot, B. Robert, M. Fink, A. L. Boch, J. F. Aubry, and M. Tanter, "MR-guided adaptive focusing of therapeutic ultrasound beams in the human head," *Med. Phys.*, vol. 39, no. 2, pp. 1141–1149, Feb. 2012.

[25] U. Vyas, E. Kaye, and K. B. Pauly, "Transcranial phase aberration correction using beam simulations and MR-ARFI," *Med. Phys.*, vol. 41, no. 3, p. 032901, Mar. 2014.

[26] A. Payne, R. Merrill, E. Minalga, U. Vyas, J. de Bever, N. Todd, R. Hadley, E. Dumont, L. Neumayer, D. Christensen, R. Roemer, and D. Parker, "Design and characterization of a laterally mounted phased-array transducer breast-specific MRgHIFU device with integrated 11-channel receiver array," *Med. Phys.*, vol. 39, no. 3, pp. 1552–1560, Mar. 2012.

[27] S. A. Sapareto and W. C. Dewey, "Thermal dose determination in cancer therapy," *Int. J. Radiat. Oncol.*, vol. 10, no. 6, pp. 787–800, Apr. 1984.

[28] "Guidance for industry and FDA staff - information for manufacturers seeking marketing clearance of diagnostic ultrasound systems and transducers," U.S. Department of Health and Human Services, Food and Drug Administration; Radiological Devices Branch, Office of Device Evaluation; Division of Solid and Fluid Mechanics, Office of Science and Engineering Laboratories, Washington, DC, Report #560, 2008.

[29] N. Todd, J. Prakash, H. Odéen, J. de Bever, A. Payne, P. Yalavarthy, and D. L. Parker, "Toward real-time availability of 3D temperature maps created with temporally constrained reconstruction," *Magn. Reson. Med.*, vol. 71, no. 4, pp.

1394–1404, Apr. 2014.

[30] H. Odéen, N. Todd, M. Diakite, E. Minalga, A. Payne, and D. L. Parker, "Sampling strategies for subsampled segmented EPI PRF thermometry in MR guided high intensity focused ultrasound," *Med. Phys.*, vol. 41, no. 9, p. 092301, Sep. 2014.

CHAPTER 4

SIMULTANEOUS ACQUISITION OF 3D ACOUSTIC RADIATION FORCE IMAGING AND PRF THERMOMETRY USING A MULTI-CONTRAST APPROACH

4.1 Introduction

In Chapter 3, a method for performing 3D acoustic radiation force imaging (ARFI) was presented using a spin-echo sequence. While it was found that 3D ARFI could be done safely, standalone PRF thermometry imaging was required to measure the induced temperature rise; this would be time consuming and potentially hazardous to perform after every 3D ARFI measurement. Consequently, it would be beneficial if the temperature rise induced by 3D ARFI could be monitored without additional imaging scans. This chapter presents a second 3D ARFI technique that is capable of simultaneously measuring tissue displacement and tissue heating.

The spin-echo method presented in the previous chapter is not sensitive to temperature change resulting from the proton resonance frequency shift (PRF), and so this ARFI method uses a gradient-recalled echo (GRE) pulse sequence that preserves the sensitivity to temperature change. However, once motion encoding gradients are added to the sequence, the measured phase has contributions from both tissue

displacement and tissue heating, and so a means of attributing the contribution made to the total phase change from each source is required. Other investigators have achieved this in 2D by alternating the polarity of the motion encoding gradients [1]; however, this approach has the downside of increased artifacts due to noncanceling eddy-currents and increased noise in the images [2]. This chapter presents a novel method of acquiring simultaneous temperature and displacement measurements using a multicontrast acquisition, without alternating the gradient polarity, and is also the first to do so in 3D. While multicontrast acquisitions have been used to measure other quantities, such as temperature, T1, and T2*, [3]–[6], this is the first use of a multicontrast acquisition for performing displacement measurements.

This new 3D ARFI method samples the same lines of k-space multiple times within a single TR interval, and it will be shown that this extra information can be used to solve for the constituent parts of the total phase change. This approach is particularly well suited to MR-ARFI because long TRs are usually required to prevent overheating the tissue. Thus, in most ARFI schemes, data acquisition consumes only a small fraction of the TR interval and the remaining time is wasted. This method makes more efficient use of the TR interval by filling the dead time with repeated measurements of the same k-space lines. This has two positive outcomes: (1) the signal-to-noise ratio (SNR) of the image is improved through signal averaging, and (2) the additional data make it possible to determine temperature separately from tissue displacement.

4.2 Methods

The sequence timing diagram used throughout this chapter is shown in Figure 4.1. The sequence is based on a GRE segmented echo planar imaging sequence that was modified to include a bipolar motion encoding gradient (MEG) and to allow repeated acquisitions of the readout train. Each repetition of the readout is referred to as a "contrast" and the number of contrasts allowed is limited by the TR interval. The ultrasound burst was synchronized with the second lobe of the MEG by means of an optical trigger emitted by the sequence. The device described in Appendix A was used to convert the optical trigger from the MRI to an electrical trigger compatible with the ultrasound waveform generator.

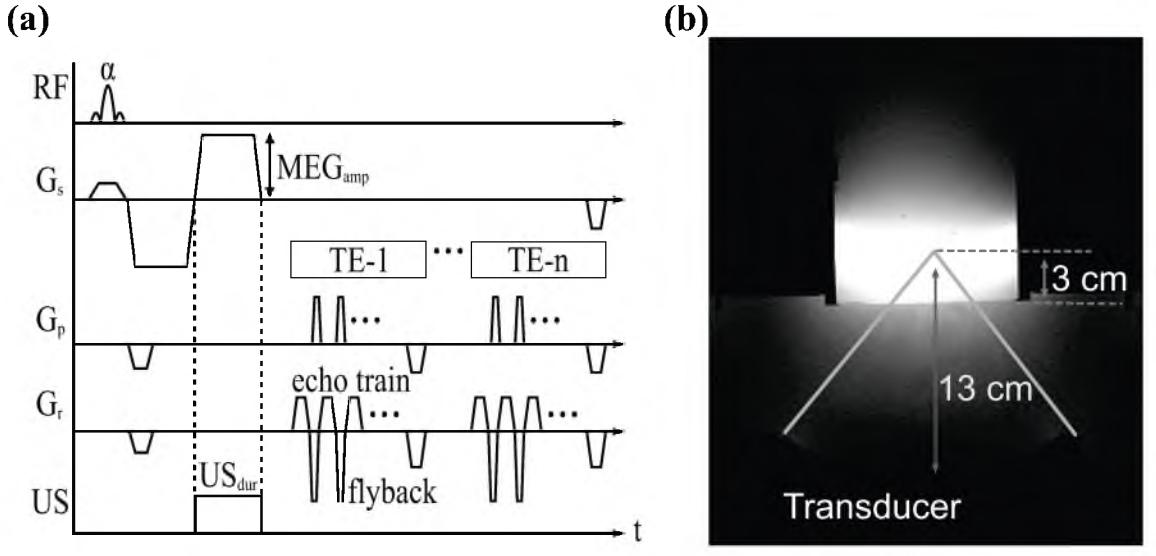

Figure 4.1: Experiment configuration summary. **(a)** GRE multicontrast ARFI pulse sequence diagram. Readout is repeated multiple times with an echo forming at TE-1, TE-2, etc. **(b)** Experiment set up with phased-array transducer positioned 13 cm below a gelatin phantom. Transducer focus penetrated 3 cm into the phantom.

4.2.1 Determination of the ARFI and Temperature Phase Contributions

Reconstruction of the multicontrast data must be done differently than in the previous chapter which performed a simple complex subtraction between a reference image with no ultrasound and a second image with ultrasound. The first step is to generate a regular complex image for each contrast for both the ultrasound-off and ultrasound-on measurements. Let the i-th contrast of the measurements with ultrasound be denoted as ON_i, and let OFF_i denote the i-th contrast of the images without ultrasound. An example of the phase for ON_1 through ON_3 is shown in Figure 4.2a-c. Since each contrast is acquired at an increasingly later echo time, the signal decreases for each successive contrast. Furthermore, the signal decays at a rate of T2*, which is faster than the spin echo technique of Chapter 3, since this sequence is based on a gradient recalled echo instead of a spin-echo acquisition. The next step is to perform a complex phase subtraction between ON_i and OFF_i for each contrast to attain a phase difference, $\Delta\phi_i$, for each contrast. At this point, it is still unknown how

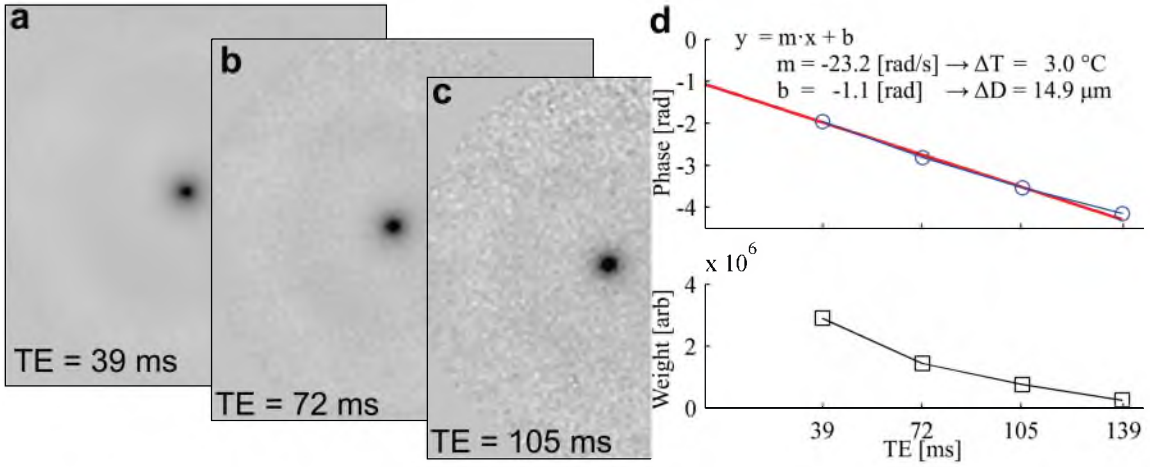

Figure 4.2: Image reconstruction for multicontrast sequence. **(a-c)** Phase maps for three contrasts demonstrating reduction in signal over time. **(d)** Example of separating displacement and temperature phase contributions by weighted fit. Slope of the line gives phase from temperature while intercept gives phase from displacement.

much of $\Delta\phi_i$ is due to temperature change vs displacement. To resolve this, it is first noted that the phase due to temperature accrues as:

$$\Delta\phi_T = \gamma B_0 \Delta T \cdot TE \tag{4.1}$$

while the phase due to displacement accrues as:

$$\Delta\phi_D = \gamma \int_0^t MEG(t)\Delta D(t)dt \tag{4.2}$$

and the total phase is then:

$$\Delta\phi_i = 2\pi\gamma B_0 \Delta T \cdot TE \; + \; \gamma \int_0^t MEG(t)\Delta D(t)dt \tag{4.3}$$

Since $\Delta\phi_D$ is not a function of TE, and it is reasonable to assume the tissue displacement is the same for every ultrasound shot, then $\Delta\phi_D$ will be a constant in the previous expression. Furthermore, if ΔT changes slowly over the period of a single TR, then the term $2\pi\gamma B_0 \Delta T$ in Eqn (4.3) is also a constant, reducing Eqn (4.3) to:

$$\Delta\phi_i = m \cdot TE \; + \; b \tag{4.4}$$

This reveals that the total phase difference evolves as a linear function of the echo time of each contrast, and that the displacement phase is the total phase at TE = 0. Intuitively, this makes sense since in the absence of tissue heating there would be a constant phase associated with a given displacement, as was the case with the SE

technique in Chapter 3. Thus, the final task is to perform a linear least-squared error fit to the $\Delta\phi_i$ vs TE of each voxel, at which point temperature can be solved for with:

$$m = \gamma B_0 \alpha \Delta T \Rightarrow \Delta T = \frac{m}{\gamma B_0 \alpha} \tag{4.5}$$

and displacement is given by:

$$b = \gamma \int_0^{t_{enc}} MEG(t)\Delta D(t)dt \Rightarrow \Delta D = \frac{b}{\gamma \int_0^t MEG(t)dt} \tag{4.6}$$

where the displacement has been reduced to a weighted time-average displacement over the encoding interval, and the integral in the denominator is the known motion encoding gradient area. Figure 4.2d demonstrates the linear fit for one voxel with corresponding conversion of slope/intercept to temperature/displacement, and where the additional step of weighting the fit by the signal magnitude has been taken to account for the decrease in SNR over time. While this process increases the reconstruction time compared to the simple subtraction reconstruction method of the spin-echo technique, each voxel is independent and the task is easily computed in parallel on a CPU or GPU. If reconstruction speed were still a constraint, reconstruction could be limited to a region of interest surrounding the focal spot.

4.2.2 Validation of Multicontrast Sequence

Experiments in a gelatin phantom compared the displacement and temperature measurements derived from the multicontrast sequence to those of the spin-echo

ARFI and standard PRF thermometry sequences, respectively. The relevant sequence parameters for each sequence are summarized in Table 4.1. All ARFI measurements used a pulse duration of 10 ms and an applied power of 44 W. The standard PRF thermometry sequence used the same ultrasound power and duty cycle as the ARFI scans (44 W, 10 ms on, 190 ms off), but had a faster acquisition time so the measurement that came closest in time to ARFI dataset was used for comparison.

A second experiment was performed to address an unsolved question regarding how well the location of peak heating and peak displacement agree along the beam's propagation direction. Previous experiments, which were not capable of simultaneous ARFI and temperature measurement, have indicated that peak displacement may occur more proximal to the transducer than peak temperature. However, this has been a difficult experiment to perform since it required using two different sequences with

Table 4.1 : Sequence parameters for each sequence type

	TR [ms]	**TE** [ms]	**Acq. Time per Meas** [s]	**FA** [°]	**ETL**	**Resolution** [mm]	**Field-of-View** [mm]	**MEG_{Mom}** [ms·mT/m]
MC ARFI	200	30, 48, 66, 83, 101, 119, 137, 154, 172	53	85	9	1 x 1 x 2.5	192 x 108 x 50	284
SE ARFI	200	45	53	90	9	1 x 1 x 2.5	192 x 108 x 50	284
PRF	35	16	11	20	9	1 x 1 x 2.5	192 x 108 x 50	N/A

FA = Flip Angle. ETL = echo train length, i.e., the number of k-space lines acquired per contrast.

different acquisition schemes. Most notably, the standalone ARFI sequence was based on a spin-echo sequence while the thermometry sequence was a GRE based sequence. Since these two ways of forming an echo have different distortion and warping characteristics, it was difficult to register the two datasets precisely. With the multicontrast sequence, no registration is required because temperature and displacement are acquired simultaneously. For these tests, the volume was rotated such that phase encode direction with 1.0 mm resolution was along the ultrasound direction, instead of the slice encoding direction with 2.5 mm resolution. All datasets were zero-fill interpolated from their acquired resolution to 0.5 x 0.5 x 0.5 mm voxel spacing to reduce partial volume effects.

4.3 Results

A comparison of the 3D displacement maps measured by the multicontrast and the spin-echo techniques are shown in Figure 4.3, while Figure 4.4 shows the 3D temperature maps measured with the multicontrast sequence compared to the standard MR thermometry sequence. The peak displacements measured by each method agree to within 0.5 μm, while peak temperatures agree to within 0.8 °C. While both metrics agree within the noise of the measurements, it should be noted that due to the differing acquisition intervals, it was not possible to acquire a standard PRF temperature map with heating duration identical to that of the multicontrast temperature maps. As a result, the standard PRF sequence had a slightly longer heating duration. When the imaging direction with highest resolution was aligned with beam's direction of propagation, the location of peak heating and peak displacement agreed to within 0.5 mm (see Figure 4.5).

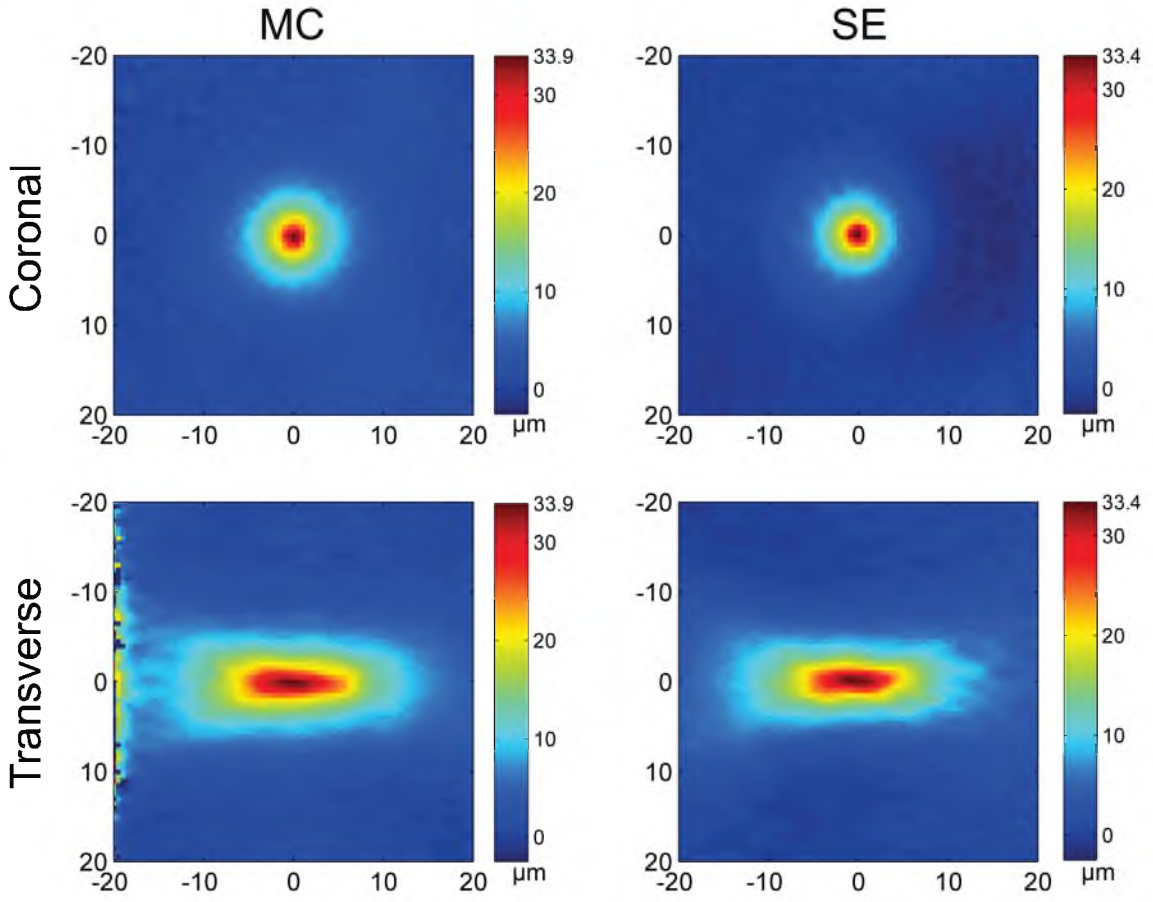

Figure 4.3: Comparison of 3D displacement maps as measured by MC-ARFI and SE-ARFI.

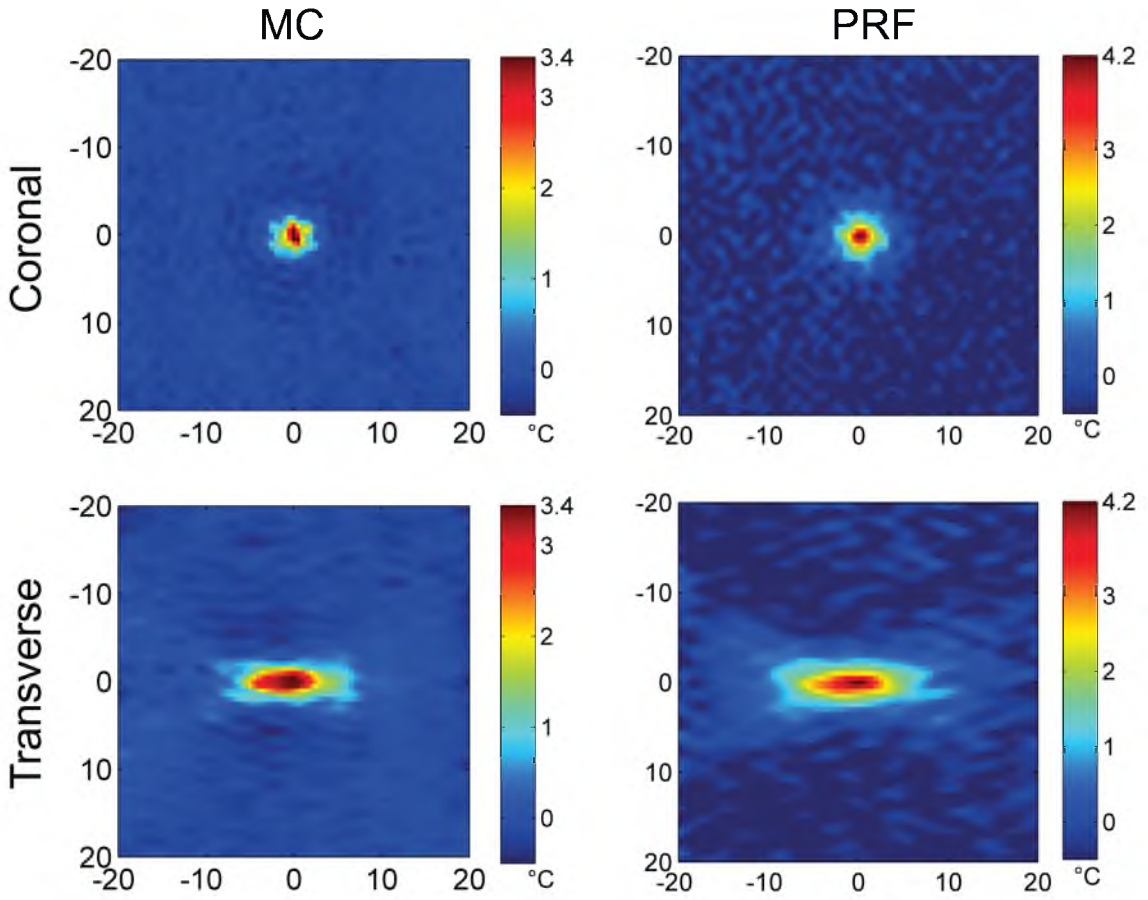

Figure 4.4: Comparison of 3D temperature maps as measured by the multicontrast approach and standard PRF thermometry. Note: duration of heating in the PRF method is slightly longer.

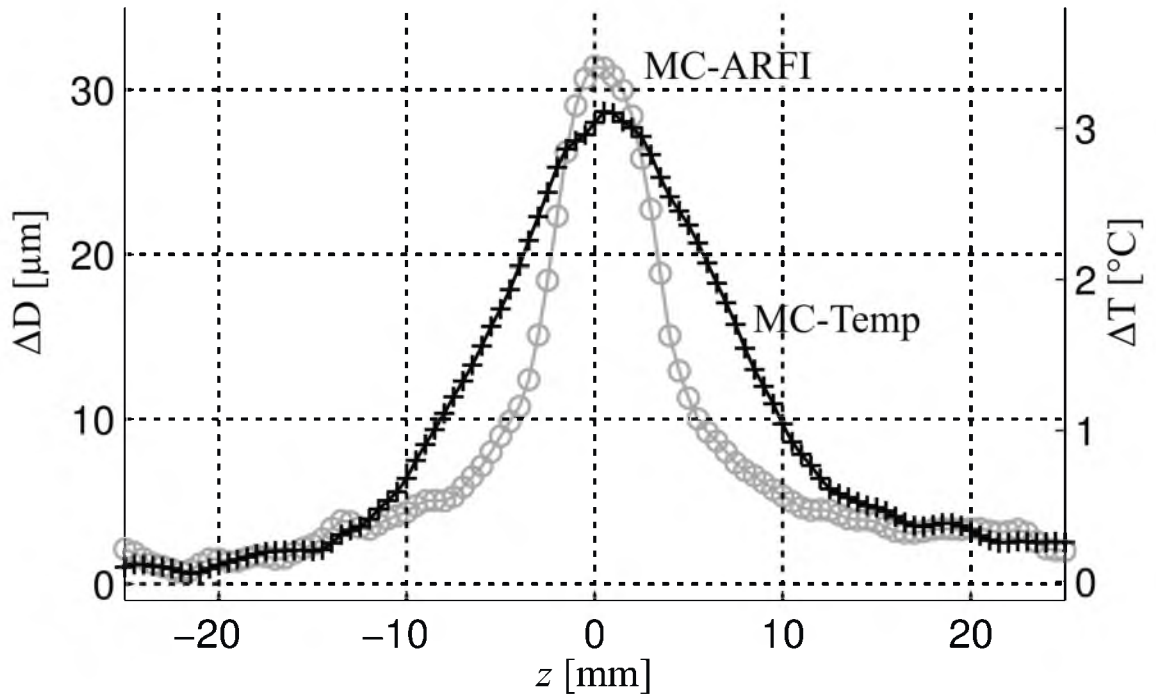

Figure 4.5: Comparison of MC-ARFI and MC-Temperature when axis of best resolution (1 mm) was aligned with beam propagation direction. Location of peak ARFI and temperature agree to within 0.5 mm.

4.4 Discussion

The displacement maps in Figure 4.3 demonstrate qualitatively that the two measurement schemes produce similar 3D displacement fields. Additionally, the agreement of peak displacement to within 0.5 μm indicates that the multicontrast approach can be relied upon as a means of ARFI measurement. The temperature maps in Figure 4.4 show signs of increased deviation between the two methods. However, the general shape of the patterns are similar, and the maximum temperatures agree within the noise of the measurements. This may be a sign that the weighting function used when performing the per-voxel linear fit to phase was not optimal, or there was simply too much signal decay by the later echoes which resulted in an improper slope calculation. Further investigation into the most appropriate and robust weighting is

warranted. In all cases, tissue heating was less than 4.5 °C which indicates this method is safe. The result in Figure 4.5 resolves an important question that has been difficult to definitively answer without simultaneous acquisition of temperature and displacement: does the location of peak ARFI displacement occur closer to the transducer than does the location of peak temperature? Figure 4.5 indicates that, at least in homogeneous media, the answer is: no, in fact they coincide quite closely. According to the new multicontrast measurement, peak ARFI displacement occurred within 0.5 mm of peak temperature, which is less than the size of a single voxel. This demonstrates a benefit of simultaneous measurements in addition to providing a safety monitoring mechanism.

Finally, for beam localization purposes, this sequence could be used without separating the effects of ARFI and temperature. Since both indicate the presence of the ultrasound beam, and there is now evidence that the two effects overlap even in the z direction; the combined sensitivity to temperature and displacement may improve the accuracy of focal spot determination. Of course the temperature and displacement effects could be separated at any time, but this "combined" phase could provide a useful third signal.

In future, this multicontrast technique could be applied to the determination of tissue mechanical properties and their temperature dependence. By continuously measuring ARFI and temperature, it may be possible to observe a mechanical change in the tissue experimentally, and have a record of the temperature history that generated that change. This may help provide another means of measuring tumor destruction which would further complement the earlier work of this dissertation.

4.5 Conclusion

This chapter has presented and validated a new method of safely measuring acoustic radiation force and temperature simultaneously. By acquiring multiple acquisitions of the same k-space lines every TR, it was shown that the contributions of displacement and temperature to the total measured phase could be attributed to the proper source. This method's measurements of temperature and displacement agreed favorably with those of independent techniques. The displacement peak matched to within 0.5 μm of a standard spin-echo ARFI method, and maximum temperature agreed to within 0.8 °C. This new tool was used to answer an important question: does peak temperature and peak displacement occur at a different location along the beam propagation direction? It was found that both peaks coincide within approximately 0.5 mm, a result that is more reliable than when attempted with separate ARFI and temperature scans since this result is self-registered. When beam localization is the primary goal, this method may be used in a third mode where only the total phase difference is considered since the sensitivity to both temperature and displacement could provide a clearer indication of the beam's center.

4.6 References

[1] V. Auboiroux, M. Viallon, J. Roland, J.-N. Hyacinthe, L. Petrusca, D. R. Morel, T. Goget, S. Terraz, P. Gross, C. D. Becker, and R. Salomir, "ARFI-prepared MRgHIFU in liver: simultaneous mapping of ARFI-displacement and temperature elevation, using a fast GRE-EPI sequence," *Magn. Reson. Med.*, vol. 68, no. 3, pp. 932–946, Sep. 2012.

[2] E. A. Kaye, J. Chen, and K. B. Pauly, "Rapid MR-ARFI method for focal spot localization during focused ultrasound therapy," *Magn. Reson. Med.*, vol. 65, pp. 738–743, Mar. 2011.

[3] R. V. Mulkern, L. P. Panych, N. J. McDannold, F. A. Jolesz, and K. Hynynen, "Tissue temperature monitoring with multiple gradient-echo imaging sequences," *J. Magn. Reson. Imaging JMRI*, vol. 8, no. 2, pp. 493–502, Apr. 1998.

[4] E. A. Kaye and K. B. Pauly, "Adapting MRI acoustic radiation force imaging for in vivo human brain focused ultrasound applications," *Magn. Reson. Med.*, vol. 69, no. 3, pp. 724–733, Mar. 2013.

[5] N. Todd, M. Diakite, A. Payne, and D. L. Parker, "Hybrid proton resonance frequency/T1 technique for simultaneous temperature monitoring in adipose and aqueous tissues," *Magn. Reson. Med.*, vol. 69, no. 1, pp. 62–70, Jan. 2013.

[6] C. Lorenzato, C. Oerlemans, A. Cernicanu, M. Ries, B. Denis de Senneville, C. Moonen, and C. Bos, "Rapid dynamic R1 /R2* temperature assessment: a method with potential for monitoring drug delivery," *NMR Biomed.*, vol. 27, no. 11, pp. 1267–1274, Nov. 2014.

CHAPTER 5

CONCLUSION

This dissertation has presented several methods for improving focused ultrasound thermal therapies. In Chapter 2, a new adaptive model-predictive controller was successfully demonstrated *in vivo*, and simulations showed that its predictive features helped reduce treatment time by approximately 50% compared to treatments performed without prediction. The predictive features also helped mitigate the negative effects of longer MR sampling intervals, allowing more flexibility in selecting imaging parameters. Chapter 3 presented a new technique for performing MR-ARFI in three dimensions. This 3D spin-echo method accurately localized the focal spot in a single scan, and would have direct application to setting up the controller presented in Chapter 2. Furthermore, this 3D ARFI technique localized the ultrasound beam in fat, which is not possible with traditional beam localization methods that rely on PRF thermometry. Finally, Chapter 4 demonstrated a novel method for acquiring 3D ARFI displacement maps simultaneously with 3D temperature maps using a multicontrast sequence. This improved the safety of using 3D ARFI repeatedly since temperature can be monitored.

5.1 Additional Accomplishments

The effort expended while completing this dissertation has also resulted in over 50,000 lines of Matlab code, the creation of parsers for extracting useful information from the log files of several software programs, and generated over 35 conference abstracts, and nine journal publications including the following:

- **J. de Bever**, N. Todd, A. Payne, R. Roemer, "Adaptive model-predictive controller for magnetic resonance guided focused ultrasound therapy," *Int. J. of Hyperthermia,* vol. 30, no. 7, pp. 456-470, Nov. 2014.

- Payne, **J. de Bever**, A. Farrer, B. Coats, D.L. Parker, D.A. Christensen, "A simulation technique for three-dimensional MR-guided acoustic radiation force imaging," *Med. Phys.*, (Accepted).

- H. Odéen, **J. de Bever**, S. Almquist, A. Farrer, N. Todd, A. Payne, J.W. Snell, D.A. Christensen, D.L. Parker, "Treatment envelope evaluation in transcranial magnetic resonance-guided focused ultrasound utilizing 3D MR thermometry," *J. of Ther. Ultrasound*, vol. *2*, no. 19, Oct. 2014.

- N. Todd, J. Prakash, H. Odéen, **J. de Bever**, A. Payne, P. Yalavarthy, DL Parker, "Toward real-time availability of 3D temperature maps created with temporally constrained reconstruction," *Mag. Res. Med.*, vol. 71, no. 4, pp. 1394-04, Apr. 2014.

- A. Payne, R. Merrill, E. Minalga, U. Vyas, **J. de Bever**, N. Todd, R. Hadley, L. Neumayer. A. Christensen, R. Roemer, D. Parker, "Design and characterization of a laterally mounted phased-array transducer breast-specific MRgHIFU device with integrated 11-channel receiver array," *Med. Phys.,* vol. 39, no.3, pp. 1552-60, Mar. 2012.

- N. Todd, U. Vyas, **J. de Bever**, A. Payne, D. L. Parker, "Reconstruction of fully three-dimensional high spatial and temporal resolution MR temperature maps for retrospective applications," *Mag. Res. Med.*, vol. 67, no. 3, pp. 724-730, Mar. 2012.

- R. Koslover, B. Gleeson, **J. de Bever**, W. Provancher, "Mobile navigation using haptic, audio, and visual direction cues with a handheld test platform," *IEEE Transactions on Haptics*, vol. 5, no. 1, pp. 33-38, Jan. 2012.

- Payne , U. Vyas, N. Todd , **J. de Bever** , D.A. Christensen , D. L. Parker, "The effect of electronically steering a phased array ultrasound transducer on near-field tissue heating," *Med. Phys.*, vol. 38, no. 9, pp. 4971-4981, Sep. 2011.

- N. Todd, U. Vyas, **J. de Bever**, A. Payne, and D.L. Parker, "The effects of spatial sampling choices on MR temperature measurements," *Mag. Res. Med.*, vol. 65, no. 2, pp. 515-521, February, 2011.

Additionally, Appendix A details the device I designed and constructed that converts the optical trigger emitted by the MRI into an electrical signal compatible with the ultrasound generator. This device was initially created for use with the ARFI pulse sequences discussed in Chapters 3 and 4, however, the flexibility of its design has made it useful for many other projects not discussed in this dissertation including ultrasound neurostimulation studies, where ultrasound pulses are triggered by a functional MRI pulse sequence, and for perfusion studies, where ultrasound heating pulses must be accurately synchronized with temperature imaging.

Appendix B expounds my design of a device for removing oxygen dissolved in water. By replacing the manual water boiling method we employed previously, this device has saved time, money, and improved the scientific rigor of our experiments.

Many opportunities exist for expanding the work presented in this dissertation. Merging the controller work of Chapter 2 with k-space undersampling strategies would reduce the time between temperature measurements and enable the controller to make faster, more accurate, decisions. Increasing the time horizon over which the controller makes predictions could also decrease treatment times (and may require more advanced models), as could further investigations into optimal treatment planning. Investigating the benefits of applying model predictive control concepts to other therapies such as ultrasound assisted immunotherapy, targeted drug-delivery, and hyperthermia could also be fruitful. A very real clinical need exists for performing 3D ARFI in human organs such as the breast and the brain. These organs are well suited

to the 3D ARFI pulse sequences presented due to the limited motion they experience, and by adding navigator pulses, these techniques could become more robust to motion.

APPENDIX A

DESIGN AND CONSTRUCTION OF A TRIGGER CONVERSION DEVICE

A.1 Motivation

In order to perform the acoustic radiation force imaging (ARFI) techniques developed in Chapters 3 and 4, it was necessary to synchronize the firing of short ultrasound bursts (on the order of 1 – 20 ms in duration) with the motion encoding gradients generated by the MRI scanner. Unfortunately, we did not have this capability when we endeavored to perform ARFI. This chapter describes the technical challenges that needed to be solved as well as the design and construction of the device that made synchronization of the ultrasound and MRI pulse sequence possible.

A.2 Design Constraints and Features

The Siemens MRI scanner has a fiber optic output that can be used to generate trigger pulses at programmer determined moments during the pulse sequence. The converter device's primary function is to convert the optical trigger from the MRI scanner to an electrical trigger signal compatible with the ultrasound generator. However, at the time of construction, three technical limitations existed. First, the ultrasound generator could only respond to an electrical trigger signal. Second, all Siemens MRI pulse sequences group hardware instructions into "event blocks." These

event blocks are played out sequentially, and it is generally not possible to begin a hardware activity in one event block and conclude the activity in a subsequent block. Third, the electrical input to the ultrasound generator gates the output of the ultrasound, i.e., when the input signal is logical-high, ultrasound emission is permitted, and, conversely, emission is prevented when the gating signal is logical-low.

It is the second and third techincal limitations that most heavily impacted the design of the conversion circuitry. Given that the ultrasound generator uses a gating signal, it would seem logical to have the MRI pulse sequence emit an optical pulse for the entire duration of the ultrasound burst. However, this would force the pulse sequence event block to also last for the duration of the ultrasound burst, and this might interfere with the timing of other sequence event blocks. Instead, two very short optical pulses, each lasting ~20 μs, are emitted; the first optical pulse indicates when the ultrasound emission should begin, and the second when the ultrasound emission should end. This solves the event block problem because each optical trigger from the MRI can be in two different event blocks, and the trigger is so short that it will not impede other sequence activities. This also provides a large degree of flexibility in controlling the duration of the ultrasound pulse.

However, using the two-trigger approach requires a more advanced circuit in order to control the ultrasound gating signal described in the third limitation; it is no longer sufficient to simply convert the optical signal to an electrical signal. Now, the conversion circuit must remember the current state (allow vs disallow emission of ultrasound), and switch the electrical signal delivered to the ultrasound generator from

logical-low to logical-high, or vice versa, every time an optical trigger pulse arrives from the MRI. This is achieved using a Schmitt-triggered JK Flip-Flop.

However, employing the two-trigger approach to overcome the aforementioned technical limitations creates a new safety concern that must be mitigated by the trigger conversion device. Under normal conditions, the gating signal will remain in the logical-high state for only 1 – 20 ms, and so despite the high acoustic power used by ARFI, the ultrasound pulses are safe. However, a variety of technical failures could result in the trigger conversion device not receiving the second MRI optical trigger, and thus the gating signal controlling the ultrasound burst would remain in the logical-high state indefinitely. This could cause significant risk to the target tissue in a matter of seconds.

For this reason, a "dead man's switch" safety mechanism was integrated in the trigger converter's design. When the converter powers on, it resets itself to a known state where the gating signal sent to the ultrasound generator is logical-low, preventing the emission of ultrasound energy. With the arrival of an optical trigger pulse from the MRI, the converter switches the gating signal from logical-low to logical-high while simultaneously starting a safety countdown timer. The safety timer's duration is configurable (see Figure A.1), but is typically 500 ms. If the safety timer expires before the second optical trigger arrives from the MRI, the timer forces the gating signal back to logical-low thus preventing an unsafe ultrasound emission. Furthermore, the device is placed in an error state (indicated visually by a red LED on the front of the device) which locks the device into safe mode (logical-low), and ignores further input trigger pulses. To return to normal operation, the user must manually press the reset button.

Figure A.1: Final version of the trigger conversion device. Front panel has an input select switch and LED indicators that display which input method is active, an error LED that illuminates when the safety timer has expired, a manual reset button to reset the device, and a safety timer adjustment screw. The output signals are on the right hand side of the device. Both electrical and optical outputs are active simultaneously. Between the outputs are two switches that select the trigger type and output mode.

The converter circuit was also designed with flexibility in mind and can be operated in several modes. In addition to taking an optical trigger as the input signal, the converter device can also take an electrical TTL trigger, and manual push button input. The converter device also emits its output signal simultaneously as an electrical output (usually connected to the ultrasound generator), and an optical output in case other devices need to be triggered or the capabilities of the ultrasound generator expand. Additionally, three types of output trigger signal can be selected. The first trigger type, labeled as "safe" on the device, implements the two-trigger conversion with safety timer as described above. The second mode, labeled "pass thru" on the device, bypasses the JK Flip-Flop and safety timer functionality and simply converts the optical signal to an equivalent electrical signal. This mode may be used by hardware which allows direct triggering by an electrical signal as oppose to gating as in the "safe" mode. The last mode, labeled "unsafe" on the device, uses the JK Flip-

Flop functionality but bypasses the safety timer. This would be useful for applications where there is no safety risk associated with the gating signal remaining in the active state.

There are also three output modes. The first, labeled "Trig" on the device, outputs the trigger type selected in the previous paragraph. The second mode, labeled "Tmr" on the device, outputs the timer signal instead of the trigger signal. This is useful for diagnostics and confirming the timer duration. The last mode, labeled "ON" on the device, overrides all triggers and outputs a constant logical-high signal. This would be used when triggering is not needed, but when disconnecting the trigger conversion device would be too time consuming.

Finally, the device can operate on power provided by an electrical outlet, or four standard AA batteries.

A.3 Construction

An initial prototype was designed and implemented on a bread board before a printed circuit board was designed (see Figure A.2). The printed circuit board (PCB) was designed in PCB Artist (Advanced Circuits and WesDev Ltd). The final circuit schematic is shown in Figure A.3, and was laid out on a two-layer PCB (Figure A.4). The final PCB design was manufactured by Advanced Circuits. Surface mount components were attached to the PCB manually by applying solder paste to each pin pad and carefully laying the components on their designated location. The partially assembled PCB was then placed on a hot plate, as shown in Figure A.5, until the solder began to visually wick into the proper position. The board was then removed from the heating pad causing the solder paste to solidify. The PCB was designed to take this

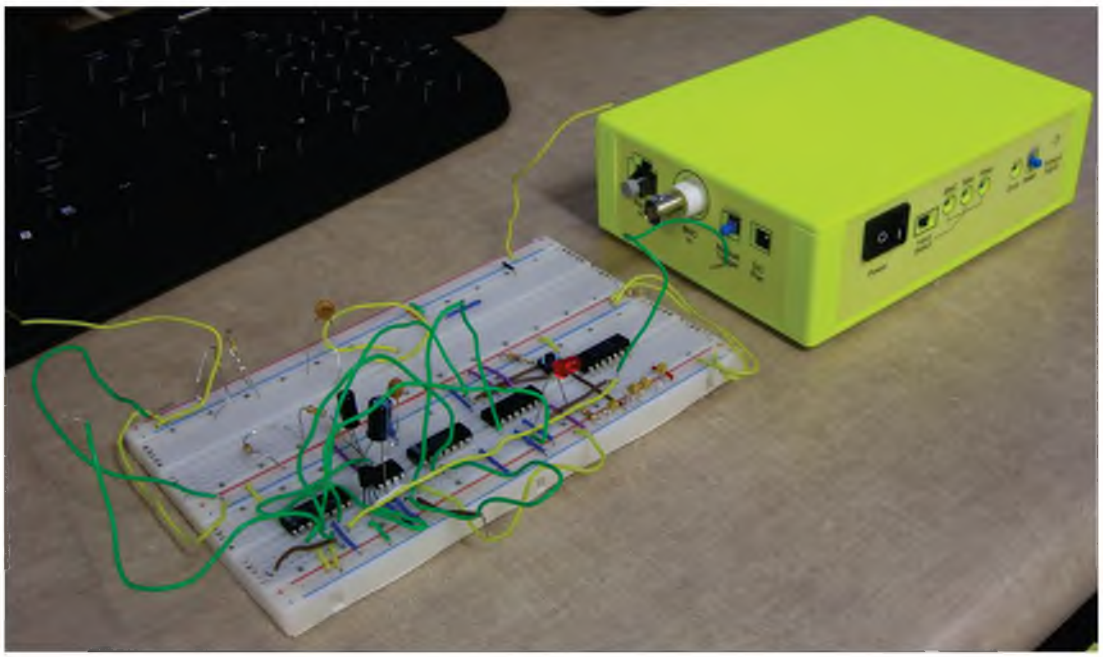

Figure A.2: The initial prototype conversion circuit implement on a breadboard (left) next to the final device (right).

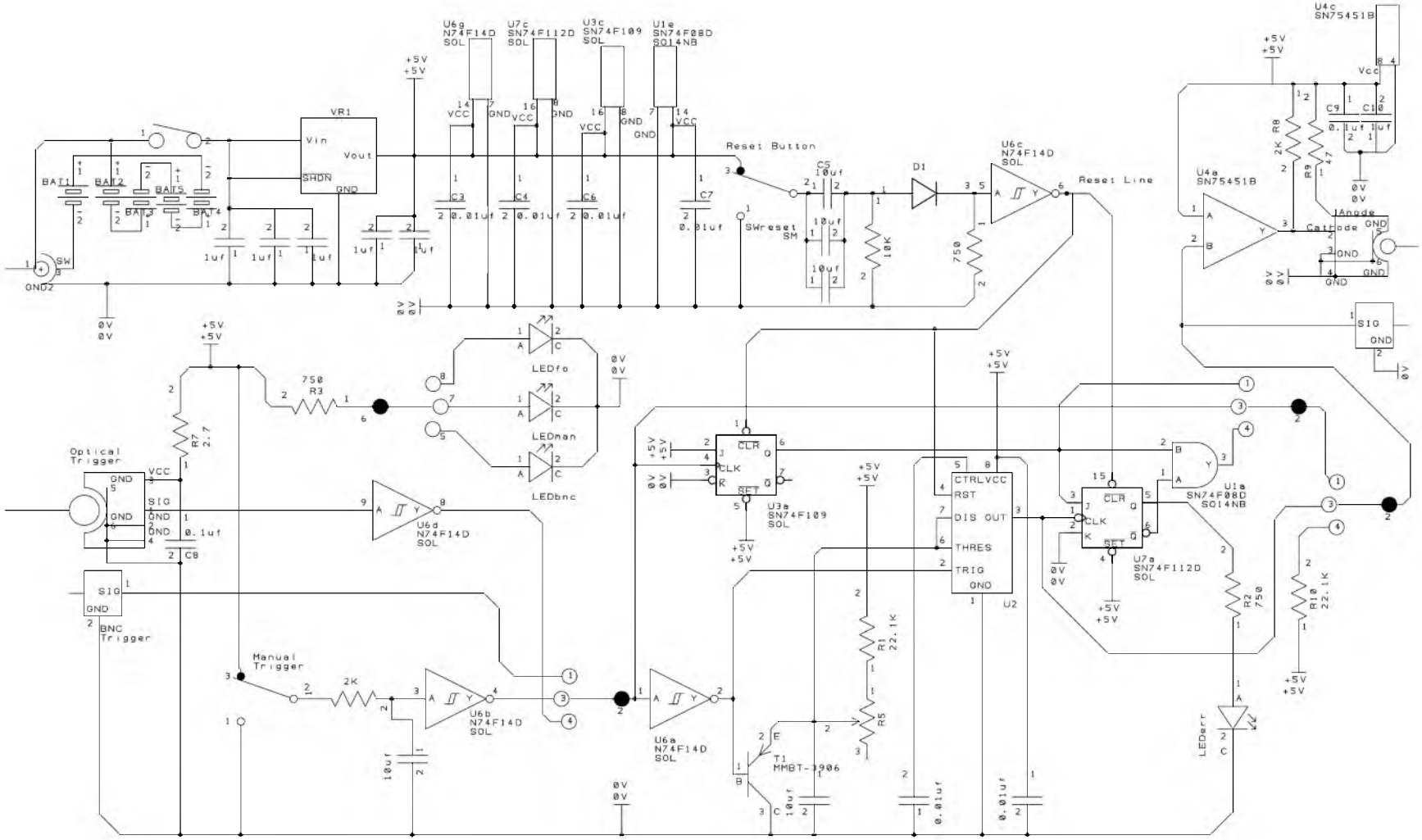

Figure A.3: The final trigger converter circuit schematic

(a)

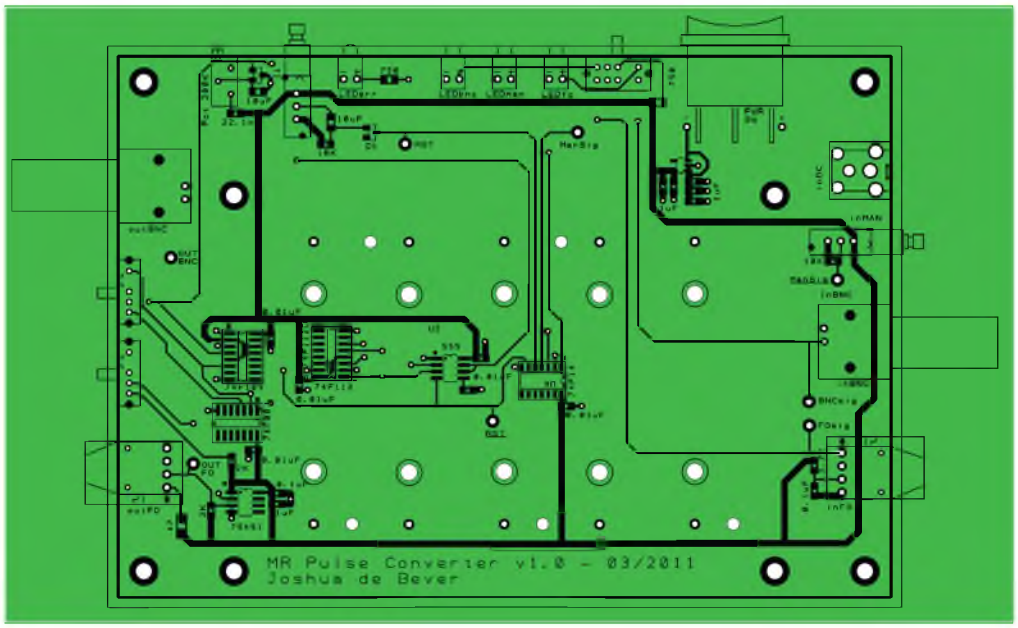

(b)

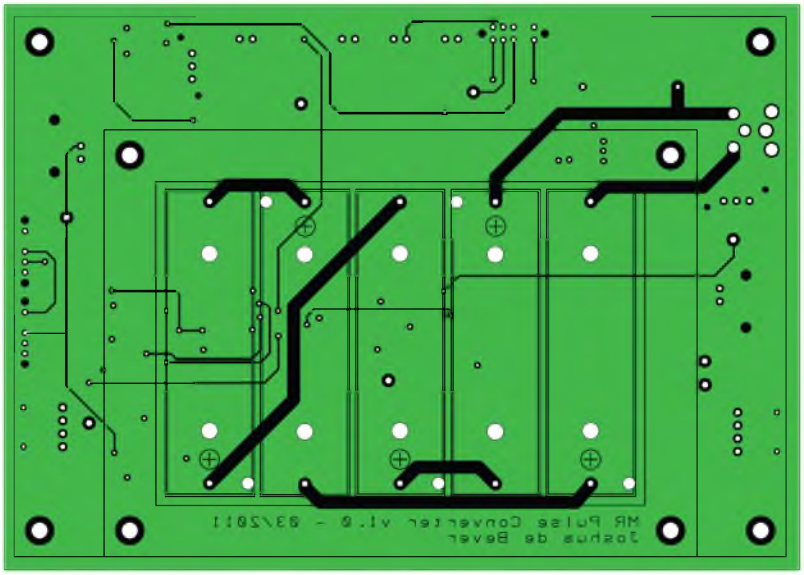

Figure A.4: The final PCB layout. **(a)** Top layer of PCB. **(b)** Bottom layer of PCB.

Figure A.5: A hot plate was used to solder surface mount components.

manufacturing step into account since only the top layer would allow for surface mount components to be attached using this simple method. The remaining components were manually soldered, and the final result can be seen in Figure A.6. An enclosure was designed in Solid Works (Dassault Systèmes) and was fabricated using 3D printing. To facilitate through-panel connections, all electrical components were modeled to ensure accurate placement and hole sizes (see Figure A.7).

A.4 Discussion and Conclusion

The final trigger conversion device has proved to be very reliable, and the flexible design has found application beyond the MR-ARFI scenarios presented in this dissertation. For instance, the trigger conversion device has enabled precise synchronization of heating pulses with MR thermometry sequences, as well as neuromodulation applications where the ultrasound is triggered by an fMRI pulse sequence. The safety timer is configurable from between 400 ms – 2.8 s, and the device can be triggered with optical pulses shorter than 1 μs.

A.5 Parts List

The components used to construct the trigger conversion device are detailed in Table A.1. Most of the components used are generic enough that equivalent components from another manufacturer could be substituted if desired.

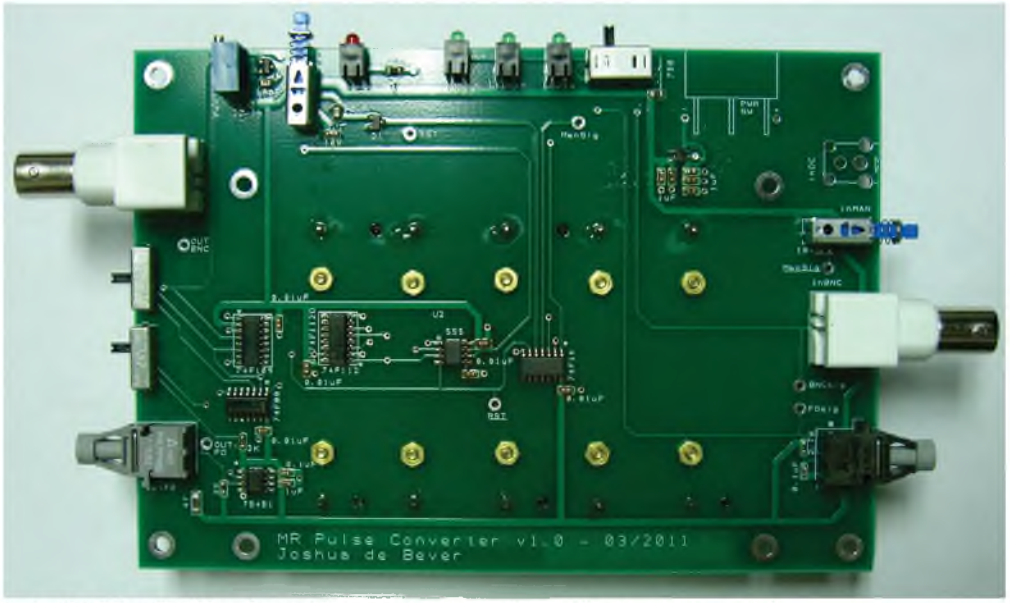

Figure A.6: The PCB after all components have been mounted.

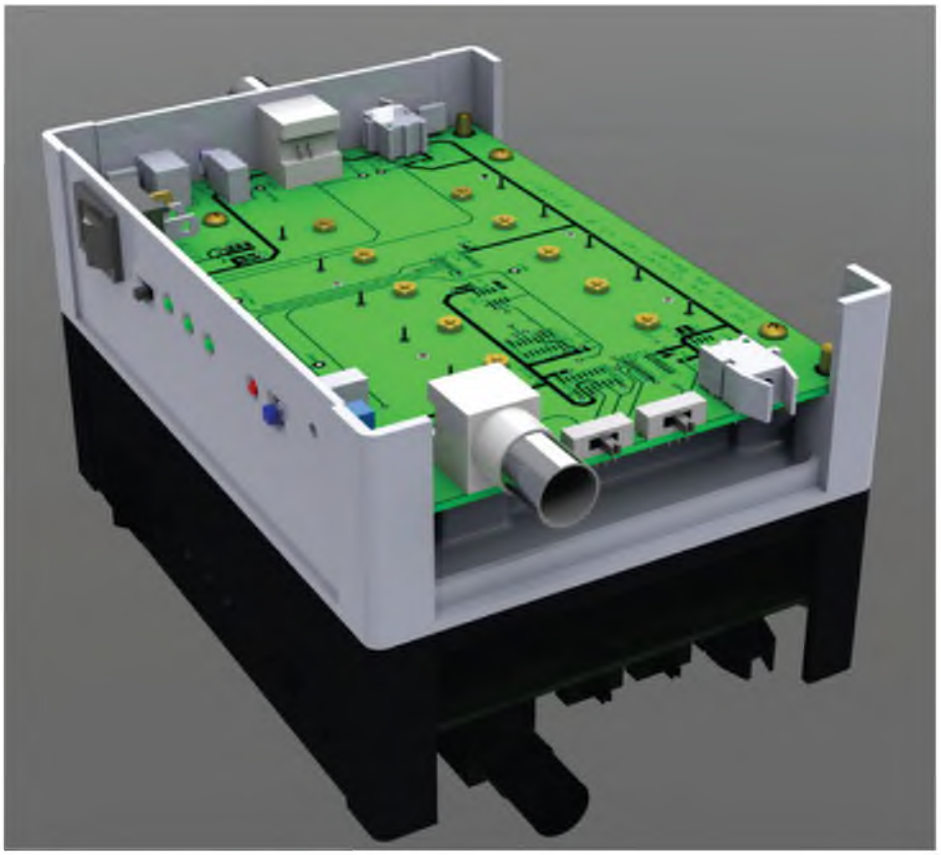

Figure A.7: Rendering of enclosure, PCB, and mounted components.

Table A.1: Parts list for trigger conversion device

Passive Components

Part Type	Part Description	Manufacturer	Part #	Qty
Resistor (SM)	2.7 Ohm, 5%, 0.1W, 0603	Stackpole	RMCF0603JT2R70	1
Resistor (SM)	47 Ohm, 1%, 0.25W, 1206	Rohm Semiconductor	MCR18EZPF47R0	1
Resistor (SM)	750, 1%, 0.125W, 0805	Stackpole	RMCF0805FT750R	2
Resistor (SM)	2K, 1%, 0.1W, 0603	Stackpole	RMCF0603FT2K00	2
Resistor (SM)	10K, 1%, 0.1W, 0603	Stackpole	RMCF0603FT10K0	2
Resistor (SM)	22.1K, 1%, 0.1W, 0603	Stackpole	RMCF0603FT22K1	1
Potentiometer	200k, 25-Turn, PC-Mount, Right-Angle	Murata	PV36Z204C01B00	1
Capacitor (SM)	0.01uF, 5%, 50v, MLCC, X7R, 0603	TDK	C1608X7R1H103J	2
Capacitor (SM)	0.1uF, 10%, 50v, MLCC, X7R, 0603	Kemet	C0603C104K5RACTU	6
Capacitor (SM)	1.0uF, 10%, 50v, MLCC, X7R, 0603	TDK	C1608X5R1H105K	3
Capacitor (SM)	10uF, 10%, 10v, MLCC, X5R, 0805	Murata	GRM21BR61A106KE19K	2

Input/Output Jacks, Switches, & Indicators

BNC Jack	50 Ohm PC-Mount, Right Angle WHITE HOUSING	Amphenol	31-54341-10RFX	2
Fiber Optic Transmitter	Fiber optic transmitter, PC-Mount, Right Angle	Avago	HFBR-1528Z	1

Table A.1 Continued

Part Type	Part Description	Manufacturer	Part #	Qty
Fiber Optic Receiver	Fiber optic receiver, PC-Mount, Right Angle	Avago	HFBR-2528Z	1
LED	Green, 3mm (T-1), PC-Mount, Right-Angle	Kingbright	WP934CB/GD	3
LED	Red, 3mm (T-1), PC-Mount, Right-Angle	Kingbright	WP934CB/ID	1
Slide Switch	1P3T	C&K Components	OS103011MA7QP1	2
Slide Switch	2P3T	C&K Components	OS203011MA2QP1	1
Push Button	1P Momentary	ALPS	SPPJ311500	2
Knob	Red knob for ALPS SPPJ3 pushbutton	ALPS	UJ206020	2
Power Switch	Rocker Switch, SPST, Black, Snap-In	C&K Components	DA102J12S215HQF	1
	Integrated Circuits			
Logic-AND	Quad-AND gate, 2-Input	Texas Instruments	SN74F08D	1
Logic-NOT	Hex-Schmitt Triggered Inverter	Phillips	N74F14D	1
Flip-Flop	Positive-Edge triggered, JK Flip-Flop	Texas Instruments	SN74109D	1
Flip-Flop	Negative-Edge triggered, JK Flip-Flop	Texas Instruments	SN74112D	1
Timer	555 Precision Timer	Texas Instruments	TLC555-CDRG4	1
Transistor	General Purpose switching transistor	Fairchild	MMBT-3906	1
Peripheral Driver	Dual Hi Current Peripheral Drivers	Texas Instruments	SN75451B	1

Table A.1 Continued

Part Type	Part Description	Manufacturer	Part #	Qty
Diode	General Purporse Diode, Surface mount	NXP	BAS16,235	1
		Power		
Battery Holder	1xAA Holder, PC-Mount	MPD	BHAA-3	5
DC Jack	DC power jack, shielded, ID=2.1mm, OD=5.5mm	CUI	PJ-047A	1
DC Adapter	7.5V, 6W, 0.8A, AC-DC adapter, ID=2.1mm, OD=5.5mm	Mean Well	GS06U-11P1J	1
		Structural		
Screw	4-40, 1/2", Machine Screw, Pan-Head, Phillips, Brass		94070A110	8
Screw	4-40, 1/4", Machine Screw, Flat-Head, Phillips, Brass		92480A106	1
Screw	2-56, 1/4", Machine Screw, Flat-Head, Slot, Brass		92451A077	10
Thread Insert	4-40 Thread Insert w/o Flange, 3/16" Thread length, Brass		92395A112	9
Hex Nut	2-56 Hex Nut, 3/16" Width, 1/16" Height, Brass		92671A003	10

Table A.1 Continued

Part Type	Part Description	Manufacturer	Part #	Qty
Quick-Connect Terminal	Female 0.187 Quick Connect terminal			2
Rubber feet	for 0.250" (1/4") Dia. Hole			4

APPENDIX B

DESIGN AND CONSTRUCTION OF A DEVICE FOR THE REMOVAL OF DISSOLVED OXYGEN FROM WATER

B.1 Motivation

It is common for the ultrasound beam to be coupled to the target tissue via a water bath; however, any oxygen dissolved in the water bath will scatter the beam and reduce the beam power delivered to the target. Dissolved oxygen can also cause cavitation which has the potential to be dangerous, for example, if bubbles were to accumulate on the patient's skin. Consequently, ensuring the water bath contains low amounts of dissolved oxygen is critical for performing safe, high quality, focused ultrasound studies. Unfortunately, water normally contains large amounts of dissolved oxygen. Additional gases are also likely to be dissolved in water, however, dissolved oxygen content is a good indicator of overall gas levels and so monitoring other gases is of secondary concern. While, commercially available systems for degassing water exist, they are prohibitively expensive, costing approximately $4,000 – $10,000, and do not meet all our performance goals. This chapter discusses the design, construction, and testing of an automated device for removing dissolved oxygen from water that is economical and highly effective.

B.2 Design Targets

Our target design criteria are summarized in Table B.1. A target dissolved oxygen content of 1 ppm (or 1 mg/liter) was selected based on common industry standards. For instance, to sell an ultrasound device in Canada, Health Canada requires that the ultrasound device have its performance quantified in water that starts <= 2 ppm at 22 ± 3°C [1]. Furthermore, water below 4 ppm is absolutely required to avoid cavitation, and so to ensure that the water bath is sufficiently degassed for the duration of the experiment, even after multiple transfer steps, the initial dissolved oxygen content should be < 2 ppm. As a worst-case scenario, we assumed that the de-ionized water available begins at a dissolved oxygen content of 7 ppm.

A target goal of degassing a water volume of 40 L (approximately 10 gallons) to a dissolved oxygen content of 1 ppm within 4 hours was selected. This goal enables us to replace the transducer's water bath multiple times during an experiment as well as make phantoms, etc. with water to spare. A 4 hour timeline ensures same-day access to degassed water so we can always run sound experiments.

Lastly, the degassing system should require as little human interaction as possible while remaining safe and efficient.

B.3 Degassing Methods

Several methods exist for degassing water. The following expanded descriptions of each degassing method include paraphrased material available from Health Canada and Precision Acoustics [1], [2].

Table B.1: Target design criteria for the water degassing device

Target	Value
Initial dissolved oxygen content	7.0 ppm
Final dissolved oxygen content	1.0 ppm
Volume to be degassed	40 L / ~10 Gallons
Max time to degas volume	4 hours
Cost	$2000

B.3.1.1 *Boiling*

This is a simple and effective way of degassing water. While boiling periods as short as 5 – 15 minutes are sufficient to reduce oxygen levels below 2 ppm, it can take a long time to boil a sufficiently large volume of water. Furthermore, the water will need to cool before it can be used. During the extended cooling duration, the water is regassing, and thus undoing the work that was just done.

B.3.1.2 *Vacuum*

When subjected to hard vacuums, dissolved oxygen levels can be reduced below the 1 ppm. This method of degassing is suited to small volumes of water, but can be difficult to implement for larger volumes.

B.3.1.3 *Reduced Pressure Recirculation*

The system comprises of a high volume pump connected to a standing body of water by rigid walled tubing. A pressure restrictor is fitted to the inlet tube, such that the pump is attempting to draw water through the tube faster than water is allowed in.

This creates a partial vacuum within the rigid walled tube and any dissolved gas bubbles increase in size, and eventually nucleate to form larger bubbles which eventually escape to the surface. Oxygen levels of 2-3 ppm can be achieved.

B.3.1.4 Addition of Sodium Sulphite

Sodium sulphite reacts with the dissolved oxygen in the water. Sodium sulphite concentrations as low as 4 g/liter will keep oxygen levels below 2 ppm for at least 40 hours. However, this technique introduces significant ionic content, and can increase the water's conductivity above allowed limits. Furthermore, sodium sulphite solution is alkaline and will result in corrosion of many metals including aluminum and nickel, and may not be safe for contact with skin.

B.4 Selected Design and Rationale

The boiling method was ruled out because it is impractical for degassing the large 40 L target volume. Due to the difficulty of heating such a large volume, the water must boiled in batches, and each batch can take 2-3 hours once heating and cooling time is accounted for. This method also requires constant human monitoring to ensure safety and efficient throughput. Vacuum degassing was also ruled out for being too slow and requiring multiple batches, which requires human interaction. Adding sodium sulphite risks damaging the transducer and could possibly harm the patient.

The selected design combines the vacuum method with the reduced pressure recirculation method to provide a device capable of degassing large volumes of water without human interaction and without altering the chemistry of the water bath. A

schematic of the degasser components is shown in Figure B.1, and the final constructed device is shown in Figure B.2. The design uses Liqui-Cel Contactors made by Membrana – Charlotte, a division of Celgard LLC. These modules consist of a hydrophobic porous membrane that allow water to pass through the contactor while a vacuum pump pulls gas through the membrane and out of the water. Flow rates up to 3 L/min are achievable using their "MiniModules." These modules are the second most expensive component of the system, and require a vacuum pump that is sold separately.

Several types of vacuum pumps exist including oil lubricated rotary pumps, dry vane pumps, rotary screw dry pumps, liquid ring pumps, and diaphragm pumps. For this application, a diaphragm pump was selected due to its immunity to water vapor and low maintenance costs (no oil or filters to clean/replace). The KNF USA Inc. LABOPORT N811KVP diaphragm vacuum pump was selected due to its relatively low cost and acceptable performance. At a price of $575, the N811KVP pump produces a maximum vacuum of 75 Torr. Future systems should consider the N816KTP model for $900 which produces a much stronger 15 Torr, vacuum.

To select the appropriate Liqui-Cel Contactor, the performance of four different versions was modeled to estimate the time required to reduce 40 L of water with an initial dissolved oxygen content of 7 ppm down to the desired target of 1 ppm. Membrana provides datasheets that estimate the percentage of oxygen removed at various flow rates after one pass through the Liqui-Cel contactor when applying a given vacuum. The higher the flow rate, the less oxygen is removed during each pass through the contactor; however, the more frequently water is recirculated. The

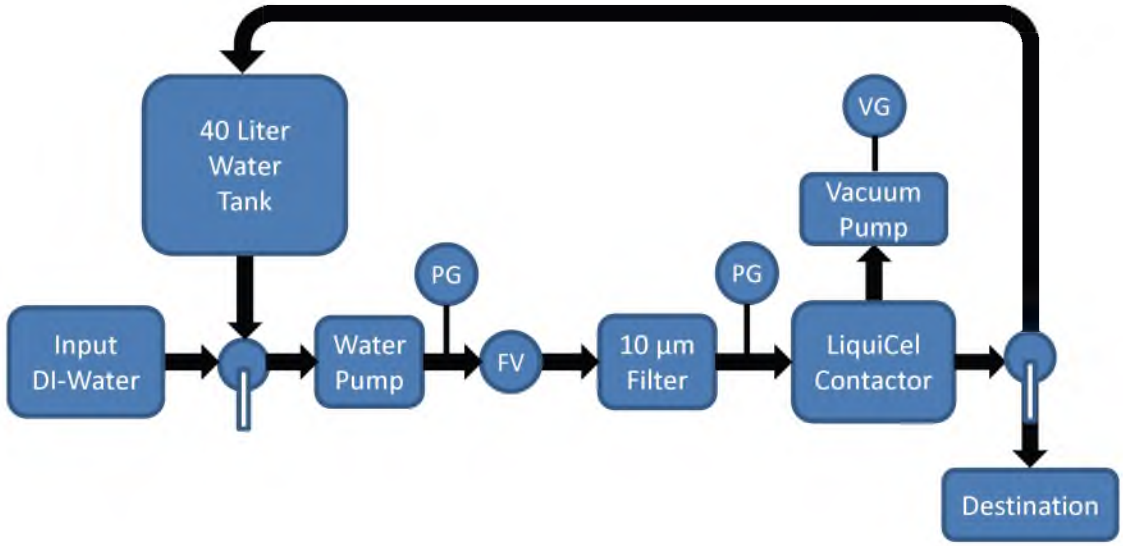

Figure B.1: Schematic diagram of the water degassing device. Repeated passes through the Liqui-Cel Contactor extracts dissolved oxygen from the water. PG = Pressure Gauge (optional). VG = Vacuum Gauge (optional). FV = Flow control Valve (optional). DI-Water = De-ionized water.

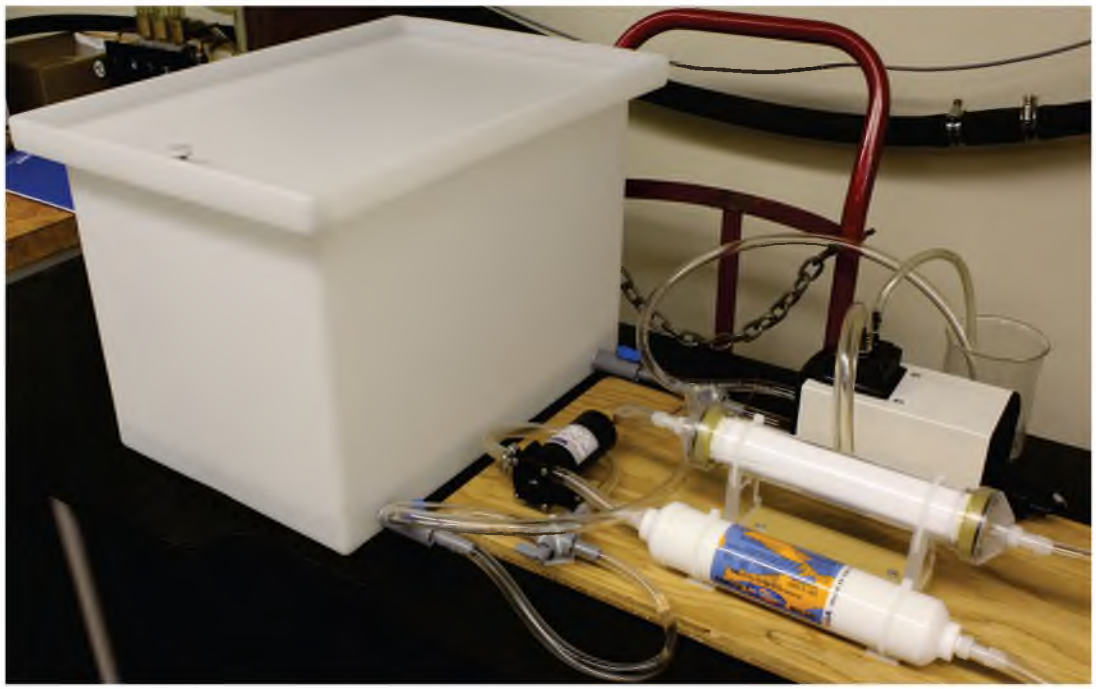

Figure B.2: Final version of degasser after construction.

performance of the contactors was derated since the vacuum pump selected can only provide a 75 Torr vacuum, and the lowest vacuum strength the contactor datasheets gave specifications for was a 50 Torr vacuum. The modeled performance of the four Liqui-Cel Modules is summarized in Table B.2. Based on these results, the MiniModule 1.7 x 8.75" ($475) was selected since it provides the best opportunity to achieve the 4 hour target degassing time while not being significantly more expensive than the lower performing models. These estimates also indicate that a flow rate of 1000 mL / minute should be sufficient, and this is readily achievable with economical water pumps. Many components in Figure B.1, such as the vacuum and pressure gauges, are recommended by Membrana for industrial applications, but were omitted in this design to reduce cost. Furthermore, some components are readily interchangeable with comparable devices. For instance, Membrana instructs users to install a 10 μm prefilter to protect the Liqui-Cel Contactor from debris carried in the water. A 5 μm prefilter, normally used for water fountains and refrigerators, was selected due to its low cost ($10 – $15), but other options exist. A DC water pump from SHURflo was selected because it allows for easy adjustment of the flow rate. Lastly, it was important to use thick-walled tubing for the connection between the contactor and the vacuum pump as thin-walled tubing could not withstand the pressure differential and collapsed.

B.5 Results and Discussion

To test the degassing device, the 40 L water tank was first filled with deionized water. Using a Hanna Instruments HI-9146 (Woonsocket, Rhode Island, USA) dissolved oxygen meter, the water tank's initial dissolved oxygen content was

Table B.2: Comparison of Liqui-Cel Contactors

	MicroModule 0.75 x 1"		**MiniModule 1.0 x 5.5"**		**MiniModule 1.7 x 5.5"**		**MiniModule 1.7 x 8.75"**	
Cost	$195		$290		$400		$475	
Max Flow Rate	100 mL /min		500 mL /min		2000 mL /min		3000 mL /min	
Vacuum for Spec	125 Torr		50 Torr		50 Torr		50 Torr	
	Flow Rate [mL/min]	Time to Target [Hours]	Flow Rate [mL/min]	Time to Target [Hours]	Flow Rate [mL/min]	Time to Target [Hours]	Flow Rate [mL/min]	Time to Target [Hours]
	20	46.4	100	17.9	200	9.2	250	7.4
	40	28.2	200	10.6	600	3.7	500	3.9
	60	21.6	300	8.9	1000	2.8	1000	2.1
	80	17.6	400	7.7	1400	2.3	1500	1.6
	100	16.4	500	6.8	2000	1.9	2500	1.4

measured to be 6.76 ppm. After starting degasser, measurements of the dissolved oxygen content were taken periodically, the results of which are shown in Figure B.3. The predicted time to reach the target dissolved oxygen content of 1.0 ppm was approximately 2.1 hours, and the measured dissolved oxygen content at that time was approximately 1.4 ppm. Reaching the 1.0 ppm level did not occur until the device had been running for approximately 4 hours. There are several reasons for the anticipated degassing rate to be higher than the measured rate. First, the vacuum pump selected can produce at most a 75 Torr vacuum, while the Liqui-Cel Contactor lists a minimum desired vacuum of 50 Torr. It is likely that the vacuum pump only operates at maximum capability during limited scenarios, so the effective vacuum is likely weaker than the 75 Torr value quoted by the manufacturer. Second, while the Liqui-Cel Contactor performance metrics were derated to account for the difference in vacuum strength when predicting their performance, it is possible that the derating applied was overly optimistic since it is not obvious how the degassing rate varies with vacuum strength. Third, as time progresses, the Liqui-Cel Contactor accumulates water on the outside of the membrane which may indicate that its performance is degrading over time. Fourth, the predicted performance did not account for regassing of the water in the water tank, but this is most certainly occurring. In fact, in Figure B.4 the degasser was shut off and the effect of regassing was measured. If the water surface of the water tank is properly covered from air exposure, regassing can be kept to approximately 0.11 ppm per hour, but nevertheless, this effect was missing from the predicted contactor performance.

Given these results, the choice to target a 1 ppm dissolved oxygen content now

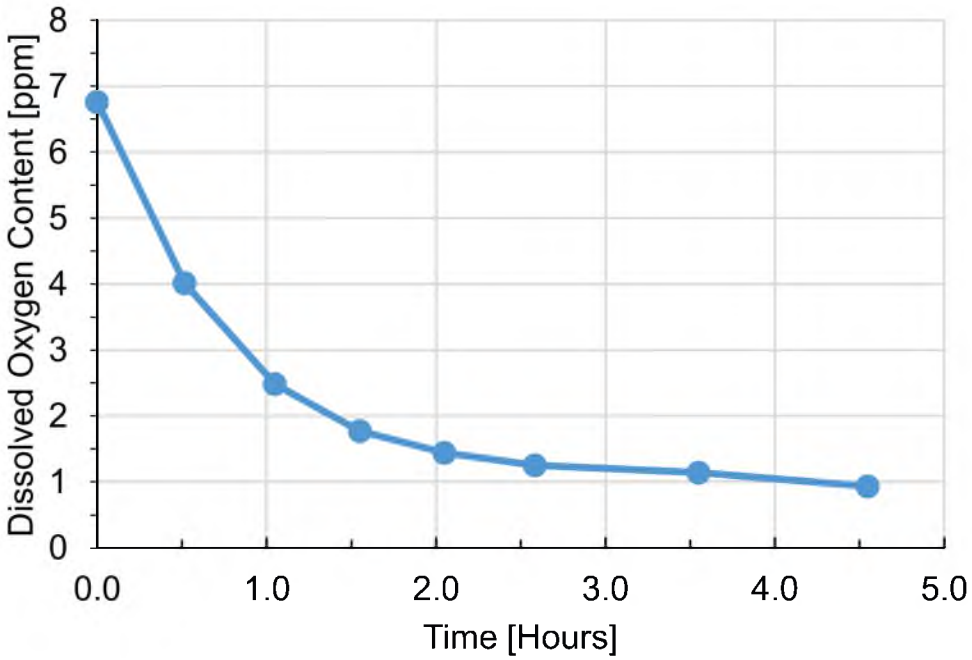

Figure B.3: Dissolved oxygen content of 40 L water tank while degasser is running. The target dissolved oxygen content of 1 ppm is achieved after approximately 4 hours, while 1.25 ppm is achieved after only 2.5 hours.

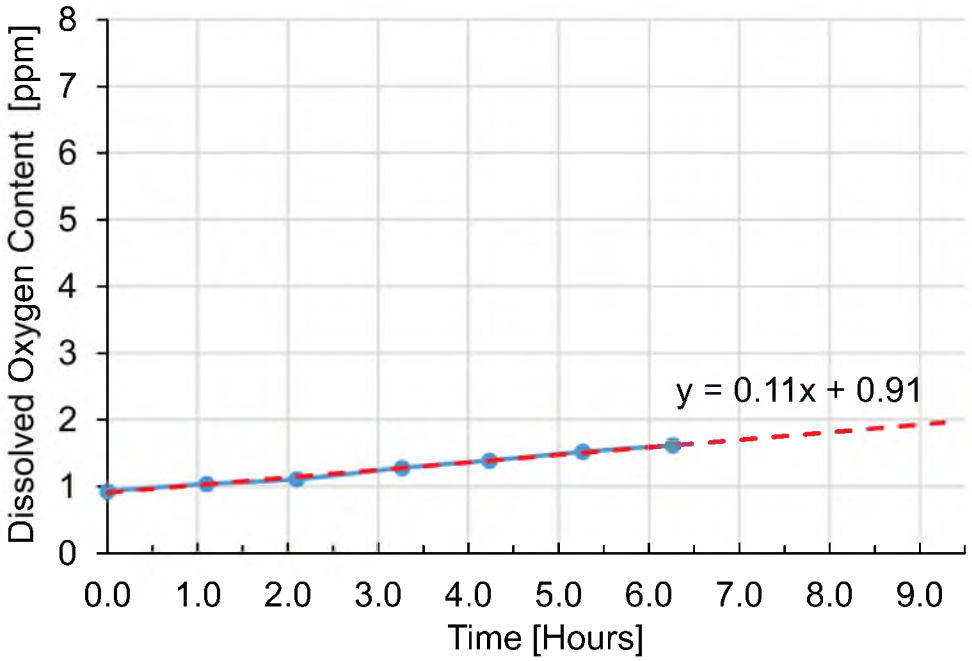

Figure B.4: Regassing of 40 L water tank once degasser is disabled. When the water is covered in the tank, it regasses at a rate of approximately 0.11 ppm per hour. At this rate, after 9 hours the water in the tank would still be below 2 ppm.

seems ambitious. That said, the target was achieved by the target duration of 4 hours, and it is important to note that very acceptable dissolved oxygen levels of approximately 1.3 ppm were achieved after only 2.5 hours. Finally, choosing the highest performing contactor was definitely the best choice given that the performance predictions were slightly optimistic.

B.6 Parts List and Cost Estimate

The parts required to construct this device, as well as their estimated cost, are shown in Table B.3. The vacuum pump can easily be substituted for another model, and a higher performing model could significantly improve the system's performance.

Table B.3: Parts list for water degassing device

Part	Description	Price Estimate
Membrana Liqui-Cel Contactor	MiniModule 1.7 x 8.75"	$475
Water pump	SHURflo 100 series, 24V	$50
5 μm Sediment Filter	Omnipure CL10PF5 inline sediment water filter	$15
DC power supply	12 V, 10 A	$100
Water Tank	10 Gallon capacity RV Supplies	$50
Vacuum Pump	KNF LABOPORT Mini Diaphragm Vacuum Pumps Model #: N811KVP (75 Torr)	$575
	or	*or*
	Model #: N816KTP (15 Torr)	$900
Misc	Tubing, Valves, Connectors, etc	$50
	Total Cost:	$1315 - 1640

B.7 Conclusion

A device for degassing water quickly, efficiently, and effectively has been designed, constructed, and tested. This device meets all of the design criteria – it automatically degasses 40 L of water to 1 ppm within 4 hours – and costs less than $1400. This is cheaper and more effective than commercially available systems, and eliminates the need for human monitoring. Performance could be improved further by investing in a higher performance vacuum pump, optimizing the flow rate through the Liqui-Cel Contactor, and investigating more effective methods of preventing regassing.

B.8 References

[1] Health Canada, "Selling Ultrasound Therapy Devices in Canada: What You Need to Know," 1999. [Online]. Available: http://www.hc-sc.gc.ca/ewh-semt/pubs/radiation/ultrasound_devices-appareils_ultrasons/index-eng.php. [Accessed: 21-May-2010].

[2] Precision Acoustics, "Water Treatment." [Online]. Available: http://acoustics.co.uk/products/3d-scanning-tanks/water-treatment-system/water-treatment/. [Accessed: 21-May-2010].